Use of inverse rock physics modeling in reservoir characterization

Kenneth Bredesen

Thesis for the degree
Master of Science

Department of Earth Science

University of Bergen

May 31, 2012

"Most people, if you describe a train of events to them will tell you what the result would be. They can put those events together in their minds, and argue from them that something will come to pass. There are few people, however, who, if you told them a result, would be able to evolve from their own inner consciousness what the steps were which led up to that result. This power is what I mean when I talk of reasoning backward."

Sherlock Holmes, in A Study of Scarlet

by Arthur Conan Doyle (1859 - 1930)

Abstract

Reservoir characterization based on seismic data demands a robust and reliable method that transforms seismically derived parameters such as elastic moduli, P-velocity, S-velocity or acoustic impedance into parameters delineating lithology and reservoir quality. However, as the number of such desirable reservoir parameters exceeds the number of seismic observables, a straightforward transformation does not exist. Hence, one is restricted to consider an approach by a set of rock physics constraints, which is often associated with a non-linear and undetermined problem with non-unique solutions. Johansen et al. (2011) developed such an approach referred to as *inverse rock physics modeling* (IRPM) that is based on the estimation strategy of Johansen et al. (2004).

There exists numerous rock physics models to cover the large span of different natural born rocks. As all these models simplify inherent complex rocks to predict the seismic response, their quantitative accuracy is debatable. Moreover, several reservoir parameters for these models have many elements of uncertainty attached, and it can be challenging to assign them proper values, e.g. the porosity of sediments in a reservoir at the stage of deposition. Despite these problems, the rock physics models have proved to yield constraint data that lie within a manageable proximity to real seismic data. The IRPM approach takes advantage of this fact and may serve as a tool for interpretation of lithology and evaluation of reservoir quality. However, users of the IRPM approach must aim their attention to recognize relevant uncertainties, pitfalls and limitations to reduce misinterpretation risks. This study considers a set of rock physics constraints where particular reservoir parameters have been perturbed to mimic uncertainty. From considering synthetic data, it was found that uncertainties in the reservoir parameters considered had a significant influence on the corresponding inverse solutions.

In reservoir monitoring the supervision of temporal fluid pressure and saturation alterations during production is key information to achieve optimized oil recovery. The IRPM approach is flexible to incorporate reservoir parameters that are of interest in reservoir monitoring. This study applies IRPM on real data from Glitne, North Sea, to predict pore pressure, saturation and porosity after a period of production. However, due to absence of repeated observational data from Glitne, a synthetic hybrid model was used to simulate production effects on the initial Glitne data. The results obtained showed little variation in the porosity solutions, a wide range of possible saturation solutions and pore pressure solutions that were cumbersome to constrain due to its insensitivity in the Glitne rock physics model. The solutions emphasize limited applications of IRPM to constrain particular reservoir properties that are highly insensitive in certain rock physics models.

Keywords: Reservoir characterization, rock physics, quantitative seismic interpretation, reservoir description, reservoir monitoring.

Acknowledgements

Through this work I have received excellent supervision from Prof. Tor Arne Johansen and his Ph.D. student Erling Hugo Jensen. I owe you both my gratitude, and I hope to gain more experience of cooperation with them as I plan to continue as a Ph.D. student.

All the lunch breaks with my fellow students bawling about non-geophysics related subjects have added joy to my everyday life at the University. They have becomed good friends and made useful comments unto this thesis.

My family has always encouraged me regarding my education. They have given me both moral and economical support, and I'm very lucky and thankful to have them standing behind my back.

Last but not least, my girlfriend Henriette. Your support and kindness have been immensely important for me to reach the finishing line of my thesis.

Kenneth Bredesen Bergen, May 31, 2012

Contents

Chapter 1

Introduction

1.1 Motivation

The global demand of oil is stretching for new limits parallel with declining production. Hence, enhanced oil recovery is a hot area of research in a wide range of scientific disciplines, including seismic reservoir characterization. Seismic reservoir characterization, also known as reservoir geophysics, is defined by Robert E. Sheriff as "The use of geophysical methods to assist in delineating or describing a reservoir or monitoring the changes in a reservoir as it is produced" (Walls et al., 2004). As such, a bridge between observed elastic properties (denoted data parameters) and reservoir properties (denoted model parameters) must be established in aid of reservoir characterization. Rock physics offers the key for linking the data and model parameters, and is a part of the so called *integrated approach* outlined in figure 1.1. The work in this thesis aims at *rock physics inversion* according to this figure.

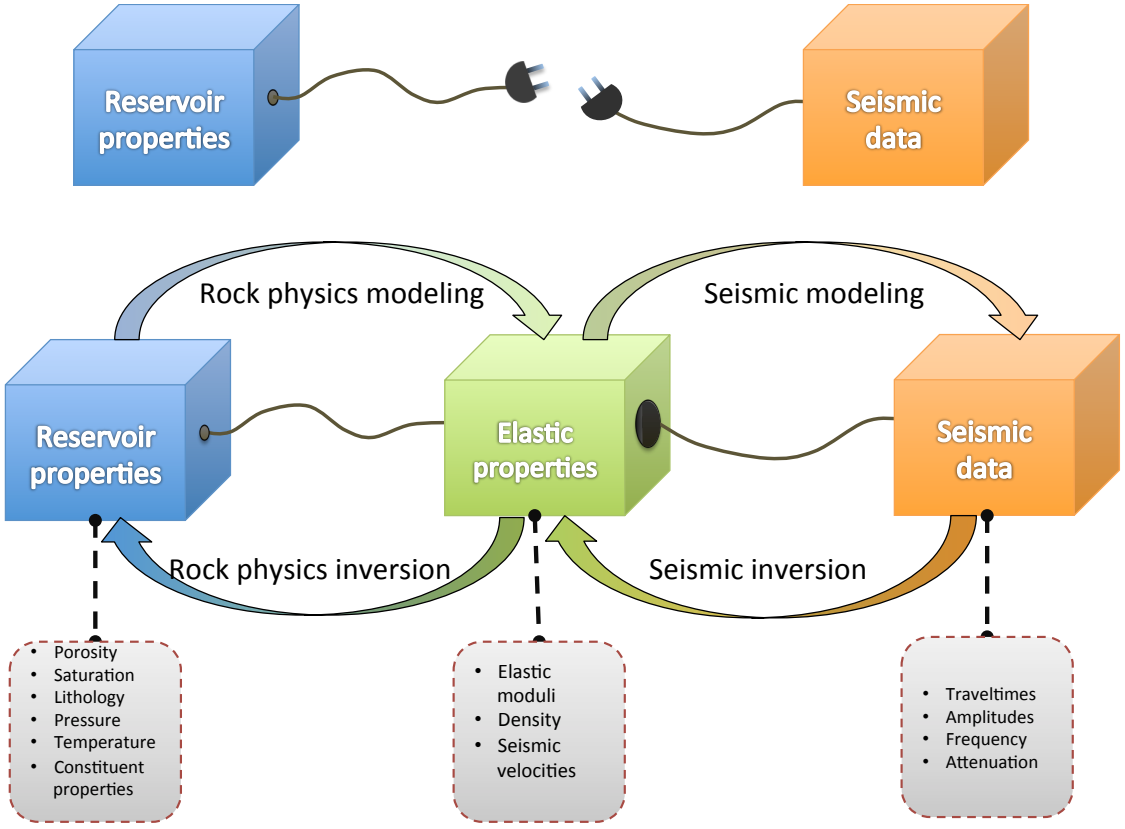

Figure 1.1: The integrated approach delineates how the various parameter domains are linked together by rock physics and seismic modeling. It represents a simple workflow scheme for reservoir characterization that clusters transformations as junctions between the various parameter domains. Examples of model parameters within each domain are given in the grey boxes. Adapted from Gelius and Johansen (2010).

A forward rock physics model attempts to predict the elastic behavior (e.g. elastic moduli, seismic velocities, density) of rocks from a description of reservoir properties (e.g. porosity, constituent properties, saturation). Thus, the model parameters are input while data parameters are output. However, rocks are by nature made very heterogeneous, and rock physics models are restricted to consider a confined set of model parameters to describe the heterogeneity without loosing its practical simplicity (Guéguen and Palciauskas, 1994). Hence, careful usage of rock physics is required to obtain approaches of seismic

observables with success (Avseth et al., 2005).

In a reservoir characterization context, reservoir properties should ideally be estimated from geophysical observables. Hence, rock physics must be solved backwards, i.e. solving an inverse problem. However, the number of model parameters used to describe heterogeneities in a rock outnumbers the data parameters describing its physical behavior. Moreover, rock physics models are non-linear functions of model parameters. This makes it impossible to straightforward turn rock physics upside-down to estimate model parameters from acquired data parameters (Johansen et al., 2011).

In spite of these issues, several approaches are however used to predict reservoir quality and lithology from geophysical observations. Ødegaard and Avseth (2003) developed a *rock physics template* analysis where observational data is cross plotted along modeled data using customized rock physics models, and by studying correlations within these plots one can make interpretations of reservoir properties. Another alternative is to use *statistical rock physics*, e.g. a Bayesian inversion type (Avseth et al., 2005; Tarantola, 2005). Here, the concept is to obtain statistical correlations based on data fitting of a set of training data where both data and model parameters are well described, and which subsequently are used for reservoir characterization. Furthermore, a strategy proposed by Johansen et al. (2004) were further adapted by Johansen et al. (2011) to introduce an approach referred to as *inverse rock physics modeling* (IRPM). The IRPM approach consists essentially by considering rock physics constraints represented as functions of model parameters from a set of observational data that are correlated to interpret reservoir properties. This approach will be applied through this thesis.

As to modeling simplifications and uncertainties in observation data, inverse solutions of reservoir quality and lithology are characterized by non-uniqueness. Hence, specialists that apply IRPM for reservoir characterization must be highly compatible to recognize and be aware of underlying reasons causing non-unique solutions to minimize distorted interpretations. Highlighting these issues is therefore of vast importance besides learning the procedure of the approach itself. For instance, when defining a rock physics model for an area, lack of information about required input parameters force us to assign reasonable values based on assumptions, nearby well data and experience (Avseth et al., 2005). If however the properties defined in the model deviate significantly from the real case scenario, inconsistencies in the rock physics constraints lead to erroneous inverse solutions. The IRPM approach makes it functional to investigate the non-uniqueness of rock physics modeling and influence of model and observational data uncertainties.

One of the most recent technical contributions for enhanced oil recovery is four-dimensional (4D) seismic to surveillance the temporal variations in fluid saturation and pressure during production. This helps to map the fluid mobility so that optimized placement of injection and production wells can be made (Gelius and Johansen, 2010). Especially in complex reservoirs, huge oil amounts are left behind after production as the fluid distribution is inadequately mapped. Rock physics is vital

in 4D reservoir characterization as it serve as a tool for interpreting observations (Bjørlykke, 2010). Hence, rock physics constraints can be modified to predict reservoir properties that usually alter during production by the IRPM approach. Subsequently, when a set of time-lapse observations data are available, the changes occurred in the reservoir can be quantified by analyzing the corresponding inverse solutions of each data set. However, in lack of repeated observations, hybrid synthetic modeling has been applied to consider the impact of production effects on initial observations.

1.2 Main objectives

The main objectives of the thesis is to:

- Give a thorough review of the inverse rock physics modeling (IRPM) approach of Johansen et al. (2011).
- Use the functional features of IRPM to emphasize the non-uniqueness of predicting reservoir quality and lithology from observational data.
- Study how uncertainties in defining reservoir parameters can influence the inverse solutions.
- Suit the rock physics modeling for reservoir monitoring applications to study simulated production effects on observational data from Glitne, North Sea.

1.3 Thesis outline

The thesis is divided in to chapters where the focus of each chapter is:

In chapter 1 to give the motivation and main objectives of thesis.

In chapter 2 to review relevant elasticity and rock physics theory.

In chapter 3 to scrutinize the IRPM approach.

In chapter 4 to test the IRPM approach using synthetic data and where effects of reservoir parameter uncertainties are studied.

In chapter 5 to adapt the IRPM to applications in reservoir monitoring to study simulated production effects on Glitne observational data.

In chapter 6 to discuss and conclude the main findings of this study.

Chapter 2

Background theory

2.1 Outline

The purpose of this chapter is to provide background theory to support understanding the inverse rock physics modeling (IRPM) approach. Basic knowledge about elastic theory is fundamental to understand concepts of seismic data and its link to rock physics and reservoir characterization and monitoring. Sections 2.2 and 2.3 reviews elastic media and the elastic wave equation. Following, section 2.4 introduce rock physics in general and the most commonly used models for dry rocks. Section 2.5 introduce the Gassmann (1951) model for fluid saturated rocks.

2.2 Stress, strain and Hooke's law

The content of this section is extracted from Auld (1990) and Pujol (2003). Elasticity theory provides the link between the rock physics parameters and the seismic parameters, i.e. the connection between the two rightmost domains in figure 1.1. Hence, this theory builds the foundation in the study of modern use of seismic. Even though this thesis concern is rock physics theory, it is still an advantage to see the whole picture of the integrated approach. Thus, elasticity theory is reviewed in this and the following section.

Elasticity theory describes how a material deforms under applied stress, and how it returns to its original form when releasing the stress. The oscillatory motions of a medium, e.g. seismic waves, is caused to a rise in elastic restoring forces when particles in a medium are displaced from its equilibrium positions. A quantitative definition of the particle displacement field $\boldsymbol{u}$ is given as

$$\boldsymbol{u}(\boldsymbol{L}, t) = \boldsymbol{l}\left(\boldsymbol{L}, t\right) - \boldsymbol{L}, \tag{2.1}$$

where $\boldsymbol{L}$ and $\boldsymbol{l}$ denotes the position vectors of the initial and new positions, respectively, and t is time. Thus, $\boldsymbol{u}$ describes how particles within a medium are vibrating through time. Furthermore, elastic waves represent infinitesimal material deformations that can be quantified by the strain tensor $\boldsymbol{\epsilon}$ as follows

$$\boldsymbol{\epsilon} = \epsilon_{ij} = \frac{1}{2}\left(\frac{\partial u_i}{\partial r_j} + \frac{\partial u_j}{\partial r_i}\right), \qquad i, j = x, y, z, \tag{2.2}$$

where the components ϵ_{ij} is the strain components. A connection between $\boldsymbol{u}$ and $\boldsymbol{\epsilon}$ is given by the strain-displacement relation,

$$\begin{aligned} \epsilon_I = \nabla_{Ij} u_j, \qquad & I = 1, 2, 3, 4, 5, 6, \\ & j = x, y, z, \end{aligned} \tag{2.3}$$

where ∇_{Ij} is the symmetric gradient operator, often denoted ∇_S. Be aware that (2.2) is denoted in

full subscript notation, whereas (2.3) has abbreviated notation.

The stress tensor $\boldsymbol{\sigma}$ gives the state of stress for any particles in a body. It consist of the stress components $\sigma_{ij}(i, j = x, y, z)$ acting on a surface i in direction j of the volume elements that represents a bodies particles. For an arbitrarily oriented surface with normal $\hat{\boldsymbol{n}}$, a traction force vector σ_n can be found from

$$\sigma_n = \sigma_{ij} n_j. \tag{2.4}$$

A change in material volume corresponds to a non-zero quantity of the diagonal elements in $\boldsymbol{\sigma}$ and $\boldsymbol{\epsilon}$, while a change in shape is given by the off-diagonal elements.

When dealing with small stress and strain in a perfectly elastic medium, a constitutive law called Hooke's law states the existence of a linear stress-strain relationship. In general Hooke's law is

$$\sigma_{ij} = c_{ijkl}\epsilon_{kl}, \qquad i, j, k, l = x, y, z, \tag{2.5}$$

where c_{ijkl} is a 6×6 matrix containing constants describing the stiffness of a medium, with i and j as free subscripts, and summation over k and l. This implies a matter of $3 \times 3 \times 3 \times 3 = 81$ elastic constants. However, from equation 2.2 the strain tensor must be symmetric, i.e. $\epsilon_{kl} = \epsilon_{lk}$, and only holds six independent components, which also is valid for the stress tensor, i.e. $\sigma_{ij} = \sigma_{ji}$. This means that $c_{ijkl} = c_{ijlk} = c_{jikl} = c_{jilk}$ and thereby a reduction to $6 \times 6 = 36$ elastic constants is achieved. Moreover, the existence of elastic potential gives that $c_{ijkl} = c_{klij}$ and further reduces the number of elastic constants down to 21. Nevertheless, only the most complex anisotropic mediums requires 21 constants in order to be properly described. In case of an isotropic medium, only two constants are needed.

The elastic stiffness constants can be expressed in terms of elastic moduli such as the bulk moduli K, shear moduli μ, Young's modulus E, Poisson's ratio v, and if the medium is isotropic it can be described by the Lamé constant λ and shear moduli μ. Definitions and relationships between elastic constants are summarized in table 2.1.

Elastic constant	K	μ	E	v	λ
Definition	$-V\frac{\delta P}{\delta V}$	$\frac{\sigma_{xy}}{2\epsilon_{xy}}$	$\frac{\sigma_{zz}}{\epsilon_{zz}}$	$-\frac{\epsilon_{xx}}{\epsilon_{zz}}$	$K-\frac{2}{3}\mu$

	K,μ	E,v
K	K	$\frac{E}{3(1-2v)}$
μ	μ	$\frac{E}{2(1-v)}$
E	$\frac{9K\mu}{3K+\mu}$	E
v	$\frac{3K-2\mu}{2(3K+\mu)}$	v

Table 2.1: Upper: definitions of elastic constants. V and P are volume and pressure, respectively. Lower: relationship between elastic constants. Modified from Guéguen and Palciauskas (1994).

2.3 Elastic waves

The content of this section is extracted from Auld (1990). To examine how an elastic material vibrates as a function of time one must relate the particle displacement $\boldsymbol{u}$ to the applied stress $\boldsymbol{\sigma}$ through Newstons 2. law, $\boldsymbol{F} = m\boldsymbol{a}$, where $\boldsymbol{F}$ is force, m material mass and $\boldsymbol{a}$ the particle acceleration, which on integral form is

$$\iint_{\delta S} \boldsymbol{\sigma}\cdot\hat{\boldsymbol{n}}\; dS + \iiint_{\delta V} \boldsymbol{F}\; dV = \iiint_{\delta V} \rho\frac{\partial^2\boldsymbol{u}}{\partial t^2}\; dV, \tag{2.6}$$

for a volume element with volume V, surface area S with normal vector $\hat{\boldsymbol{n}}$ and density ρ. The surface integral term in (2.6) can be transformed to a volume integral by applying the Gauss theorem

$$\iint_{\delta S} \boldsymbol{\sigma}\cdot\hat{\boldsymbol{n}}\; dS = \iiint_{\delta V} \nabla\cdot\boldsymbol{\sigma}\; dV. \tag{2.7}$$

Now, the integrals can be eliminated and a differential form of (2.6) is obtained by following

$$\nabla\cdot\boldsymbol{\sigma} = \rho\frac{\partial^2\boldsymbol{u}}{\partial t^2} - \boldsymbol{F}, \tag{2.8}$$

which is known as the translational equation of motion. Furthermore, by differentiating (2.8) with respect to time t and introducing particle velocity $\boldsymbol{v} = \frac{\partial\boldsymbol{u}}{\partial t}$, (2.8) becomes

$$\nabla\cdot\frac{\partial\boldsymbol{\sigma}}{\partial t} = \rho\frac{\partial^2\boldsymbol{v}}{\partial t^2} - \frac{\partial\boldsymbol{F}}{\partial t}. \tag{2.9}$$

To eliminate the term $\frac{\partial\sigma}{\partial t}$ equations (2.3) and (2.5) are used to produce a wave equation as follows

$$\text{From (2.5)} \rightarrow (\boldsymbol{\sigma} = \boldsymbol{c}:\boldsymbol{\epsilon}) : \frac{1}{\boldsymbol{c}} \Rightarrow \boldsymbol{\epsilon} = \frac{1}{\boldsymbol{c}} : \boldsymbol{\sigma}, \tag{2.10}$$

$$\text{From (2.3)} \rightarrow \boldsymbol{\epsilon} = \nabla_s\boldsymbol{u} \xrightarrow{\frac{\partial}{\partial t}} \nabla_s\boldsymbol{v} = \frac{\partial\boldsymbol{\epsilon}}{\partial t} \xrightarrow{(2.10)} \nabla_s\boldsymbol{v} = \frac{1}{\boldsymbol{c}} : \frac{\partial\boldsymbol{\sigma}}{\partial t}. \tag{2.11}$$

Multiplying (2.11) by $\boldsymbol{c}$ and substitute into (2.9) gives the general elastic wave equation for $\boldsymbol{v}$;

$$\nabla \cdot \boldsymbol{c} : \nabla_s \boldsymbol{v} = \rho \frac{\partial^2 \boldsymbol{v}}{\partial t^2} - \frac{\partial \boldsymbol{F}}{\partial t},$$

or, in abbreviated notation,

$$\nabla_{iK} c_{KL} \nabla_{Lj} v_j = \rho \frac{\partial^2 v_i}{\partial t^2} - \frac{\partial}{\partial t} F_i. \tag{2.12}$$

Equation (2.12) is a complex partial differential equation which is quite cumbersome to solve. However, assuming a body force $\boldsymbol{F} = 0$ and a plan harmonic wave with phase velocity $v = \frac{\omega}{k}$, where ω is angular frequency and k is the wavenumber[1], on the form

$$\boldsymbol{v} \propto \boldsymbol{r} e^{i(\omega t - \boldsymbol{k} \cdot \boldsymbol{r})}, \tag{2.13}$$

reduce the problem of finding wave velocity and polarization down to an eigenvalue problem. Say that the direction of propagation is given by $\hat{\boldsymbol{l}}$ and that time and spatial derivatives transforms to multiplication with angular frequency and wave number respectively, i.e. $\frac{\partial}{\partial t} \to i\omega$ and $\frac{\partial}{\partial x_j} \to -ik$. Consequently, the symmetric gradient operator ∇_{Lj} and its transpose, divergence of stress operator ∇_{iK}, may be replaced by matrices $-ikl_{Lj}$ and $-ikl_{iK}$ respectively, and substituted into (2.12) to give

$$\begin{gathered} k^2 l_{iK} c_{KL} l_{Lj} v_j = \rho \omega^2 v_i, \\ \Updownarrow \\ k^2 \tau_{ij} v_j = \rho \omega^2 v_i. \end{gathered} \tag{2.14}$$

This is called the Christoffel equation where $\tau_{ij} = l_{iK} c_{KL} l_{Lj}$ represents the Christoffel matrix. The eigenvalues of τ_{ij} corresponds to the phase velocity of the P, SV and SH waves, while its eigenvectors states the polarization. The Christoffel equation applies to plane wave solutions in both isotropic and anisotropic media specified by the stiffness tensor c_{KL}.

If the stiffness tensor c_{KL} defines an isotropic material, equation (2.14) simplifies to two simple expressions;

$$V_P = \sqrt{\frac{K + \frac{4}{3}\mu}{\rho}}, \tag{2.15a}$$

$$V_S = \sqrt{\frac{\mu}{\rho}}. \tag{2.15b}$$

These two equations are frequently used in rock physics modeling since the effective medium theory assumes the volume of rock to be homogenous and elastically isotropic.

[1] $k = \frac{2\pi}{\lambda}$, where λ is the wavelength.

As an elastic wave propagates through an isotropic medium and encounters an interface where a new isotropic medium with discriminated physical properties begins, some of the energy from the wave will be reflected upwards to the surface. The reflected energy creates the foundation for reflection seismic studies. The amount of reflected and transmitted energy can respectively be expressed by reflection and transmission coefficients. The most trivial case is when having various isotropic mediums with velocities V_n and densities ρ_n, where index n refers to a specific medium. If an incident wave hits an interface between two such mediums perpendicularly, the reflection coefficient becomes

$$R = \frac{V_{n+1}\rho_{n+1} - V_n\rho_n}{V_{n+1}\rho_{n+1} + V_n\rho_n}, \quad -1 \leq R \leq 1, \tag{2.16}$$

where negative signs of R emphasize a phase shift of 180° in the reflected wave.

A reflected wave cannot capture unlimited physical variations in the subsurface, which leads us to the subject of seismic resolution. It can be separated into what the wave can discriminate in the horizontal and vertical directions. For the horizontal direction, the wave can not distinguish two features closer than of $R_F = \left(\frac{VZ}{2f}\right)^{\frac{1}{2}}$, called the *Fresnel zone*, where Z and f respectively are depth to object and frequency of the wave. Furthermore, the vertical resolution defines the ability to separate two features. If the thickness of a layer is smaller than $\lambda/4$, where λ is the wavelength, the reflectors corresponding the upper and lower layer interface can not be discriminated and only one reflector appears. Hence, the layer will not be correctly interpreted.

2.4 Rock physics modeling

The content of this section is mainly extracted from Guéguen and Palciauskas (1994), Mavko et al. (2009) and Gelius and Johansen (2010). Rock physics theory provides a link between the elastic properties and the reservoir properties, i.e. the connection of the two leftmost domains in figure 1.1. The field of research in this thesis is within these domains, and a thorough description of basic rock physics is therefore following.

A body of rock is by nature characterized by its heterogeneity. A confident description of the physical behavior of a rock strongly depends on the level of heterogeneity, which subsequently rely on the scale considered. For instance, from analyzing a reservoir rock through a microscope one typical finds it to consist of multi-mineralic components and pores saturated with various fluids (i.e. the reservoir properties). However, a seismic wave at a tens-of-meters to hundreds-of-meters scale is because of restricted seismic resolution not capable of capturing microscopic irregularities present, but is rather recording a macroscopic average (i.e. effective elastic properties) where constituents are randomly distributed (see figure 2.1). Random distribution of constituents at a micro scale appears as an effective elastically isotropic medium at a macro scale. Hence, the seismic image of the macroscopic effective rock exhibits

a homogenous reservoir rock, although it usually occurs layered (dashed red lines in figure 2.1). This emphasize the scale dependencies of rock physics and illuminate that assumed simplifications usually are unequal the complex reality.

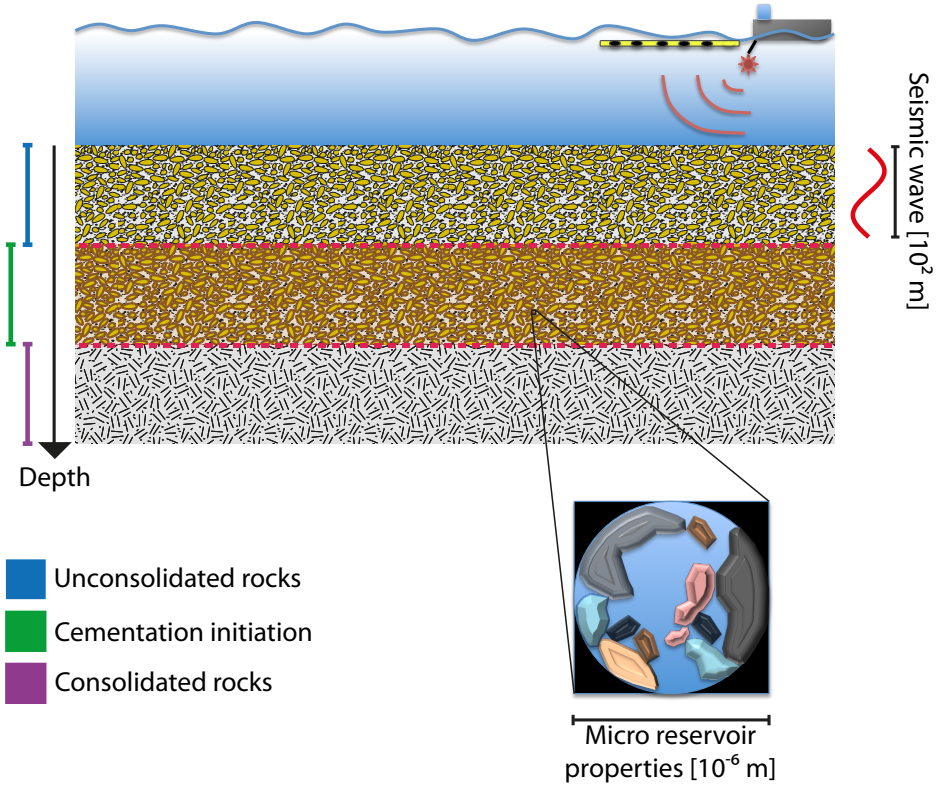

Figure 2.1: A marine seismic acquisition over a geological outcrop composed of several layers with different physical properties. The layers are separated by red dashed lines.

A representative volume element (RVE) of a rock is used to describe the average properties of a rock as a homogenous and elastically isotropic volume. The most familiar techniques for down-scaling of seismic measurements to predict the effective properties on a RVE is based on effective medium theory (Jakobsen et al., 2000), referred to as forward rock physics modeling. Due to the wide span of constituent properties and geometrical distribution, the physics of a rock can be quite differently. Thus, numerous rock physics models have been constructed to best describe the various conditions. However, they are commonly limited to be functions of the following: (1) the volume fractions of e.g. n constituents $V_1, V_2, \ldots, V_n$, (2) their elastic moduli $M_1, M_2, \ldots, M_n$, and (3) details of their relative geometrical arrangement to each other.

The geometrical details are in practice not sufficiently implemented into rock physics models, although several theories deal with simplifications and approximations. When information from only (1) and (2) are available, one may estimate the elastic moduli upper and lower bounds. At any specified volume fraction of the various phases, the exact elastic moduli will lie within these bounds and depends on the geometrical details (Mavko et al., 2009). However, these bounds are extremely reliable and robust, and have contributed to be a superior rock physics tool (Avseth et al., 2005). The first upcoming

sections reviews such bounds, continuing with more advanced rock physics models where geometrical details are to some extent incorporated.

Basically, one may group the rock physics models according to consolidated or unconsolidated rocks, a mixture of these, or empirical models (Johansen et al., 2011). Several published papers has tested the validation of different theories for different rock types. Inclusion models is made for consolidated rocks, and works adequate for sandstones (Dræge et al., 2006), carbonates (Agersborg et al., 2008) and shales (Hornby et al., 1994). Likewise, unconsolidated rocks are described by contact theories (Walton, 1987; Digby, 1981; Mindlin, 1949), whereas contact cement theory (Dvorkin et al., 1991) is used for weakly consolidated rocks.

2.4.1 Voigt-Reuss-Hill average moduli estimate

The Reuss (1929) and Voigt (1928) models give the absolute lower and upper bounds, respectively, for the elastic moduli of isotropic or anisotropic media. To illustrate, imagine a mix of soft and stiff components, e.g. shale and sandstone respectively, that have been layered both horizontally and vertically sequentially (see figure 2.2). Let V_1, V_2 and M_1, M_2 be the volume fractions and bulk or shear moduli of the sandstone and shale, respectively.

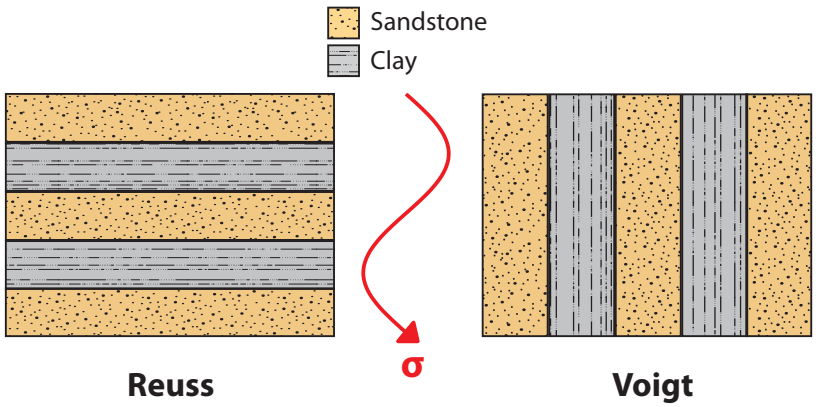

Figure 2.2: A stress $\boldsymbol{\sigma}$ is applied on an alternating body of sandstone and shale in two cases where the layers are perpendicular and parallel to the stress. The body achieves a minimum and maximum stiffness when layers are perpendicular and parallel to $\boldsymbol{\sigma}$, respectively.

Reuss model considers the elastic moduli when stress $\boldsymbol{\sigma}$ is applied normal to the horizontally aligned layers. The properties of the soft shale then dominates, resulting in a varying strain, while the stress is constant. The effective elastic moduli then gets a lower limit given by (Reuss, 1929)

$$\frac{1}{M_{\text{Reuss}}} = \frac{V_1}{M_1} + \frac{V_2}{M_2}. \tag{2.17}$$

Conversely, Voigt's model computes the elastic moduli when the stress is applied perpendicular to vertically aligned layers, giving the dominance to the stiff sandstones properties. The upper limit for

the elasticity of the rock then becomes

$$M_{\text{Voigt}} = V_1 M_1 + V_2 M_2. \tag{2.18}$$

In general, for N phases the Reuss and Voigt bounds are given as

$$M_{\text{Reuss}} = \left[\sum_{n=1}^{N} \frac{V_n}{M_n} \right]^{-1} \tag{2.19a}$$

$$M_{Voigt} = \sum_{n=1}^{N} V_n M_n. \tag{2.19b}$$

Finally, the Hill (1963) average is the arithmetic mean between M_{Reuss} and M_{Voigt};

$$M_{\text{Hill}} = \frac{1}{2}(M_{Reuss} + M_{Voigt}). \tag{2.20}$$

For any elastic material, the effective modulus M^* will always be $M_{Reuss} \leq M^* \leq M_{Voigt}$.

2.4.2 Hashin-Shtrikman bounds

The optimal bounds for an perfect elastically isotropic composite are the Hashin-Shtrikman bounds (Hashin and Shtrikman, 1963). A physical interpretation of these two bounds is that one of the constituents is embedded in the other, forming an outer and inner spherical core, as seen in figure 2.3. A medium may be viewed to compose exclusively of such embedded spheres with varying diameter, so that all void vanish at a microscopic scale. On the macroscopic scale however, the medium appears homogenous with its effective Hashin-Shtrikman upper bounds given by

$$K^{HS+} = K_1 + \frac{V_2}{(K_2 - K_1)^{-1} + V_1 \left(K_1 + \frac{4}{3}\mu_1\right)^{-1}}, \tag{2.21a}$$

$$\mu^{HS+} = \mu_1 + \frac{V_2}{(\mu_2 - \mu_1)^{-1} + 2V_1 (K_1 + 2\mu_2) \left[5\mu_1 \left(K_1 + \frac{4}{3}\mu_1\right)\right]^{-1}}, \tag{2.21b}$$

where the bulk moduli K, shear moduli μ and volume fractions V have indices 1 and 2 that corresponds to the stiffest and softest material respectively, i.e. $K_1 > K_2$ and $\mu_1 > \mu_2$. An interchange of these, i.e. indices 1 and 2 represents the softest and stiffest material respectively, in (2.21a) and (2.21b), gives the Hashin-Shtrikman lower bounds (HS^-).

The Hashin-Shtrikman bounds given by equations (2.21a) and (2.21b) can be written in a more general form called the Hashin-Shtrikman-Walpole bounds (Walpole, 1966a,b). The elastic moduli are then given by

$$K = K_1 + \frac{V_2}{(K_2 - K_1)^{-1} + V_1 \left(K_1 + \frac{4}{3}\mu_m\right)^{-1}} \tag{2.22a}$$

$$\mu = \mu_1 + \frac{V_2}{(\mu_2 - \mu_1)^{-1} + V_1 \left[\mu_1 + \frac{\mu_m}{6}\left(\frac{9K_m + 8\mu_m}{K_m + 2\mu_m}\right)\right]^{-1}}, \tag{2.22b}$$

where the index 1 and 2 refers to the two components. The upper bound is found when K_m and μ_m are the maximum bulk and shear moduli of the two components, whereas the lower bound is found when they have the minimum value. Consequentially, it is possible that $\mu_2 > \mu_1$ and $K_2 < K_1$, where the indices 1 and 2 refers to the stiffest and softest material, respectively.

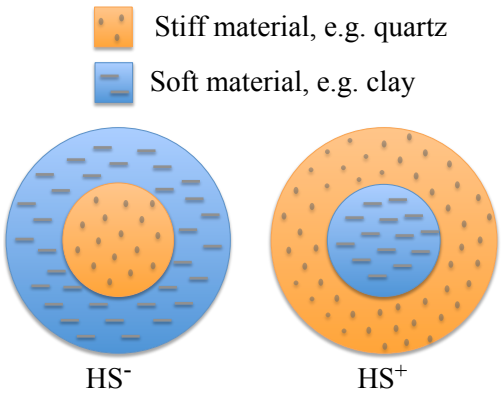

Figure 2.3: A physical interpretation of the upper and lower Hashin-Shtrikman upper (HS^+) and lower (HS^-) bounds.

2.4.3 Direct calculation

By direct calculations the effective elastic moduli is found directly from Hooke's law (2.5). Consider a simple two-phase inclusion model as in figure 2.4, containing a mono-mineralic matrix and spherical pores with volume factions V_1 and V_2, respectively.

Assume that both phases are isotropic and elastic, and that the seismic waves has a wavelength $\lambda \gg (V_1 + V_2)$ on a mini scale (10^{-3} m) where Hooke's law can be written on average form as

$$\bar{\sigma} = M^* \bar{\epsilon}, \tag{2.23}$$

where M^* can be bulk or shear elastic moduli. The average stress and strain are then

$$\bar{\sigma} = \bar{\sigma}^{(1)} V_1 + \bar{\sigma}^{(2)} V_2, \tag{2.24a}$$

$$\bar{\epsilon} = \bar{\epsilon}^{(1)} V_1 + \bar{\epsilon}^{(2)} V_2, \tag{2.24b}$$

where (1) and (2) denotes respectively matrix and inclusion phase. If M_1 and M_2 are the respective elastic moduli of the two phases, the effective modulus M^* can be found by substituting (2.24a) into (2.23) and further reformulate this expression by using equation (2.24b) to eliminate the matrix volume;

$$M^* = M_1 + (M_2 - M_1)\frac{\bar{\epsilon}^{(2)}}{\bar{\epsilon}}V_2. \tag{2.25}$$

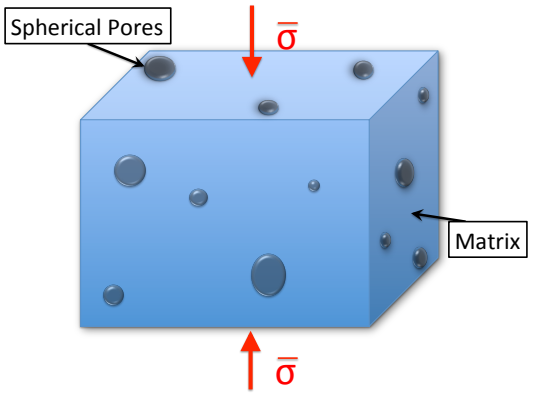

Figure 2.4: A simple two-phase inclusion model composed of matrix and pores. $\bar{\boldsymbol{\sigma}}$ describes the average stress in equation 2.23.

Furthermore, if its assumed that $V_2 < 0.1$ and no physical interactions between the pores occur, the volume strain term in (2.25) has a solution (Landau and Lifshitz, 1967)

$$\frac{\bar{\epsilon}^{(2)}}{\bar{\epsilon}} = \frac{3K_1 + 4\mu_1}{3K_2 + 4\mu_1}. \tag{2.26}$$

When (2.26) goes into (2.25), an expression for the effective elastic moduli M^* is achieved. For a dry rock, $K_2 = 0$, $V_2 = \phi$, the effective elastic modulus becomes

$$M^* = M_1\left[1 - \left(1 + \frac{3K_1}{4\mu_1}\right)\phi\right]. \tag{2.27}$$

Equation (2.27) do not incorporate with elastic moduli at a seismic scale (i.e. macro scale). Hence, it do not work consistently to predict the response of seismic waves. It only works under the restricted assumptions given above, and becomes erroneous with increasing heterogeneity (e.g. more than two phases, larger pore volume, non-spherical pore geometries, etc.).

2.4.4 Self-consistent approach (SCA)

With the assumptions $V_2 < 0.1$ and no pore interactions of the inclusion model in section 2.4.3 being neglected, (2.26) fails to hold. Instead, the method of SCA replaces the elastic moduli of the matrix, i.e. K_1 and μ_1, with the rocks effective moduli, K^* and μ^*, so the strain volume term becomes

$$\frac{\bar{\epsilon}^{(2)}}{\bar{\epsilon}} = \frac{3K^* + 4\mu^*}{3K_2 + 4\mu^*}. \tag{2.28}$$

The theory considers that the pores are embedded into the effective medium instead of the matrix, and thereby it incorporate interactions between the pores. Subsequently, (2.28) yields a more accurate

approximation than (2.26). Applying (2.28) in (2.25) gives an expression for K^* and another for μ^*, which can both be solved by a self-consistent approximation for K^* and μ^* (Guéguen and Palciauskas, 1994). SCA is based upon scattering theory which considers the scattered elastic energy transmitted from the inclusions as elastic waves propagates through the rock volume.

2.4.5 Differential effective medium (DEM) theory

The differential effectium medium inclusion theory (Bruggemann, 1935) is based on the Kuster-Toksöz (KT) scattering model of first order. When a plane P-wave propagates through a medium consisting of a matrix and pores, the pores generates scattered of energy transmitted as P and S waves. The KT model basically sums up the incident and scattered waves from the pores to give the net scattering (Gelius and Johansen, 2010). A general expression for the effective elastic moduli K^*_{KT} and μ^*_{KT} for a spectrum of aspect ratios[1] α is given by

$$(K^*_{KT} - K_m)\frac{\left(K_m + \frac{4}{3}\mu_m\right)}{\left(K^*_{KT} + \frac{4}{3}\mu_m\right)} = \sum_{i=1}^{N} v_i\,(K_i - K_m)\,P^{mi}, \tag{2.29a}$$

$$(\mu^*_{KT} - \mu_m)\frac{(\mu_m + \zeta_m)}{(\mu^*_{KT} + \zeta_m)} = \sum_{i=1}^{N} v_i\,(\mu_i - \mu_m)\,Q^{mi}, \tag{2.29b}$$

where indices m and i represents the matrix and the various pore contents respectively, and P^{mi} and Q^{mi} is the geometrical factors specified in table 2.2.

Pore shape	P^{mi}	Q^{mi}
Spheres	$\frac{K_m+\frac{4}{3}\mu_m}{K_i+\frac{4}{3}\mu_m}$	$\frac{\mu_m+\zeta_m}{\mu_i+\zeta_m}$
Needles	$\frac{K_m+\mu_m+\frac{1}{3}\mu_i}{K_i+\mu_m+\frac{1}{3}\mu_i}$	$\frac{1}{5}\left(\frac{4\mu_m}{\mu_m+\mu_i} + 2\frac{\mu_m+\gamma_m}{\mu_i+\gamma_m} + \frac{K_i+\frac{4}{3}\mu_m}{K_i+\mu_m+\frac{1}{3}\mu_i}\right)$
Disks	$\frac{K_m+\frac{4}{3}\mu_i}{K_i+\frac{4}{3}\mu_i}$	$\frac{\mu_m+\zeta_i}{\mu_i+\zeta_i}$
Penny cracks	$\frac{K_m+\frac{4}{3}\mu_i}{K_i+\frac{4}{3}\mu_i+\pi\alpha\beta}$	$\frac{1}{5}\left(1 + \frac{8\mu_m}{4\mu_i+\pi\alpha(\mu_m+2\beta_m)} + 2\frac{K_i+\frac{2}{3}(\mu_i+\mu_m)}{K_i+\frac{4}{3}\mu_i+\pi\alpha\beta_m}\right)$

Table 2.2: Coefficients P and Q for some given shapes[2]. The indices m and i refer to the matrix and inclusion materials respectively. Adapted from Mavko et al. (2009).

The KT model is however only based on first order scattering, so the inclusion scatterings that interacts each other are not included. Here, DEM theory propose to solve that issue by stepwise embedding a volume fraction of inclusions within the matrix and run the KT model to compute the effective elastic moduli. This composite is within the next step considered to represent the new matrix, as a new set of inclusions of equvalent aspect ratio are added, and the same process is repeated over again. The

[1] The aspect ratio describes the shape of a pore, and is defined as $\alpha = \frac{a}{b}$, where a and b is the minor and major axis for a pore, respectively.

[2] $\beta = \mu\frac{(3K+\mu)}{(3K+4\mu)}$, $\gamma = \mu\frac{(3K+\mu)}{(3K+7\mu)}$, $\zeta = \frac{\mu}{6}\frac{(9K+8\mu)}{(K+2\mu)}$.

effective elastic moduli is then given after all the inclusions are included in the computations. Note that this model is asymmetric, i.e. an interchange of the matrix with one of the embedding components and subsequently applying DEM theory, leads to a different elastic moduli. For a two-phase medium the effective elastic bulk K^* and shear μ^* moduli is found from the coupled system of ordinary differential equations (Berryman, 1992) as

$$(1-y)\,\frac{d}{dy}\left[K^*(y)\right] = \left(K_2 - K^*\right) P_2^*(y), \tag{2.30a}$$

$$(1-y)\,\frac{d}{dy}\left[\mu^*(y)\right] = \left(\mu_2 - \mu^*\right) Q_2^*(y). \tag{2.30b}$$

Phase one is the host material with bulk moduli $K_1 = K^*(y=0)$ and shear moduli $\mu_1 = \mu^*(y=0)$, while phase two has K_2 and μ_2 as the bulk and shear moduli and a volume fraction given by y, which in case of fluid inclusions and voids is $y = \phi$, where ϕ is the porosity. The geometrical factors P and Q is given in table 2.2, and the index 2 indicates that the coefficients are for an inclusion of phase two in a host material with the effecitve moduli K^* and μ^*.

2.4.6 Contact theory (CT)

An appropriate way of modeling sediments right after deposition is by considering a random package of identical spherical grains (Mindlin, 1949). This applies only when sediments are buried to a depth where increasing confining pressure P_c does not cause the grains to further reorganize. Such models are referred to as contact theory (CT), where the most familiar group member is the Hertz-Mindlin model (HM). The elastic moduli of the CT models depend on the contact properties between the grains; contact stiffness, contact area and coordination number[1] C_0, - but also, the elastic properties of the grains and confining pressure P_c. The according Hertz-Mindlin effective bulk moduli for a dry package of grains is

$$K^{HM} = \left(\frac{C_0^2\left(1-\phi_0\right)^2 \mu_s^2}{18\pi^2\left(1-v_s\right)^2} P_c\right)^{\frac{1}{3}}, \tag{2.31}$$

where ϕ_0, μ_s and v_s are the critical porosity[2], shear moduli and Poisson ratio of the grain material, respectively.

Due to the resistance between grains to slip relative to each other, the shear moduli also depends on the normal stress applied on the grain package and the roughness of grains. Mindlin (1949) assumed that shear stress is applied subsequently to normal stress, and a maximum of grain friction. The effective shear moduli of the dry package of grain then becomes

[1] Coordination number C_0 is the average number of contact points for each grain.

[2] The critical porosity is the porosity of sediments at the stage of deposition. A porosity ϕ extending the critical porosity ϕ_0 leads to suspension of the material, i.e. it behaves like a fluid.

$$\mu^{HM} = \frac{5 - 4v_s}{5\,(2 - v_s)} \left(\frac{3C_0^2\,(1-\phi_0)^2\,\mu_s^2}{2\pi^2\,(1-v_s)^2} P_c \right)^{\frac{1}{3}}. \tag{2.32}$$

Another member of CT models is the Walton (1987) model which is expressed by other parameters than in the HM model. It assumes that the shear stress is added simultaneously to the normal stress, somewhat giving different results from the HM model. Furthermore, the roughness of the grain contacts are considered in two extreme cases, giving it an upper and lower limit for the elastic parameters. The upper limit is in the case of a very high friction coefficient, i.e. very rough grain contacts, giving the effective bulk and shear moduli of a dry package of grains, respectively as

$$K^{Wa+} = \frac{1}{6} \sqrt[3]{\frac{3\,(1-\phi_0)^2\,C_0^2 P_c}{\pi^4 B^2}}, \tag{2.33a}$$

$$\mu^{Wa+} = \frac{3}{5} K^{(Wa+)} \frac{5B + A}{2B + A}, \tag{2.33b}$$

where the coefficients A and B are defined as,

$$A = \frac{1}{4\pi} \left(\frac{1}{\mu_s} - \frac{1}{\mu_s - \lambda_s} \right), \tag{2.34a}$$

$$B = \frac{1}{4\pi} \left(\frac{1}{\mu_s} + \frac{1}{\mu_s - \lambda_s} \right), \tag{2.34b}$$

where λ_s is the Lamé constant of grain material. If the grain contacts are smooth, the lower bound of Walton model has an effective bulk moduli $K^{Wa-} = K^{Wa+}$ as in (2.33a), whereas the effective shear moduli is

$$\mu^{Wa-} = \frac{3}{5} K^{Wa-}. \tag{2.35}$$

2.4.7 Contact cement theory (CCT)

As granular media experience further burial, additional stiffness-influence processes occur. These are due to (1) mechanical and (2) chemical compaction which is transforming the granular structured rock to consolidated prominent rocks. The former process leads to a reorganization of grains that cause an increase of stiffness at grain contact points. The latter process is due to minerals tending to partly or completely dissolve and precipitate within the pore space and contact points, caused by the high pressure at grain contact points and high concentration of ions in the pore fluids (Kullerud, 2010). The sorting processes mainly occurs at the "unconsolidated rocks" zone in figure 2.1, whereas the cementation occurs in the "cementation initiation" zone. The cement, which may consist of the same mineral as the grains, can rim the grains in different ways (see figure 2.5), and has a substantial impact on the rock stiffness, even at modest amounts.

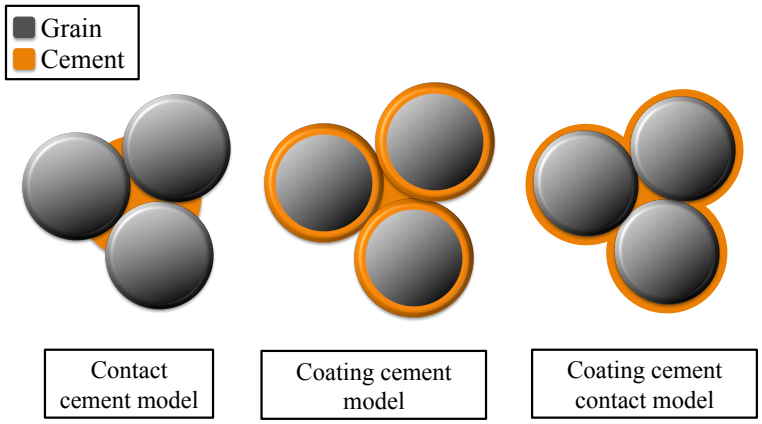

Figure 2.5: Grains that have been coated with cement, e.g. clay, before deposition is referred to as coating cement model. If the cementation occur after the grains has established contact, it is denoted a contact cement model or coating cement contact model.

Dvorkin et al. (1991) developed a contact cement theory (CCT) that delineates the effective elastic properties of a given cemented granular model, with respect to the elastic properties of the cement, its volume fraction and critical porosity (Gelius and Johansen, 2010). According to the CCT model the bulk and shear moduli are respectively

$$K^{CCT} = \frac{1}{6} C_0 \left(1 - \phi_0\right) M_c \hat{S}_n, \tag{2.36a}$$

$$\mu^{CCT} = \frac{3}{5} K^{CCT} + \frac{3C_o \left(1 - \phi_0\right)}{20} \mu_c \hat{S}_\tau, \tag{2.36b}$$

where $M_c = \rho_c V_{P_c}^2$ and $\mu_c = \rho_c V_{S_c}^2$ are the cement's compressional and shear moduli, respectively. $\hat{S}_n$ and $\hat{S}_\tau$ are both contact stiffness coefficients outlined in appendix A.

A hybrid approach can be used to predict the elasticity as function of varying porosity associated with various compaction processes. At the high porosity end member, the rock is predicted by contact theory (CT) models, whereas at zero porosity, the rock must hold the elastic moduli of the effective mineral. A Hashin-Shtrikman-Walpole (HSW) bound is thereby used to interpolate between these two end members. If contact cement is present, this approach yields however under-predicted values at the high porosity regime. Thus, a CCT model is applied at this regime (e.g. in between 0-10 % porosity reduction caused by cementation growth), and a HSW bound interpolates between the remaining gap (see figure 2.6).

The upper HSW bound describes the theoretical stiffest way of mixing the effective mineral and the grain package framework, while the lower bound corresponds to the softest way of mixing these. These trends have also been found to describe different compaction processes. The upper bound may be interpreted as chemical compaction processes causing contact cement to precipitate. The lower bound describes porosity reduction related to mechanical compaction where sorting cause smaller grains to occupy the pore space between bigger grains. These different compaction processes are found at vari-

ous deposition environments (Avseth et al., 2005). Interpretations of rock physics modeling like these may work as guidelines in the choice of rock physics models to locally constrain the data. For instance, if a well runs through a section of unconsolidated material where the porosity has decreased due to sorting, contact theory and lower HSW bound (CT/HSW$^-$) is favorable.

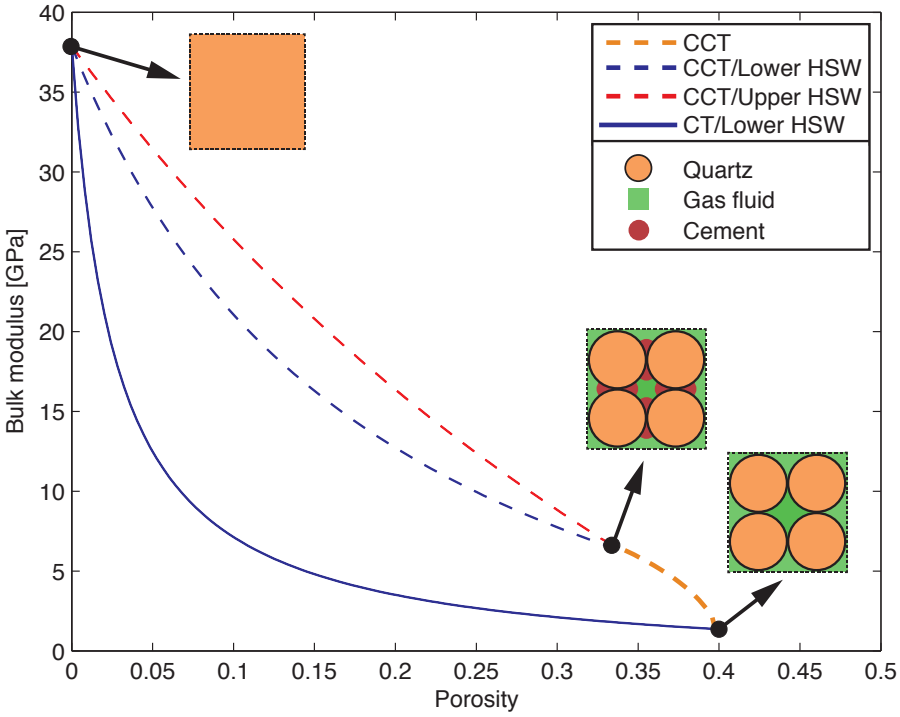

Figure 2.6: Typical trend of porosity versus bulk moduli obtained by Hashin-Shtrikman-Walpole linking the end members of CT and CCT models. The critical porosity C_0 is 0.4, and a pure gas saturation is considered. An illustration is attached to the CT and CCT end-members in the high porosity regime where HSW is bounding these to the zero porosity end-member. Avseth et al. (2005) refers to these various hybrid approaches as *the friable sand model* (CT/Lower HSW), *the constant-cement model* (CCT/Lower HSW) and *the increasing-cement model* (CCT/Upper HSW).

2.4.8 Patchy cementation

At the stage where cementation initiates at unconsolidated loose sands, the contact cement is rarely homogeneously distributed between grains. Hence, the rock is partial sensitive to pressure variations at grain contacts where no cementation yet has occurred. Avseth and Skjei (2011) propose to model such rocks by a heuristic approach where contact theory (CT) and contact cement theory (CCT) models combined with Hashin-Shtrikman-Walpole (Walpole, 1966a,b) bounds are used. The assumption is that the rock consists of a binary mixture of cemented and uncemented grain contacts, as upper and lower bounds, respectively. Whereas the lower bound is represented by connecting the high porosity contact theory end member with the mineral point, the upper bound is found by increasing the effective stress until it mimics a 10 % constant cement model (i.e. consolidated compaction). Amounts of cement between 0-10 % is considered to lie within the regime of patchy cementation where the rock will be partial pressure-sensitive. Rocks with cement amounts exceeding 10 % will be extensively

pressure-insensitive. Furthermore, Avseth and Skjei (2011) applied a linear weight method between the upper (cemented) and lower (uncemented) bounds to predict the elastic moduli of patchy cemented sandstones. An alternative approach to the linear weight method is to use a Hashin-Shtrikman bound to mix the cemented sandstone end member, predicted by the CCT model, with the end-member of unconsolidated sands, predicted by either a Hertz-Mindlin (Mindlin, 1949) or Walton model (Walton, 1987) (Avseth et al., 2012). The upper bound then represents connected cement distributed evenly between grains, whereas the lower bound represents disconnected cement concentrated locally. A Hashin-Shtrikman-Walpole lower bound is further used to interpolate between the patchy cemented sandstone and the mineral point, which emphasizes varying porosity associated with sorting. The resulting model trends are shown in figure 2.7 for both stiffest and softest isotropic mixtures (i.e. connected and disconnected patchy cement, respectively).

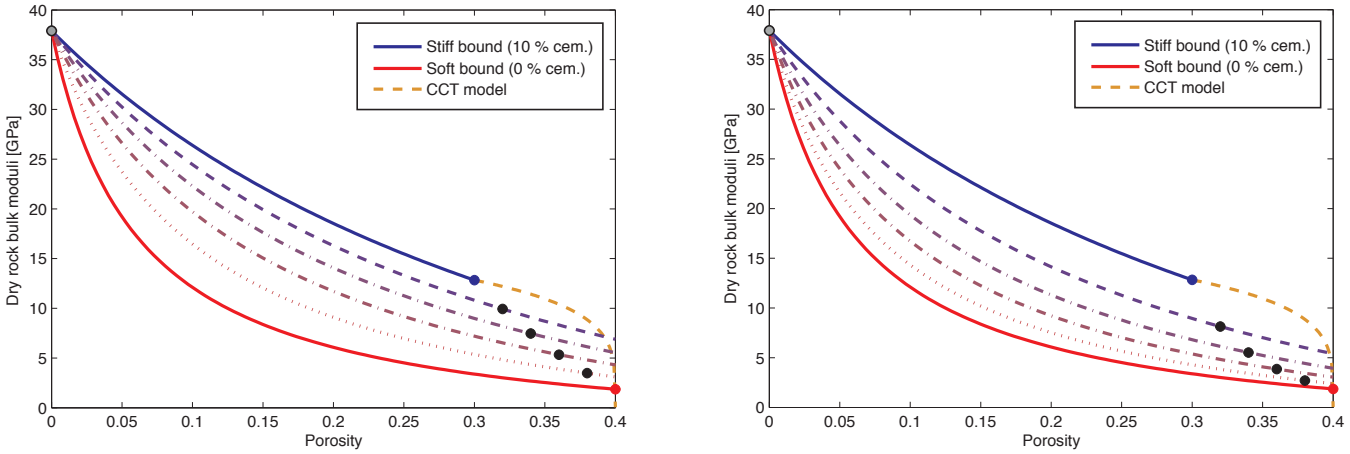

Connected patchy cement **Disconnected patchy cement**

Figure 2.7: Rock physics modeling of patchy cemented sandstone (black dots and dashed lines), composed by mixing a 10 % cemented sandstone with a pressure-sensitive unconsolidated sandstone given according to Hertz-Mindlin theory (Mindlin, 1949), at volume fractions from one (blue dots) to zero (red dots), with an increment of 0.2. The effective pressure is set to 20 MPa in the Hertz-Mindlin model.

2.5 Fluid effects

In the previous subsections 2.4.3 to 2.4.7, the rock physics models gave an effective elastic moduli for a dry rock of pores with vacuum. In this section, the model of Gassmann (1951) is proposed to predict the elastic properties when pore fluids are present.

The following assumptions must be satisfied when using the Gassman's fluid substitution recipe:

- The wavelength λ is much larger than the grains and pore space. In other words; Gassman is only valid for low frequencies where so-called local fluid flow are present,
- The rock must be isotropic,

- All the grains have equivalent physical properties,
- The pore fluid is homogenous and completely saturates the open pore space.

As a fluid do not have any response to shear strength, the Gassmann model predicts the effective shear moduli of the saturated and dry rock to be equal;

$$\mu_{sat} = \mu_d. \tag{2.37}$$

However, the effective bulk moduli of the saturated rock is

$$K_{sat} = K_d + \frac{(1 - \frac{K_d}{K_s})^2}{\frac{\phi}{K_f} + \frac{1-\phi}{K_s} - \frac{K_d}{K_s^2}}, \tag{2.38}$$

where the indices d, s and f stands for dry, solid and fluid bulk moduli, respectively, and ϕ is porosity. The K_s moduli is predefined by the mineral elastic properties, whereas K_d can be found by a rock physics model. If the fluid comprise a homogenous mixture of various fluid constituents, e.g. brine and gas, the effective bulk moduli can be found from Wood's formula (Wood, 1955). For N fluids it is

$$\frac{1}{K_f^{(W)}} = \sum_{i=1}^{N} \frac{S_i}{K_i}, \tag{2.39}$$

where S_i is the volume faction of the i-th fluid. Notice that equation (2.39) equals the Reuss lower bound (2.19a). In reality, homogenous fluid substitutions are rare, and the fluid substitution occurs in a more gradual process, referred to as patchy saturation. In such case, the fluid properties can be found by using a Hill average (Hill, 1963). For N fluids it follows,

$$K_f^{(H)} = \frac{1}{2}\left[\sum_{i=1}^{N} S_i K_i + \left(\sum_{i=1}^{N} \frac{S_i}{K_i}\right)^{-1}\right]. \tag{2.40}$$

Hence, a patchy fluid substitution yields a stiffer rock than a homogenous substitution. Notice that equation (2.40) is the arithmetic average of equations (2.19a) and (2.19b).

2.6 Summary

In this chapter we have seen how elastic moduli is linearly related to stress and strain through Hooke's law, and how this relationship is used to express an elastic wave equation where the direction, velocities and polarization of the various waves can be found. Furthermore we have presented several rock physics models that predicts the dry rock elastic moduli from a description of reservoir properties. Although there exists a myriad of rock physics theories (theoretical, empirical, hybrids, etc.), the bottom line for choosing any rock physics model is that it shall approach a description of the physical behavior of the geological scenario present. Ultimately, the Gassmann model can be applied to estimate the elastic moduli of a fluid saturated rock.

Chapter 3

The inverse rock physics modeling approach

3.1 Outline

In this chapter, the inverse rock physics modeling (IRPM) approach of Johansen et al. (2011) will be introduced. A general workflow of this approach is shown in figure 3.1. In *Step 1* a reservoir model is defined by a set of constant model parameters, hence called static model parameters, together with a set of model parameters that are allowed to vary within specified boundaries, hence called dynamic model parameters. Furthermore, a suitable rock physics model is chosen to build constraints relating the dynamic model parameters to the elastic properties, referred to as data parameters. Following in *Step 2*, a set of data parameter constraints and a set of data parameter values are input for the IRPM approach. The outcome are the solutions of dynamic model parameters that corresponds the input data parameter values. We define two different hypothetical reservoir models in step 1 in section 3.2, and these models will be used in the following sections that describes and demonstrates the IRPM approach.

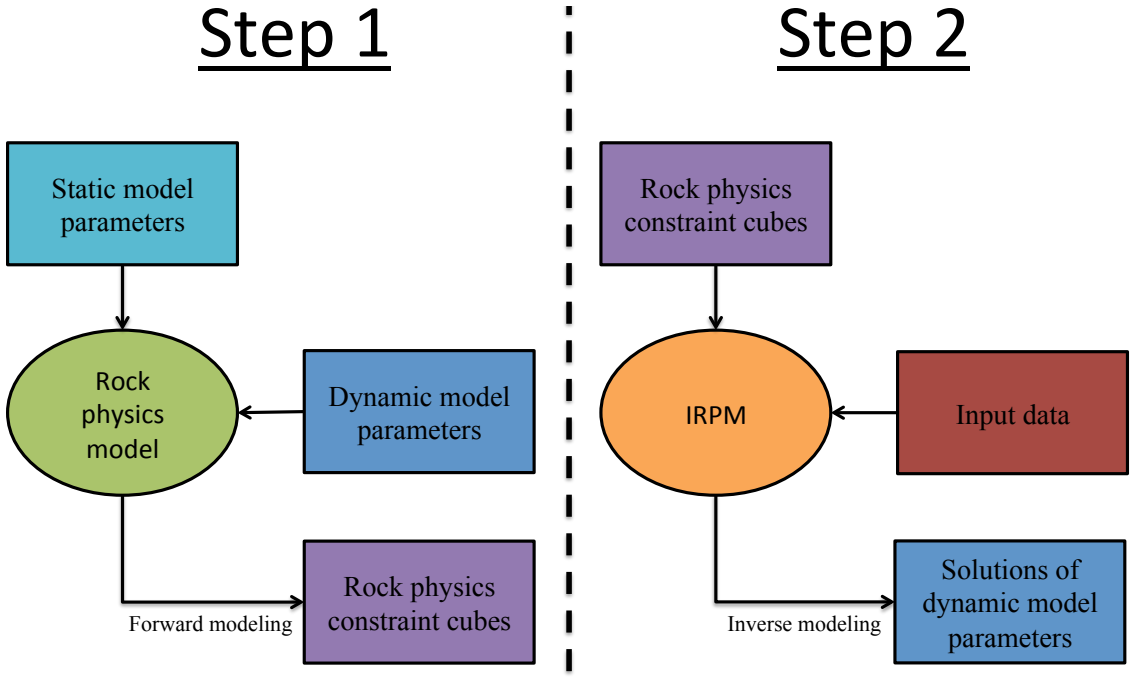

Figure 3.1: A general workflow of the IRPM approach by Johansen et al. (2011).

3.2 Reservoir model

In this study two hypothetical reservoir models are considered; reservoir A and B in figure 3.2. They are composed of the same constituents, but considered to be located at different depths offshore. The solid and fluid constituents are defined in table 3.1. The fluid constituents are different in the the two reservoirs because the temperature, fluid pressure and salinity are unequal (see table 3.2).

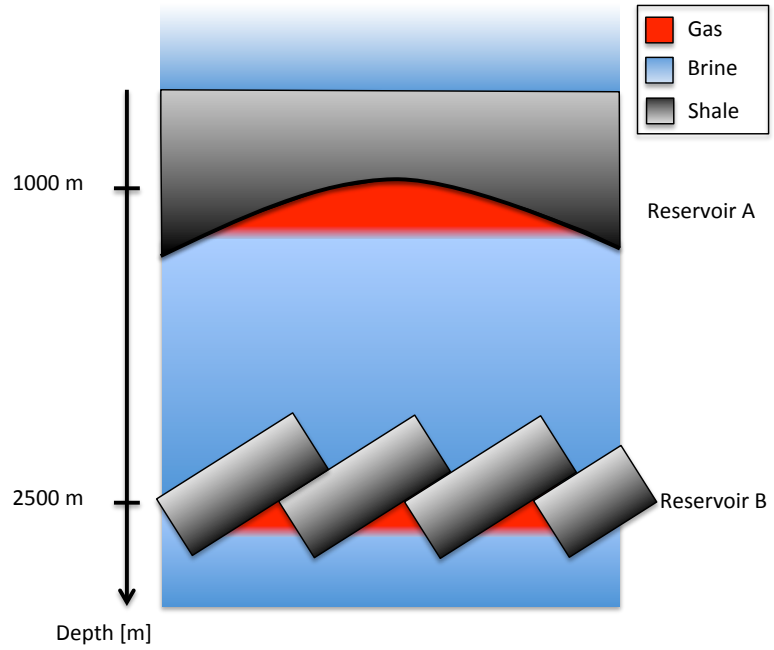

Figure 3.2: The geological scenario assumed for reservoir A and B, with a burial depth of 1000 and 2500 meters, respectively.

Constituent	Bulk moduli [GPa]	Shear moduli [GPa]	Density [g/cm^3]
Quartz	37.9	44.3	2.65
Clay	25	9	2.55
Brine$_{(A)}$	2.6467	–	1.0267
Gas$_{(A)}$	0.0028	–	0.0119
Brine$_{(B)}$	2.7436	–	1.0199
Gas$_{(B)}$	0.008	–	0.0288

Table 3.1: The constituent properties for reservoir A and B. The solid constituents are extracted from Han et al. (1986), while the fluid constituents are found from Batzle and Wang (1992) relations where the input parameters are defined in table 3.2.

Fluid property	Brine$_{(A)}$	Brine$_{(B)}$	Gas$_{(A)}$	Gas$_{(B)}$
Temperature [°C]	50	70	50	70
Fluid pressure [MPa]	10.1	25.2	1.98	4.95
Saltinity [fractions of one]	0.05	0.045	–	–
Gas gravity[1] **[ratio]**	–	–	0.56	0.56

Table 3.2: The fluid properties defined for reservoir A and B used to compute the bulk moduli and density from Batzle and Wang (1992) relations. The fluid components are denoted by (A) and (B) for reservoir A and B, respectively. The temperature is assumed to increase with depth. The fluid pressure is found from using equation (3.3). Salinity often shows a small decrease with increasing temperature. The gas gravity used here represents methane.

As new sediments are deposited, older sediments will be buried. The sediments may differ in a ge-

[1]The gas gravity is the ratio of gas density to air density at 15.6 °C.

ological time perspective that gives sequential sedimentological events reflecting various deposition environments (Boggs, 2006). The lithology may therefore shift significantly with depth, and potential hydrocarbon bearing reservoirs may be present at various depths. Reservoir A is considered to consist of an unconsolidated grain package, while reservoir B has additional cement deposited at the grain surface. This is a very important difference in the choice of suitable rock physics models for the two reservoirs (Avseth et al., 2005). Hence, it seems convenient to apply contact theory (CT) and contact cement theory (CCT) for reservoir A and B, respectively.

The dry rock physics modeling for reservoir A and B is specified as follows;

- For reservoir A, a frictionless Walton (1987) CT model is applied to mimic the elasticity at critical porosity ϕ_0 for smooth grains. A Hashin-Shtrikman-Walpole lower bound (HSW^-) is used to interpolate this end-member with the effective mineral properties. This is referred to as *the friable sand model* in Avseth et al. (2005).

- For reservoir B, a few percent of deposited cement is added in the high porosity regime modeled by CCT (Dvorkin et al., 1991). A Hashin-Shtrikman-Walpole upper bound (HSW^+) is used to model the remaining porosity loss to the effective mineral caused by increased cementation. For simplicity, the cement consists of the same mineral as the grains. Also, the cement is assumed to rim the grains in a coating cement contact manner (the rightmost grains in figure 2.5). This is referred to as the *increasing-cement model* in Avseth et al. (2005).

These hybrid rock physics techniques was reviewed in section 2.4.7. According to Avseth et al. (2005), the elasticity-porosity relationship obtained for reservoir A when choosing a HSW^- trend, describes how the elasticity is changing due to sorting (i.e. mechanical compaction) associated with changing deposition environment. Reservoir B with a HSW^+ describes the influence of increasing cementation (i.e. chemical compaction) that is proportional with depth after cementation initiation. At high porosities, cementation often lead to a relatively small decrease in porosity but a big increase in stiffness, whereas sorting may change the porosity but lightly affects the stiffness (see for instance figure 2.6).

The dynamic model parameters will preferably describe the lithology and reservoir quality. For siliciclastic rocks as in reservoir A and B, the usual parameters to consider are porosity, clay-to-sand fraction (i.e. lithology) and the gas-to-brine (eventually oil instead of gas) portion (i.e. saturation). The remaining model parameters are held constant (i.e. static model parameters) and are following considered. Besides the constituent properties defined in table 3.1, both CT and CCT needs critical porosity ϕ_0 and coordination number C_0 to be specified. Moreover, the effective pressure P_e is needed in Walton's equations (2.33a) and (2.35), whereas the amount of cement expressed by b goes into Dvorkin et al. (1991) equations (2.36a) and (2.36b). These static model parameters have been specified by assumptions and empirical relations as follows.

Firstly, the critical porosity of sediments is assumed to be 40 %; $\phi_0 = 0.4$, which is a typical value for siliciclastic rocks (Nur et al., 1995; Avseth et al., 2005). Following, the coordination number of the deposited sediments can be computed empirically when the critical porosity is known. Here, an interpolation of compiled coordination number data by Murphy (1982) is used (see table 5.1.5 in Mavko et al., 2009). This yield a coordination number

$$C_0(\phi_0)\big|_{\phi_0=40} \approx 8.3 \tag{3.1}$$

for both reservoir A and B.

Proceeding with the pressure parameter, the effective pressure is defined as

$$P_e = P_c - \beta P_p, \tag{3.2}$$

where P_c, P_p and β is the confining pressure, pore pressure and the linear poroelastic coefficient defined as $\beta = 1 - \frac{K_{dry}}{K_s}$, respectively. Here, it is assumed that $\beta = 1$, making the effective pressure P_e equal to differential pressure $P_d = P_c - P_p$. To find the confining pressure the following approach is used;

$$P_c = \rho_s^* g Z, \tag{3.3}$$

where ρ_s^*, g and Z are the bulk density of the overburden, the gravitational constant and depth, respectively (Pluijm and Marshak, 2004). The overburden bulk density of reservoir A is considered to be 1.8 g/cm^3, giving $P_c = 17.7$ MPa. This equation can be modified to yield the pore pressure (i.e. fluid pressure) P_p by replacing ρ_s^* with the respective bulk fluid density ρ_f^*. If the pore fluid in the overburden is brine (see table 3.1 for density) this gives a pore pressure $P_p = 10.1$ MPa and the effective pressure becomes

$$P_e = P_c - P_p = 7.6 \text{ MPa}, \tag{3.4}$$

for reservoir A.

Since the CCT model is pressure independent, pressure computations are skipped for reservoir B. However, CCT require the amount of contact cement expressed by $b = \frac{a}{R}$, where a is the radius of the contact cement layer, and R is the grain radius. If a porosity reduction is only caused by cementation growth, b has the following formula for coating cement contact model;

$$b = \sqrt{\frac{2\,(\phi_0 - \phi)}{3\,(1 - \phi_0)}}, \tag{3.5}$$

for a given porosity ϕ. This cementation distributes the cement evenly around the grain surface and is referred to as *Scheme 2* in Mavko et al. (2009).

A short summary of the static model parameters defined for reservoir A and B are given in table 3.3. Keep in mind that the reservoir parameters defined for reservoir A and B are purely based on assumptions and hypothetical relations. These are highly simplified and can not be directly applied to determine real reservoir parameters.

Model properties			
Reservoir A		Reservoir B	
Theory	CT & HSW$^-$	*Theory*	CCT & HSW$^+$
Depth	1 [km]	*Depth*	2.5 [km]
ϕ_0	40%	ϕ_0	40%
$C_0(\phi_0)$	8.3	$C_0(\phi_0)$	8.3
P_e	7.6 [MPa]		
Friction	None	*Cement*	Coating

Table 3.3: The rock physics models, depth and static model parameters defined for reservoir A and B.

3.3 Forward rock physics modeling constraint cubes

The mission of a rock physics model is to appropriately relate the model parameters to the corresponding data parameters. In general, the rock physics models can be thought of as functions of M model parameters;

$$d = R(\underbrace{\phi, C, S_g}_{\text{Dynamic}}, \underbrace{K_s, \mu_s, K_f, C_0, P_e, \ldots, M}_{\text{Static}}), \tag{3.6}$$

where d is a specific data parameter and R is a chosen rock physics model (for instance one of those reviewed in section 2.4.3 - 2.4.7). The input model parameters are composed of a set dynamic model parameters that varies, preferable porosity ϕ, lithology C and saturation S_g, and a set static model parameters that are constant, e.g. solid bulk moduli K_s, solid shear moduli μ_s, fluid bulk moduli K_f, coordination number C_0 and effective pressure P_e. One may generalize (3.6) by using vector notation to include a set of data parameters $\vec{d} = [d_1, d_2, \ldots, d_N]$ and model parameters $\vec{m} = [m_1, m_2, \ldots, m_M]$;

$$\vec{d} = \vec{R}_k(\vec{m}), \tag{3.7}$$

where index k specify a certain rock physics model which on this formalism is

$$\vec{R}_k = [R_{k1}(\vec{m}), R_{k2}(\vec{m}), \ldots, R_{kN}(\vec{m})],$$

where every component $R_{ki}(\vec{m})$ can be viewed as a rock physics expression procuring the data parameter d_i from $\vec{m}$.
Ê

In reservoir characterization the data parameters are acquired in sought of determining model parameters. Thus, it demands an inverse rock physics model so (3.7) becomes

$$\vec{m} = \vec{R}_k^{-1}(\vec{d}). \tag{3.8}$$

Nevertheless, the usual case scenario is that $M > N$, which implies that the forward rock physics model $\vec{R}_k$ is a nonlinear transformation where $\vec{d}$ is an image of $\vec{m}$. In practice, such inverse rock physics functions $\vec{R}_k^{-1}$ are inexistent, as this is an ill posed problem with non-unique solutions (Johansen et al., 2011).

Instead, we can consider resampling a set of forward rock physics constraints. They are in turn applied on observational data constraining the dynamic model parameters. The rock physics constraints are built for each data parameter d_i by perturbing over a set of specified dynamic model parameters $m_j (j = 1, \ldots, M_D)$, where the result will be a constraint cube with $L_1 \times L_2 \times \ldots \times L_{M_D}$ equidistant computational points of dimension M_D. The dynamic model parameters considered in the following examples are porosity ϕ, lithology C and gas saturation S_g (denoted the PLF domain), i.e. $j = \phi, C, S_g$, which will correspond to x-, y-, z-axis in a cartesian coordinate system. Each of these dynamic model parameters can however switch place with one of the static parameters, depending on the purpose of the study. Furthermore, after defining the maximum $m_{j,max}$ and minimum $m_{j,min}$ values for a specified dynamic model parameter j, the l-th value equals $m_{jl} = m_{j,min} + (l-1)\Delta m_j$ with an increment $\Delta m_j = \frac{(m_{j,max} - m_{j,min})}{L_{m_j} - 1}$, where L_{m_j} is the number of values ($L_{m_j} = 26$ in this study). The m_{jl} values are next sequentially fed into the rock physics model to compute the effective elastic properties for a given data parameter d_i. This creates a discrete sampled constraint cube for each data parameter (e.g. figure 3.3 shows bulk moduli K for reservoir B).

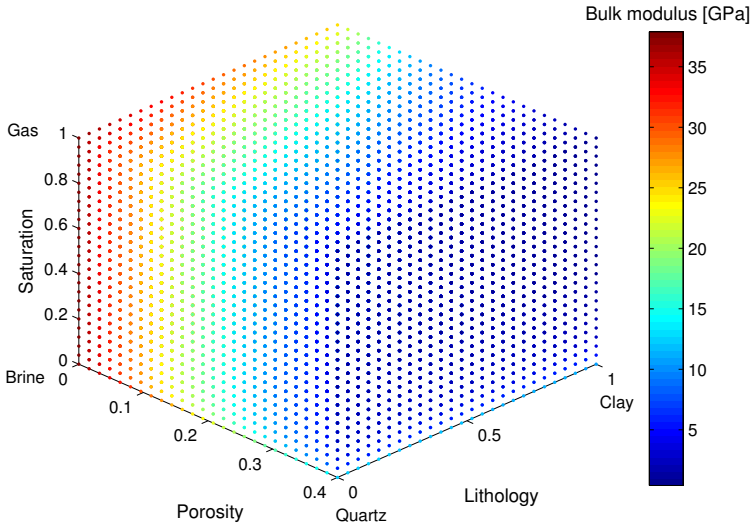

Figure 3.3: The bulk moduli discrete constraint cube for reservoir B. The cube is divided into a grid containing $26 \times 26 \times 26 = 17576$ equidistant points within an interval of $0 < \phi < 0.4$, $0 < C < 1$ and $0 < S_g < 1$. The color gradient corresponds to the computed bulk moduli K.

Interpolation of the estimated points gives a smooth continuous scalar field D_i as

$$D_i(\phi, C, S_g) = d_i, \quad \forall \quad \phi \in [\phi_{min}, \phi_{max}] \wedge C \in [C_{min}, C_{max}] \wedge S_g \in [S_{g_{min}}, S_{g_{max}}],$$

for data parameter i. The constraint cubes for bulk moduli K, shear moduli μ and density ρ (i.e. $i = K$, μ, and ρ) are shown in figures 3.4 and 3.5 for reservoir B.

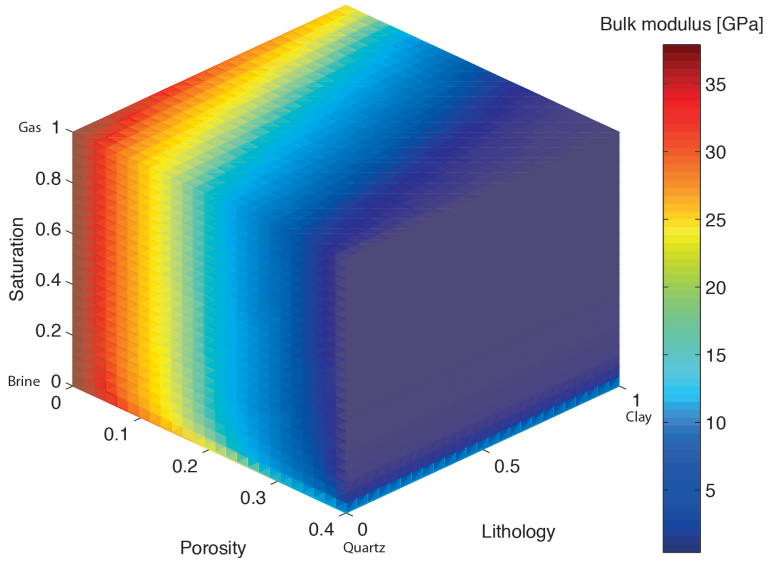

Figure 3.4: Interpolation of points in figure 3.3 introduce a continous bulk moduli K constraint cube $D_K(\phi, C, S_g)$.

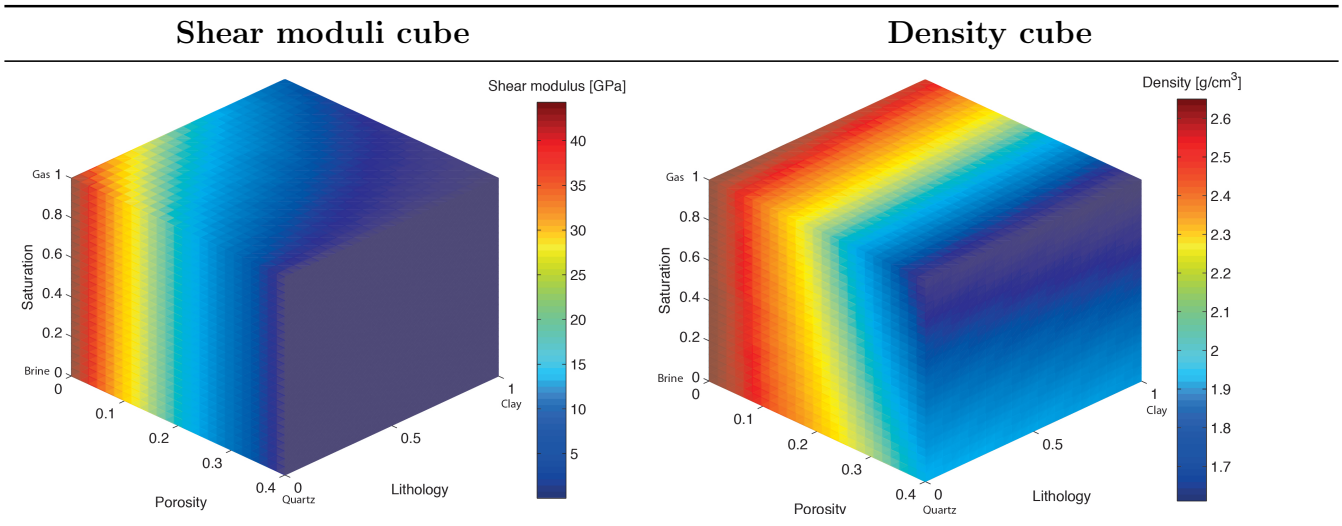

Figure 3.5: Shear moduli and density constraint cubes for reservoir B.

The dynamic model parameters, porosity, lithology and saturation, are specifically perturbed within the following rock physics relationships. For various solid volume fractions of quartz and clay (i.e. the lithology), the effective mineral properties K_s and μ_s are found from Hill's equation (2.20). For various fluid volume fractions of brine and gas (i.e. the saturation), the effective fluid bulk moduli K_f is found from Wood's equation (2.39), and the fluid substitution is introduced by using the Gassmann model, equation (2.38). The porosity is explicitly given in the Hashin-Shtrikman-Walpole bounds and

the Gassmann model, which represents the fluid volume fraction.

The density cube is not calculated using a rock physics model as for the bulk and shear moduli. Instead, for a given lithology, saturation and porosity, the density function $\rho(\phi, C, S_g)$ is the weighted sum of the average constituent densities;

$$\rho(\phi, C, S_g) = \phi\left[S_g\rho_{gas} + (1 - S_g)\rho_{brine}\right] + (1 - \phi)\left[C\rho_{clay} + (1 - C)\rho_{quartz}\right], \tag{3.9}$$

where ρ_{brine}, ρ_{gas}, ρ_{clay} and ρ_{quartz} are the densities of brine, gas, clay and quartz, respectively. Hence, the density constraint cubes for reservoir A and B are equivalent. This simple linear expression contains only density constants of the various constituents and the dynamic model parameters (ϕ, C, S_g). Thus, it is relevant to interpret the concurrency between an alteration of a specified dynamic model parameter and the corresponding impact on the density cube. For instance, the porosity ϕ appears in both terms in (3.9) and should subsequently affect the density ρ more than lithology C or saturation S_g. This is confirmed by the density cube (figure 3.5) as one observe that the color gradient is shifting more along the porosity axis than in direction of lithology or saturation axis. Also, a big contrast in density between solid and fluid constituents is represented by porosity, whereas the contrast in density of different lithology and saturation are much smaller. This interpretation reveals the connection between the visual constraint cube and the underlying mathematical expression from the density function, and equivalently the rock physics models.

Any given set of PLF (ϕ, C, S_g) will be equivalent to one specific data parameter value $\hat{d}_i$, while a single $\hat{d}_i$ value corresponds to several sets of PLF values constrained by a surface, referred to as isosurface. In figure 3.6 the reservoir A bulk and shear constraint cubes are shown, where figure 3.7 shows two isosurfaces obtained for bulk moduli values $K_1 = 3$ GPa and $K_2 = 25$ GPa, corresponding the bulk moduli constraint cube in figure 3.6. Notice that the elastic constraint cubes for reservoir A deviates significantly from the corresponding constraint cubes for reservoir B.

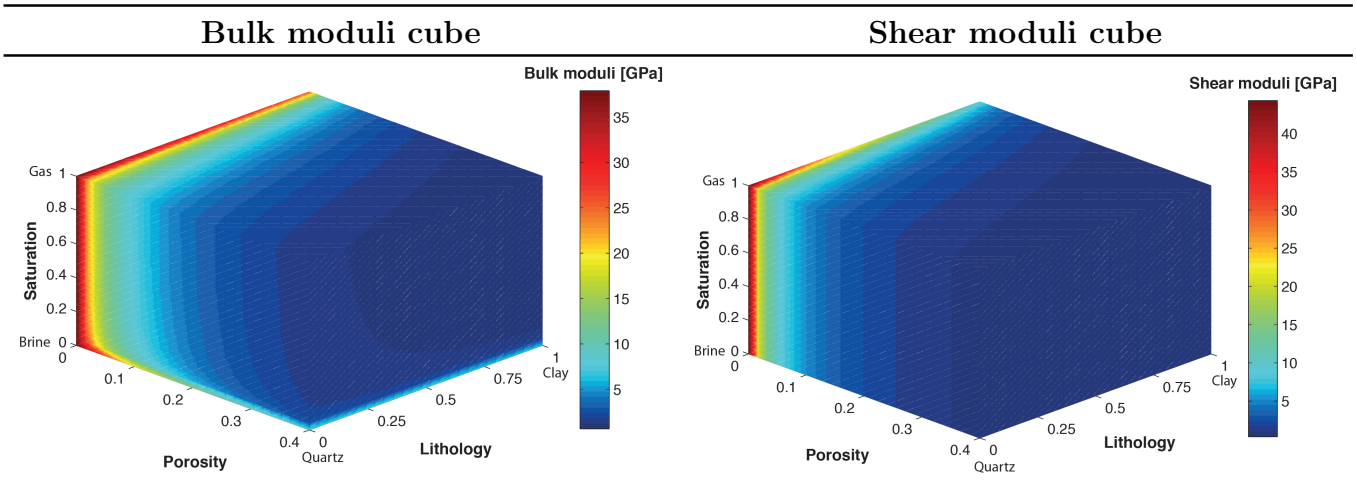

Figure 3.6: Bulk and shear moduli constraint cubes for reservoir A.

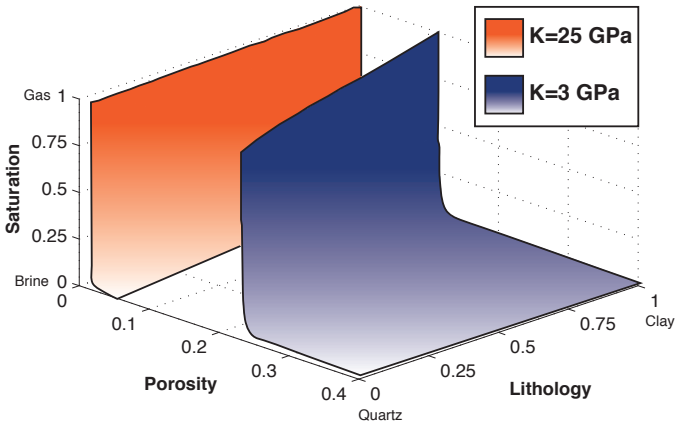

Figure 3.7: Two bulk moduli isosurfaces obtained from the bulk moduli constraint cube for reservoir A.

3.4 A 2D resampling of rock physics constraints

The original idea that elaborated to the IRPM approach by Johansen et al. (2011) is based on a paper by Johansen et al. (2004). This paper considers creating 2D rock physics constraints that are reformulated into other relationships. In the calculation of the constraint cubes presented in the previous section, all three PLF parameters varied. If one of these are held constant, the data parameters d_i can be viewed as contour lines in a 2D plot. A resampling procedure is subsequently used to extract the relationship between the two model parameters that varies. This demonstrates how rock physics constraints are generated from a different point of view than seen in the previous section.

Lets demonstrate by use a constant saturation $S_g = 1$ (pure gas) and $S_g = 0$ (pure brine), and let porosity $\phi \in [0, 0.4]$ and clay content $C \in [0, 1]$ vary as in the previous examples. Once again, the reservoir B model has been used to demonstrate the resampling procedure of Johansen et al. (2004) that goes as follows. A resampling of the rock physics constraints is done for a fixed set of data parameters $d_i (i = 1, \ldots, N)$ with j-th value equal to $D_{ij} = d_{i,min} + (j-1)\Delta d_i$ with an increment $\Delta d_i = \frac{(d_{i,max} - d_{i,min})}{L_{d_i} - 1}$, where L_{d_j} denotes number of values. For every D_{ij} that intercepts the contour lines, a registration of the clay content for a certain porosity gives the $\phi - C$ dependency. The resample procedure is demonstrated in figure 3.8 and considers bulk moduli K with $L_K = 6$, $K_{max} = 34.84$ GPa and $K_{min} = 15$ GPa, extracting six $\phi - C$ contour relations for both pure brine and gas. Each of these $\phi - C$ contours can be described as direct functions $\varphi_{D_{ij}}(\vec{m})$ (named correlation functions) of the dynamic model parameters $\vec{m}$ for a given data parameter value $D_{ij} \in [d_{i,min}, d_{i,max}]$. In 3D, the correlation functions corresponding to the data parameter values $D_{ij} (i = K)$ in figure 3.8 are shown in figure 3.9 as isosurfaces. Here, 26 various saturation values are perturbed and resampled, including pure brine and gas in figure 3.8, extracting 26 porosity-lithology contours that are subsequently interpolated. Notice the concurrency between the parallel isosurfaces and the corresponding contour lines for pure gas in figure 3.8 d).

Considering any isosurface in figure 3.9, a combination of ϕ, C and S_g corresponds a point and may

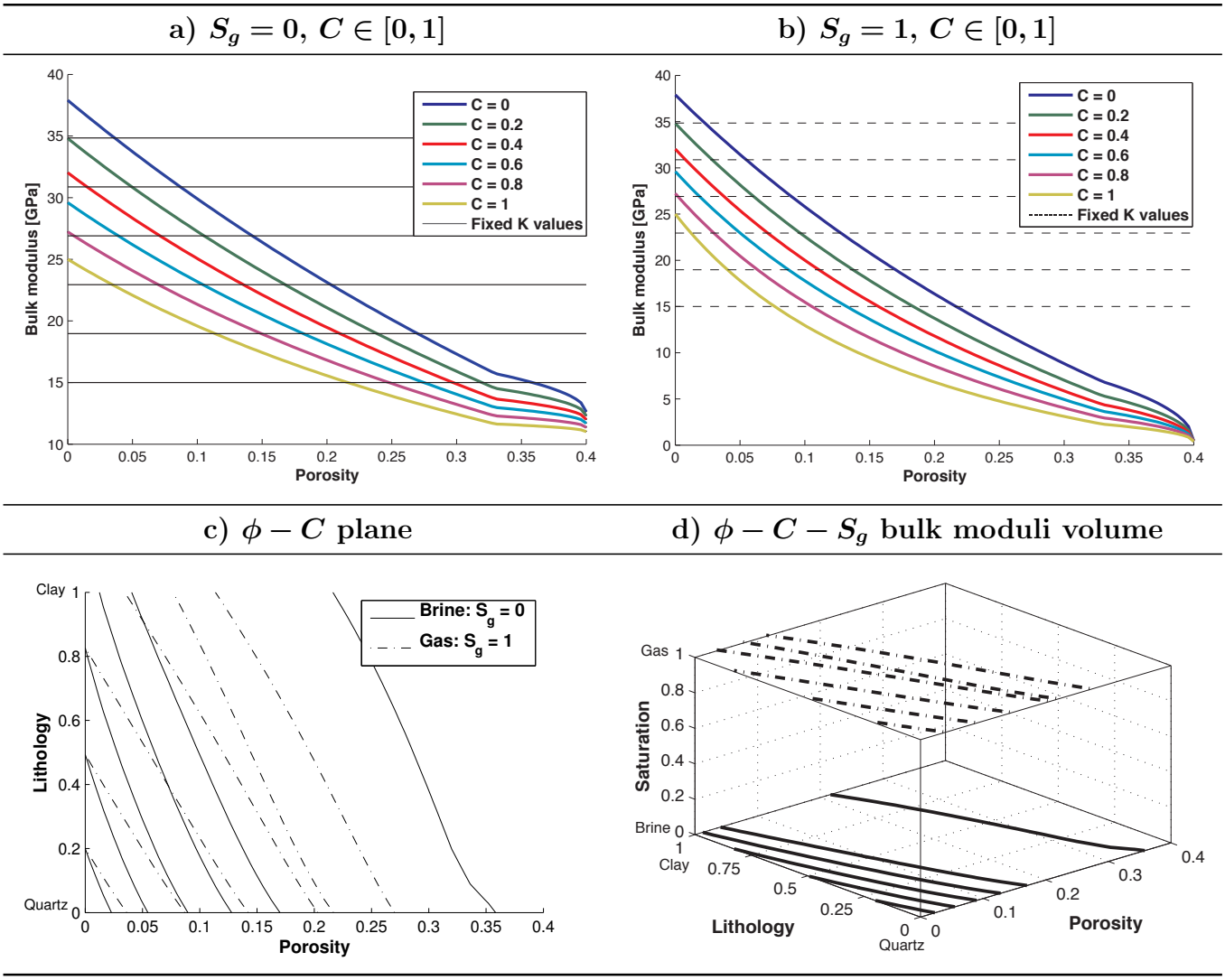

Figure 3.8: The resampling procedure for reservoir B in the two upper plots shows bulk moduli K as function of porosity and lithology sampled at six distinct K values for pure brine and gas saturations. In the two lower plots, the corresponding sampling are plotted in the porosity-lithology plane, represented in a 2D and 3D point of view.

be a possible solution to the particular data parameter value. Also notice the significant difference in bulk moduli sensitivity due to a change in porosity compared to a change in lithology or saturation. The bulk moduli decreases significantly when increasing porosity, while the bulk moduli is much less sensitive to the other two model parameters. Notice however the strong influence on the effective stiffness when introducing a small amount of gas in a fully brine saturated rock.

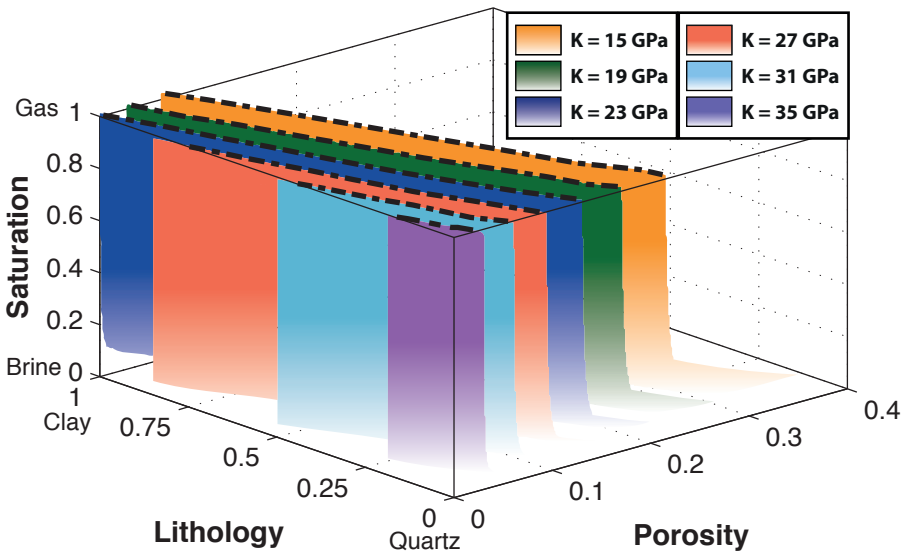

Figure 3.9: The six isosurfaces corresponding to the six resampled K values in figure 3.8. The word iso comes from the Greek word *isos*, meaning equal. In this sentence, each individual surface contains the same data parameter value at every point.

3.5 The IRPM algorithm

The six isosurfaces in figure 3.9 represent the same data parameter but have various data parameter values $\hat{d}_i$ $(i = K)$. Each isosurface may further be denoted as $\varphi_{\hat{d}_i}(\vec{m})$ and they tend to be more or less parallel to each other. This could already be seen by studying the color gradient in the bulk moduli constraint cube (figure 3.4) for reservoir B. Focusing on a single isosurface, it spans all possible PLF combinations for a particular input data value $\hat{d}_i$. It is clearly not constraining much the PLF parameters, which is quite typical. This is also as expected as determining the parameters from one input data yields an undetermined problem. However, by applying a new input data d_j with value $\hat{d}_j$, an additional isosurface is exhibited in the PLF space. The two isosurfaces tend to intercept and create a line that constrains the solutions to the problem accordingly as

$$\varphi_{\hat{d}_i} - \varphi_{\hat{d}_j} = 0, \tag{3.10}$$

narrowing the solution range significantly from considering only one input data. In figure 3.10 this has been done with the bulk and shear moduli for some values $\hat{d}_K$ and $\hat{d}_\mu$ for reservoir B. The projection (black dashed lines for porosity) of the intersection line (purple line) onto the PLF axis corresponds the solution ranges (red intervals).

A third input parameter d_n with value $\hat{d}_n$ constrains the solutions even further to the intersection of all three respective isosurfaces. The solution to this problem is accordingly

$$\varphi_{\hat{d}_i} - \varphi_{\hat{d}_j} - \varphi_{\hat{d}_n} = 0, \tag{3.11}$$

which corresponds to one or several points.

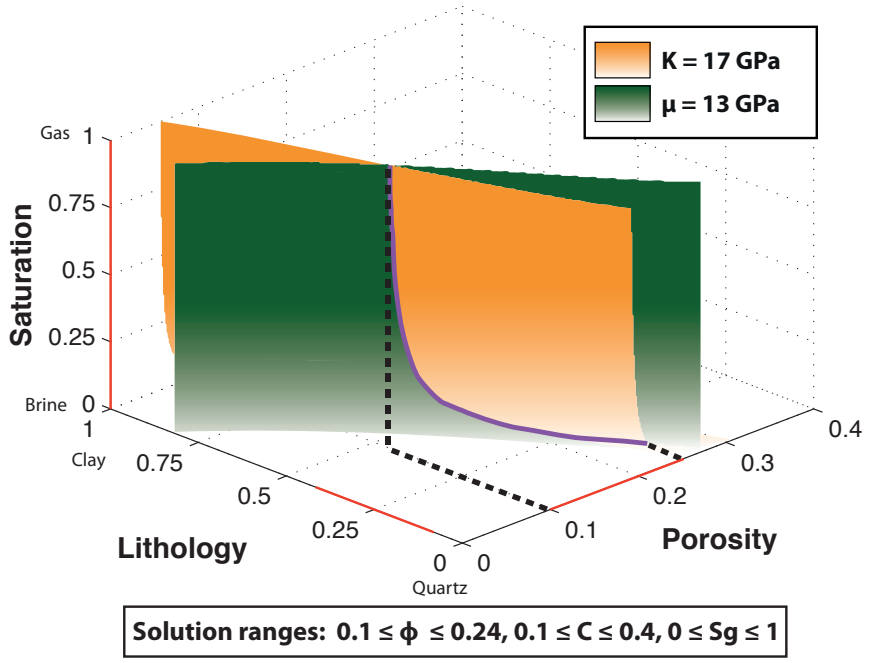

Figure 3.10: Intersection of the isosurfaces $\varphi_{K=17}(\vec{m})$ and $\varphi_{\mu=13}(\vec{m})$.

In figure 3.11 the density isosurface d_ρ is the third one present. Thus, a realsitic chance of obtaining a unique solution (i.e. a determined problem) for the dynamic model parameters is first possible when the number of dynamic model parameters $m_j (j = 1, \ldots, M)$ equals the number of data parameters $d_i (i = 1, \ldots, N)$, i.e. $M = N$. However, because of the non-linearity of rock physics models, several solutions may occur even when $M = N$. Furthermore, it is typical to perturb over static model parameters that are influenced by uncertainty as well as considering several possible rock physics models as valid candidates. Hence, one can not really talk about one unique solution when doing inverse rock physics modeling.

The actual sought of solutions is in practice done by mathematical approximation algorithms carried out by computer implementation. In the plots above, a Newton-Raphson based method (Kelley, 2003) is used, that is a calculus method for locating roots, or in this case interceptions of functions. Alternatively, a proximity detection method can be used that allow several points on the isosurfaces that lies within a certain spatial distance to each other to be considered as valid solutions. For more details about these solvers, the reader is referred to appendix B.

From a geometric point of view, isosurfaces that represents various data parameters and are parallel makes it cumbersome to obtain stable solutions. A small perturbation in one of the data parameter values would result in a significant displacement of the intersection line or points. To prevent this, the isosurfaces should be arranged more perpendicular to each other, i.e. the dot product of their normal vectors at the intersection, should be close to zero. With respect to this, Jensen and Johansen (2011)

propose a strategy for finding the best combination of data parameters to achieve as stable and with as narrow solutions as possible.

The IRPM approach can be summarized as a two-step procedure:

1. **Model forward constraint cubes:** define static and dynamic model parameters for the reservoir. Choose an appropriate rock physics model for the reservoir, and use it to do a forward modeling for a discrete set of combination of dynamic model parameters.

2. **Use IRPM to find inverse solutions:** select constraint cubes of various data parameters that yields isosurfaces for a set of input data. The IRPM algorithm is further used for localizing intersections between the respective isosurfaces. The coordinate of intersection points yields the inverse solutions of each dynamic model parameter corresponding to the input data. These solutions may aid in reservoir characterization.

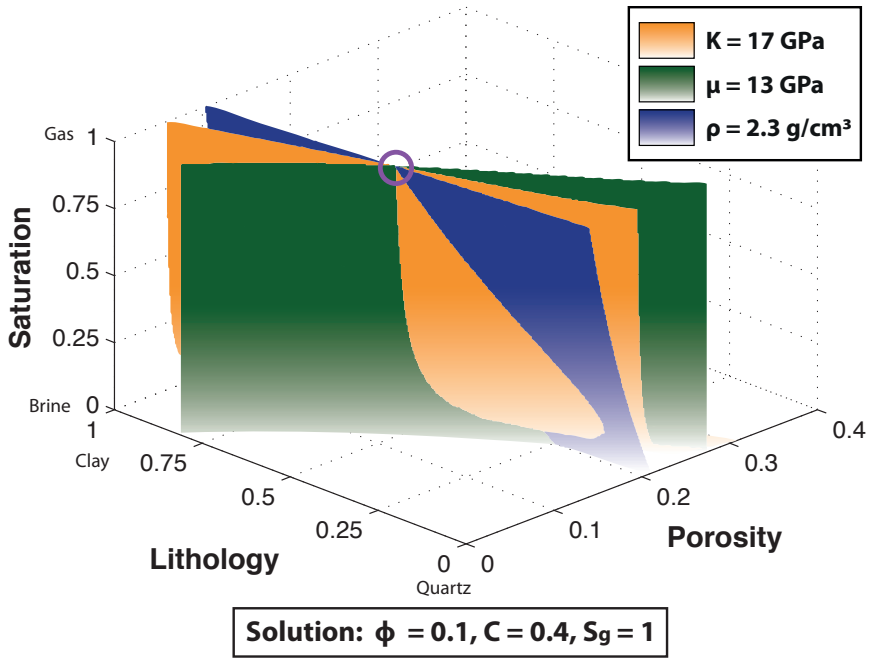

Figure 3.11: Intersection of the isosurfaces $\varphi_{K=17}(\vec{m})$, $\varphi_{\mu=13}(\vec{m})$ and $\varphi_{\rho=2.3}(\vec{m})$. In this plot, a single solution appears in the purple circle. However, this solution must not be considered to represent the true solution as this problem is non-unique.

3.6 Summary

In this chapter we have seen a general workflow of the IRPM approach and applied it on two distinct reservoir models. The reservoir models have been used to demonstrate how to model rock physics constraints and how to obtain solutions of dynamic model parameters by applying IRPM. We have seen

examples that supports that the inverse problem is emphasized by non-unique solutions. However, if an appropriate rock physics model is chosen, ideal input data acquired and the static model parameters defined sufficiently accurate, interpretation of the solutions can be helpful in reservoir characterization.

Chapter 4

IRPM performance and influence of reservoir parameter uncertainties

4.1 Outline

Is inverse rock physics modeling (IRPM) a robust, reliable and convenient method applicable for reservoir characterization? To evaluate this, the IRPM algorithm is put to the test on synthetic data constructed by the same rock physics model as the rock physics constraint cubes, obtaining fully consistent input data. Next, the influence on inverse solutions from uncertainties in the pre defined static model parameters is studied.

4.2 IRPM performance on synthetic input data

Say that the porosity, lithology and saturation (PLF) properties were known at 27 discrete points in reservoir B (see figure 4.1). These dynamic model parameter values are subsequently substituted into the rock physics model and density function applied for reservoir B (see section 3.2, 3.3 and 3.4) to compute the elastic moduli and density, respectively (see figure 4.2). Now, both the dynamic model and data parameters are known in advance, and it is possible to check if IRPM will succeed to identify the correct model parameters values when the corresponding input data is 100 % consistent.

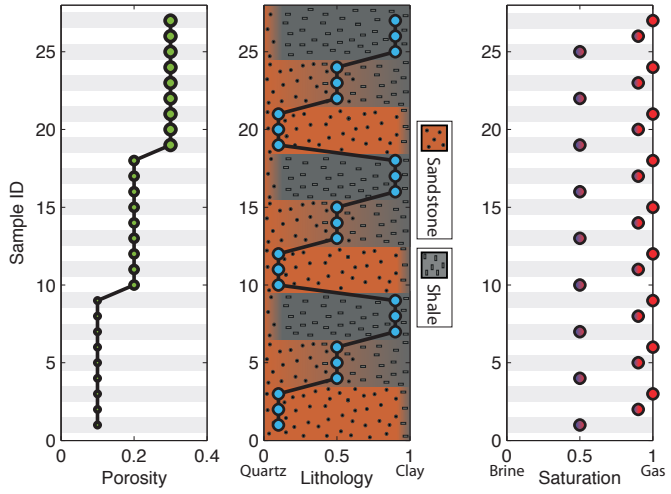

Figure 4.1: 27 discrete combinations of porosity ϕ, lithology C and saturation S_g. The zebra stripes on background separates the various data samples.

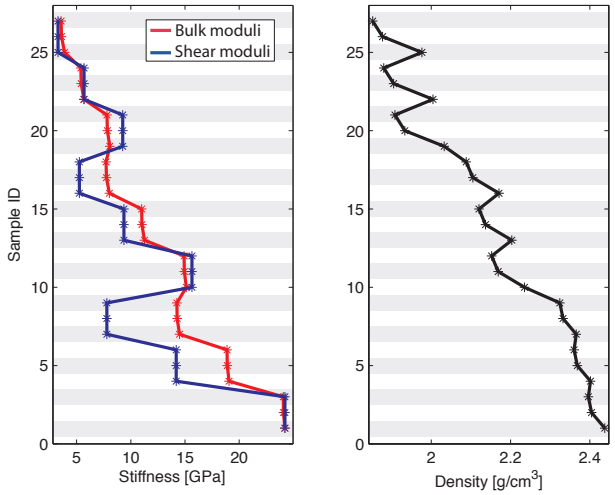

Figure 4.2: The corresponding synthetic data parameters computed using the rock physics model for reservoir B.

Figures 4.3-4.6 shows the inverse solutions obtained from applying combinations of the bulk moduli K, shear moduli μ and density ρ in each sample seen in figure 4.2. The pre defined dynamic model parameters in figure 4.1 are marked as black squares superimposing the colorized inverse solutions. Various combinations of two input data (i.e. undetermined problem) is presented in figure 4.3) K and μ, 4.4) K and ρ and 4.5) μ and ρ, whereas figure 4.6 shows all three input data (i.e. determined problem) K, μ and ρ. A Newton-Raphson based solver (see appendix B.1) are used here. The solutions obtained for sample #5 for the undetermined and "determined" problem in figures 4.5 and 4.6, respectively, can be studied in figures 4.7 and 4.8, respectively. We see that for all combinations of two input data that the

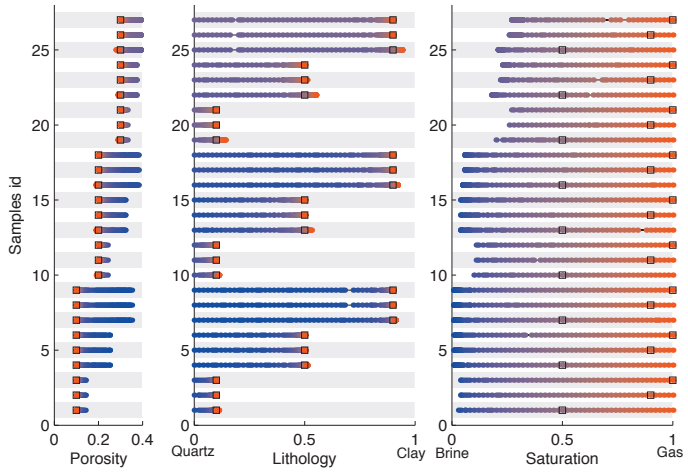

Figure 4.3: Inverse solutions using K and μ.

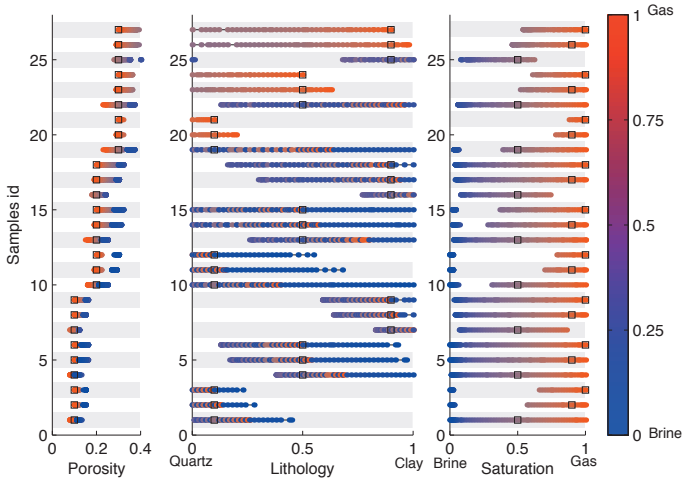

Figure 4.4: Inverse solutions using K and ρ.

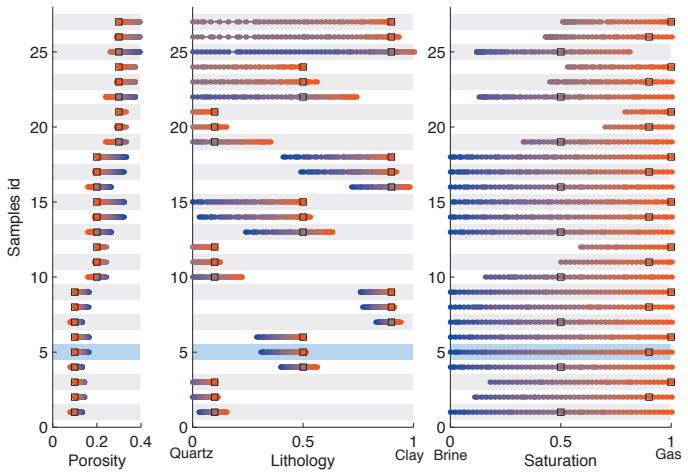

Figure 4.5: Inverse solutions using μ and ρ.

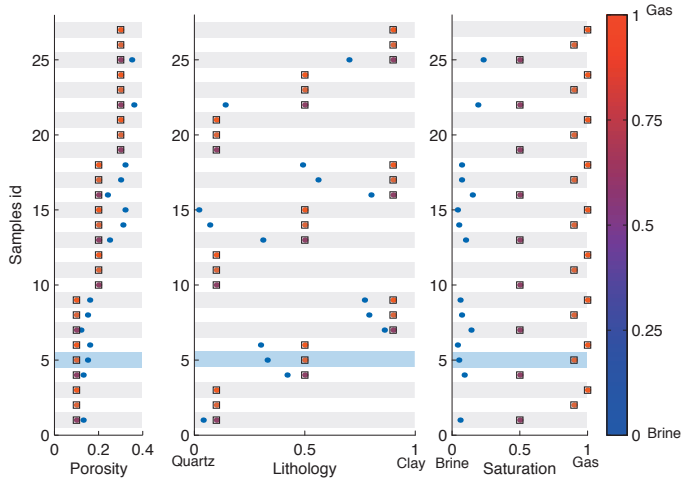

Figure 4.6: Inverse solutions using K, μ and ρ.

Figure 4.3-4.6: Inverse solutions obtained from various combinations of the input data samples in figure 4.2. The colors of the solutions denotes the saturation as proposed by the colorbar. Undetermined problems are presented by a combination of two input data (figures 4.3-4.5), whereas a determined problem is faced when considering three input data (figure 4.6). In figures 4.5 and 4.6, sample #5 is denoted by a bluish background as it is used in figure 4.7 and 4.8 to study the solutions.

porosity is constrained quite well, whereas a less narrow solution range is achieved for lithology and saturation. Often the dynamic model parameters are practically not constrained at all. An example of unconstrained saturation solutions can be seen in figure 4.7. Note that the solution ranges marked with orange on each axis are the same as those for sample #5 in figure 4.5.

The majority of samples in figure 4.6 when applying three input data have a second solution unequal the true solution. See for instance sample #5 in figure 4.8 where all three isosurfaces intersects in a point at two different locations and yields two different solutions. However, it may be possible to discard invalid solutions if additional information (e.g. from well data) is available. For instance, information about what type of fluid that is most likely to be present in the reservoir can be helpful.

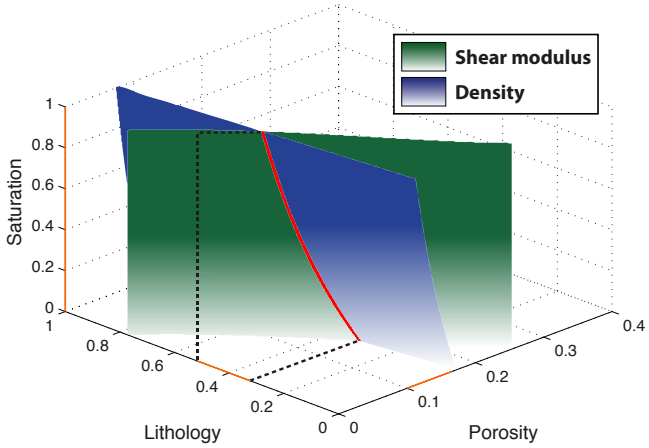

Figure 4.7: Isosurfaces for μ and ρ corresponding sample #5 in figure 4.5. The red intersection line is projected (black dashed lines for lithology) onto the PLF axis as orange intervals.

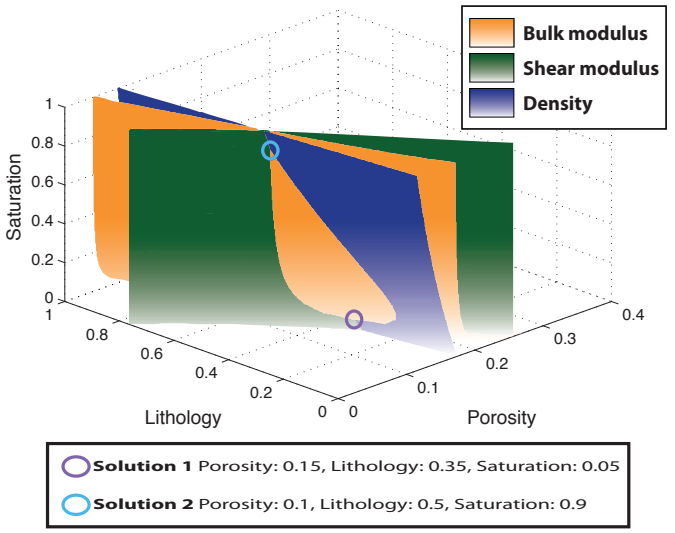

Figure 4.8: Isosurfaces for K, μ and ρ corresponding sample #5 in figure 4.6.

The pre defined saturations in figure 4.1 contains only values ≥ 0.5. Hence, limiting solutions to $S_g \in [0.5, 1]$ results in solutions which are consistent with the synthetic model (see figure 4.9).

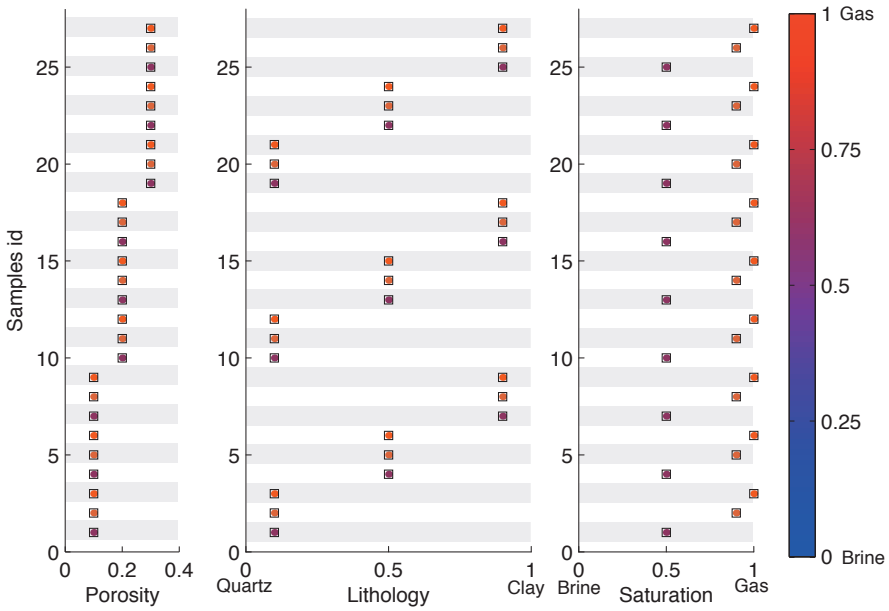

Figure 4.9: The same solutions as in figure 4.6, but here solutions with saturations under 50 % gas content are discarded. Hence, all the solutions obtained by the IRPM algorithm matches the pre-defined dynamic model parameters in figure 4.1.

4.3 Reservoir parameter uncertainties and influence of fluid heterogeneity

The synthetic input data generated in figure 4.2 were 100 % consistent with the rock physics constraint cubes used in the IRPM algorithm for reservoir B. Such settings are however not realistic; the rock physics constraints and observational input data will usually suffer from a certain degree of inconsistency. It may be that the input data lack precision from measurements, but it may also be that the rock physics constraints are too inaccurate. Uncertainties regarding defining static model parameters is one issue that could counteract accuracy in the rock physics constrains. In section 3.2 reservoir A and B were defined with a critical porosity $\phi_0 = 0.4$, which is a typical value for sandstones and limestones (Nur et al., 1995; Avseth et al., 2005). The coordination number C_0 was following estimated as a function of the critical porosity (see figure 4.10).

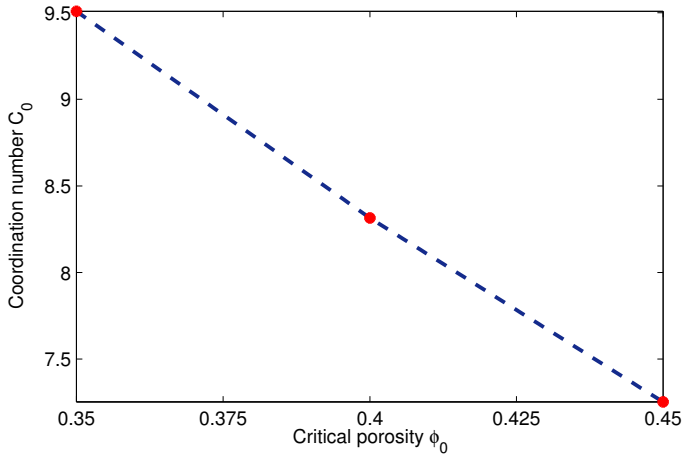

Figure 4.10: Critical porosity ϕ_0 and coordination number C_0 relationship according to Murphy (1982) compiled data (red points). The dashed blue line interpolates the data points.

If the actual critical porosity deviates significantly from that defined in the rock physics constraints, this will in turn influence the coordination number, and the rock physics constraints may become significantly imprecise. To investigate the influence of a perturbation in critical porosity (and following the coordination number), a set of five constraint cubes for reservoir B were generated with various critical porosities between 35 % and 45 % at steps $\Delta\phi_0 = 2.5$ %. Pre defined model parameter combinations and corresponding synthetic input data used in the IRPM approach is shown in figure 4.1 and 4.2, respectively. In figure 4.11 the inverse solutions of the five different critical porosity constraints are shown, using bulk moduli, shear moduli and density in the IRPM approach. As the input data in figure 4.2 were calculated using a critical porosity of 40 %, the green solutions (corresponding constraints with $\phi_0 = 0.4$) matches the black squares (i.e. the black squares) perfectly. Also notice that several samples have a second solution of the same critical porosity ϕ_0 model, corresponding to that previously seen in figure 4.6. We further see that various dynamic model parameter solutions depends differently on critical porosity; the porosity is lightly, lithology some and the saturation strongly

depends on critical porosity. The solutions also deviates more from the true model with increasing difference between the ϕ_0 defined in the various constraint cubes and the input data calculated with $\phi_0 = 0.4$. If a particular solution from a ϕ_0 model in a given sample is not found, it may be that it is overlapped by another solution (i.e. the solutions of various ϕ_0 models are equal), as seen in several samples for porosity solutions.

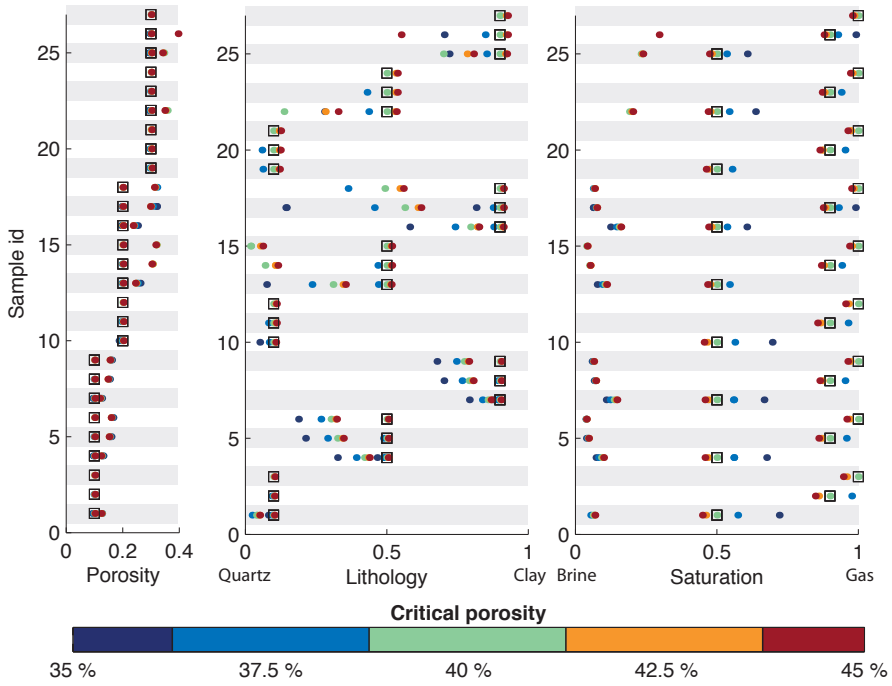

Figure 4.11: The inverse solutions obtained by applying five constraint cubes of varying $C_0(\phi_0)$. The color of the solutions reflects the critical porosity proposed by the colorbar. The black squares marks $\phi_0 = 0.4$ as defined for reservoir B in section 3.2 and were used in calculating the applied input data (see figure 4.2).

Another example of a static model parameter that may be characterized by unpredictability is the b parameter that describes location of cement deposited somewhere on the grain surface in reservoir rocks. Figure 2.5 represents some standard cement models; coated models describes cement evenly deposited on the grain surface, whereas contact models considers all cement accumulated at the grain contact points. The rock physics modeling for reservoir B (see section 3.2, 3.3 and 3.4) requires the parameter $b = a/R$, where a and R respectively is the radius of the contact cement and the grain radius, to specify the amount of contact cement. However, by assuming that porosity reduction in sands is due to cementation only and by adopting certain cement deposition models, the parameter b can be expressed explicitly as in equation (3.5) when considering a coated cement model (Mavko et al., 2009). If it turns out however that a contact cement model would be more appropriate for reservoir B, the parameter b will have the following expression

$$b = 2\left[\frac{\phi_0 - \phi}{3C_0\,(1-\phi_0)}\right]^{\frac{1}{4}}, \tag{4.1}$$

that describes all cement to be located the grain contact points and subsequently yields a stiffer rock.

To study how various cement models may influence inverse solutions obtained by IRPM, constraint cubes with accordance to equation (4.1) were generated. The inverse solutions is shown in figure 4.12 for both coated and contact cement models. The synthetic input data applied is shown in figure 4.2 and is calculated by using a coated cement model represented by the black squares as true solutions. Solutions obtained by applying constraints with a coated cement model has at least one consistent solution for every sample, whereas a contact cement model yields no solutions that are fully consistent.

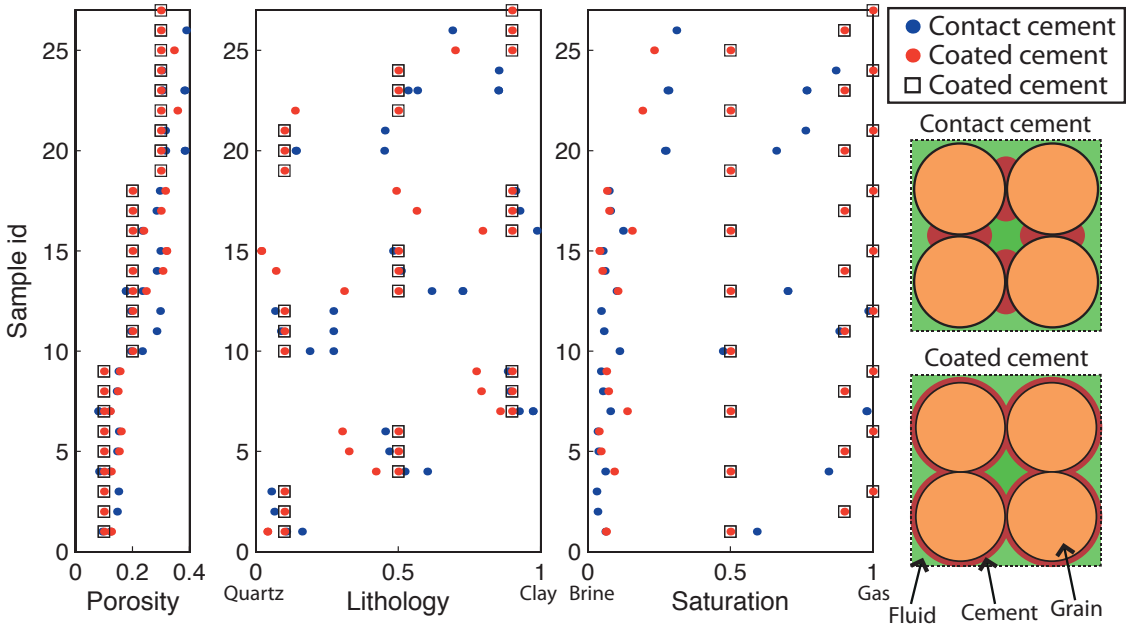

Figure 4.12: The inverse solutions obtained by applying two set of constraint cubes for reservoir B with different cement models. The black squares represents the true solutions consistent with the applied synthetic input data.

Apart from structural heterogeneity like critical porosity and cement location, nonuniform distribution of fluids introduce fluid heterogeneity that also affect the overall elastic behavior of a porous rock. Hill's equation (2.20) were proposed in section 2.5 to estimate the bulk moduli of patchy fluid saturation by equation (2.40). However, if there exists uncertainties about which fluid mix model to choose, the following example investigates the impact on the inverse solutions. The rock physics constraint cubes for reservoir B considered the Wood's formula (2.39) to predict the bulk moduli of the pore fluids. New constraint cubes for reservoir B with a Hill fluid model were generated and applied together with the synthetic input data (see figure 4.2) in the IRPM algorithm. The corresponding inverse solutions were identified only at the samples where a gas fraction S_g of 1 were defined, whereas no solutions were found for the remaining samples. In figure 4.13 the pre defined saturation of each sample is shown next to the effective bulk moduli of the rock when applying both a Wood and Hill fluid model. Also, the solutions for sample #22 is shown in the PLF space. Notice how the effective bulk moduli of the rock is the same for both applications of Wood and Hill fluid models when considering a fully gas saturated rock. This is logical as both fluid models will predict the same properties when considering pure gas or brine saturations, i.e. $K_f^{(\text{Wood})} = K_f^{(\text{Hill})}$ if $S_g = 1$ or $S_g = 0$. The remaining samples deviates in effective bulk moduli as the fluid models predicts different properties, as seen in the bulk

moduli isosurfaces in the PLF space. We see that the orange bulk moduli isosurface (i.e. a Wood fluid model) yields a solution where it intersects the shear moduli and density isosurfaces. However, no such solution is found when using a Hill model due to a significant displacement of the purple bulk moduli isosurface that provides no interception with shear moduli and density isosurfaces at a distinct point. Any fluid patchiness can be introduced by creating a set of constraint cubes, and they will yield bulk moduli insosurfaces that are located in between the orange and purple isosurface in figure 4.13 for reservoir B.

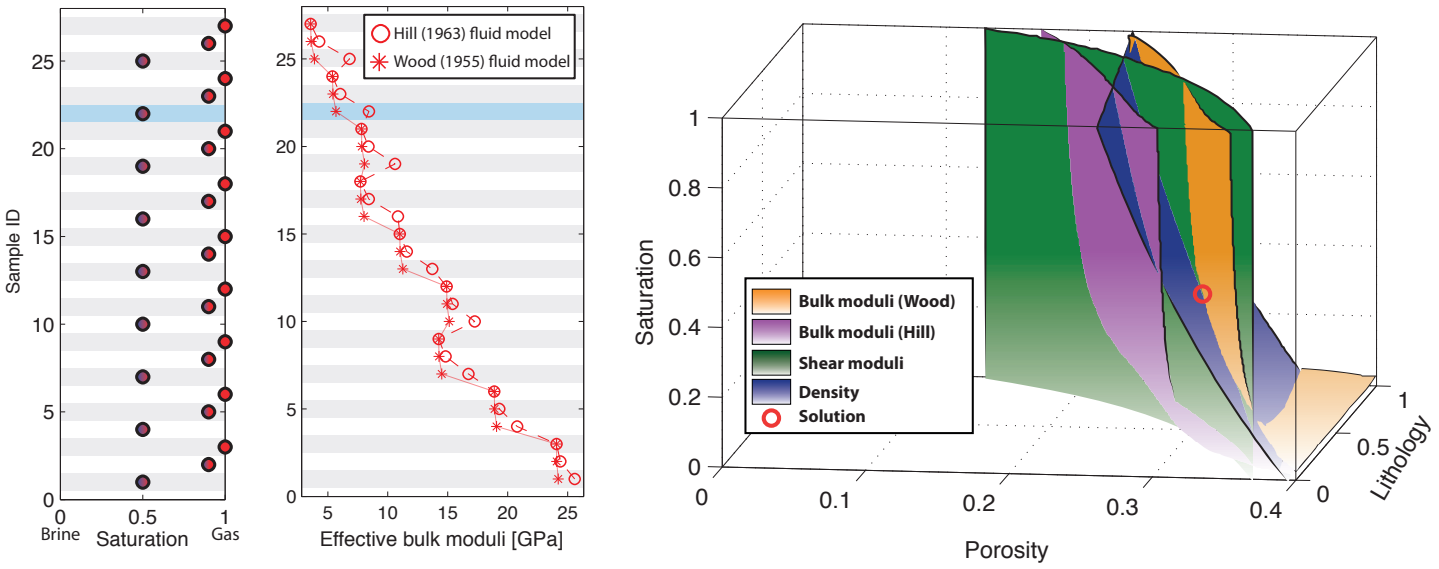

Figure 4.13: Pre defined saturation values are shown next to the corresponding effective bulk moduli when applying two different fluid models. Also, the isosurfaces for sample #22 for both fluid models are shown to the right. Notice that the shear moduli and density constraints are unaffected by different fluid models.

4.4 Summary

In this chapter we have seen the inverse solutions obtained by IRPM from synthetic input data that is fully consistent with the rock physics constraints. Even when applying the same number of input data as dynamic model parameters, the inverse solutions were non-unique. Possible methods for discarding invalid solutions were studied to yield consistent solutions with the synthetic model. Furthermore, three different static model parameters were perturbed to mimic uncertainties that lead to distorted inverse solutions. We have seen how its possible to investigate the influence of uncertainties in specific static model parameters by generating a set of constraint cubes. This may provide reducing misinterpretation risks.

Chapter 5

Use of IRPM in reservoir monitoring

5.1 Outline

Inverse rock physics modeling (IRPM) is flexible in the way it can delineate the various model parameters that a chosen rock physics model holds. In this chapter, the constraint cubes are modified so that they are suited for reservoir monitoring with respect to typical model parameters that alters under production. Following, real data from Glitne, North Sea, will be considered for reservoir monitoring, where a hybrid synthetic approach has been used to compensate the lack of repeated well log observations.

5.2 Modification of constraint cubes in aid of reservoir monitoring

One of the most recent developments in the field of seismic data acquisition is four-dimensional seismic (4D), which adds time as the fourth parameter in reservoir monitoring. This technology involves repeating conventional 3D data acquisition over the same area with a time lapse of anything between a few months to several years to capture changes in subsurface properties. Years of production can cause changes in the reservoir associated with the movement of fluids by introducing temporal saturation and pressure variations. 4D seismic technology makes it possible to surveillance the movement of these fluids and consequently to optimize the location of future wells and speed up production rates (Compagnie Generale de Geophysique, 2006; Bjørlykke, 2010).

Rock physics is essential in 4D reservoir characterization as it serve a tool for interpreting the observations (Bjørlykke, 2010). Rock physics constraints can be used to discriminate how specific model parameters are affecting the elastic properties (see for instance the generated constraint cubes in section 3.3 and 3.4). For instance, saturation effects is often described by applying Gassmann's equation (2.38). In figure 5.1 the effective bulk moduli for a homogenous and patchy fluid filled rock is shown using the Gassmann model. Notice when considering homogenous fluid distribution, the modest amounts of gas introduce almost equal elastic properties as for commercial gas amounts, whereas a patchy fluid shows a more linear decrease in stiffness with increasing gas saturation. Rock physics analysis, like applying the Gassmann model to delineate saturation effects, can be applied to investigate how the seismic properties will change due to a period of hydrocarbon production.

Whereas seismic sensitivity of fluid effects are well-documented and utilized in 4D seismic studies, similar studies on pressure effects are rarely carried out. As the Gassmann model is applicable when any chosen rock physics model predicts the dry rock properties, it labels itself as a universal key for predicting saturation effects. In contrast, an equivalent elastic relationship with pressure effects is yet undiscovered (Landrø et al., 2001; Avseth and Skjei, 2011). In practice, the seismic parameters are commonly linked to pore pressure by performing ultrasonic measurements on several core samples taken from various locations of a hydrocarbon field. Core samples suited for such measurements are

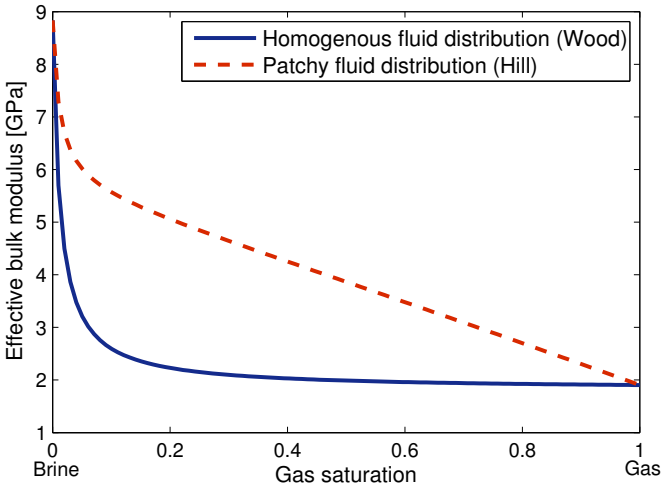

Figure 5.1: The effective bulk moduli of a rock when gas substitution is introduced, modeled by Gassmann's equation (2.38), in case of a homogenous and patchy fluid distribution.

however not always available (Avseth et al., 2005), and even if they are, they may suffer from a wide range of uncertainties and are rarely calibrated with seismic data to provide the seismic sensitivity of pressure effects (Landrø, 2001; Eiken and Tøndel, 2005). Moreover, the majority of rock physics models are pressure insensitive and therefore lacks a input pressure parameter needed to perturb the pressure for the rock physics constrains. However, a hybrid model where a high porosity grain package is computed by the pressure dependent contact theory (CT) models offers an opportunity to consider pressure effects. Also, the pressure dependency for fluids can be introduced by applying the relations proposed by Batzle and Wang (1992). In figure 5.2 rock physics constraints of reservoir A (see section 3.2 and 3.3) are functions of porosity and pore pressure, where lithology is set for pure quartz. The corresponding pore pressure effect at porosity $\phi = 0.4$ can be studied in figure 5.3, where confining pressure P_c is 17.7 MPa from equation (3.3). Both plots implies that increasing pore pressure weakens the grain framework and softens the rock.

The IRPM approach is flexible in the way that the dynamic model parameters can be switched depending on the purpose of the study. In the following, modification of constraint cubes for reservoir monitoring is demonstrated on the reservoir A model by considering lithology to be constant (pure quartz is used in this example) and varying the pore pressure P_p, porosity ϕ and saturation S_g. Hence, the dynamic model parameters are now $\vec{m} = (\phi, P_p, S_g)$. The effective pressure in equation (3.2) represents the input parameter in the CT model, where confining pressure P_c is 17.7 MPa from equation (3.3), and pore pressure has 26 equidistant values between 2 MPa and 17 MPa. Furthermore, by implementing the fluid relations of Batzle and Wang (1992) into the calculations of constraint cubes, the bulk moduli and density of fluids also change as function of pore pressure. The corresponding constraint cubes for P-velocity, S-velocity and density are shown in figure 5.4. These are common data parameters extracted from well logging (Avseth et al., 2005; Barclay et al., 2008).

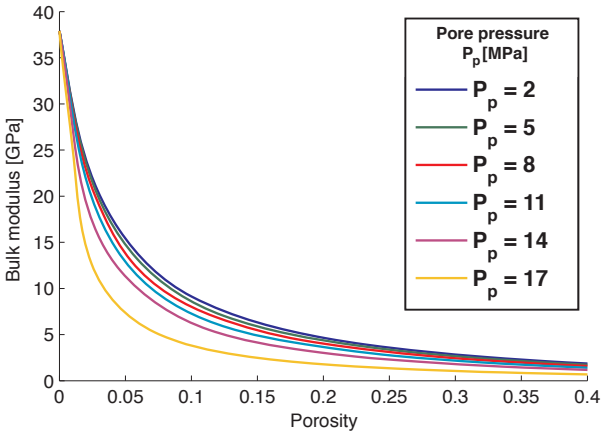

Figure 5.2: Rock physics constraints for reservoir A as function of pore pressure and porosity.

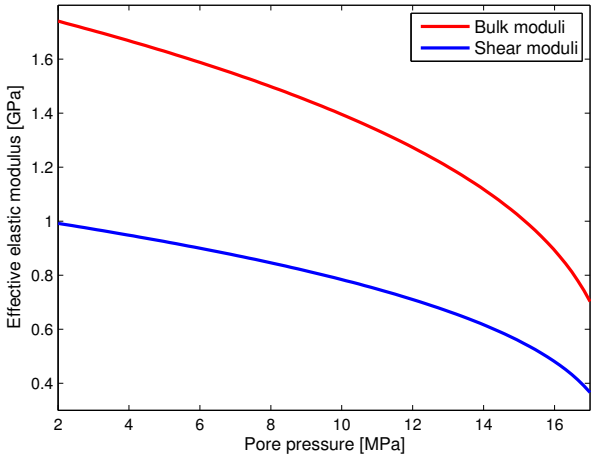

Figure 5.3: Pore pressure effects at $\phi = 0.4$ for reservoir A.

Pore pressure fluctuation in reservoirs may depend on several factors. From the reservoir pore pressure equilibrium state, it is assumed to increase near injection wells and decrease in vicinity of production wells (Cole et al., 2002). The velocity cubes in figure 5.4 implies diminishing values for increasing pore pressure, which expected from studying figure 5.2 and 5.3. Notice however that the velocity sensitivity is relative moderate for varying pore pressure. The elasticity changes remarkably when replacing perturbation of lithology with pore pressure. This is due to the contrast in stiffness between various minerals typically varies in an order up to tens-of-gigapascal, whereas common pore pressure alterations caused by hydrocarbon production is at a scale of fractions-of-gigapascal. Hence, the stiffness of the reservoir A rock is more sensitive to varying lithology than pore pressure variations.

The density of solid constituents are pressure dependent and typically requires pressure changes in order hundred-of-gigapascal, as occur several thousands of kilometers through the earth (Semprich et al., 2010; Pluijm and Marshak, 2004). Hence, the influence on density of solid constituents, due to common pressure alterations of a few megapascals in producing reservoirs, is neglected in the calculation of the density cube in figure 5.4. However, the density cube shows a small increase with increasing pore pressure due to the fluid relations of Batzle and Wang (1992). The density function can be expressed as

$$\rho(\phi, P_p, S_g) = \phi[S_g\rho(P_p)_{\text{gas}} + (1 - S_g)\rho(P_p)_{\text{brine}}] + (1 - \phi)\rho_{\text{quartz}}, \tag{5.1}$$

where ϕ, P_p S_g and ρ_{quartz} are the porosity, pore pressure, gas saturation and quartz density, respectively, and $\rho(P_p)_{\text{gas}}$ and $\rho(P_p)_{\text{brine}}$ are the densities of gas and brine as functions of pore pressure (Batzle and Wang, 1992).

When the 4D suited constraint cubes are generated, step one of the general IRPM workflow in figure 3.1 is fulfilled. To further study how certain model parameters are changing in a reservoir as

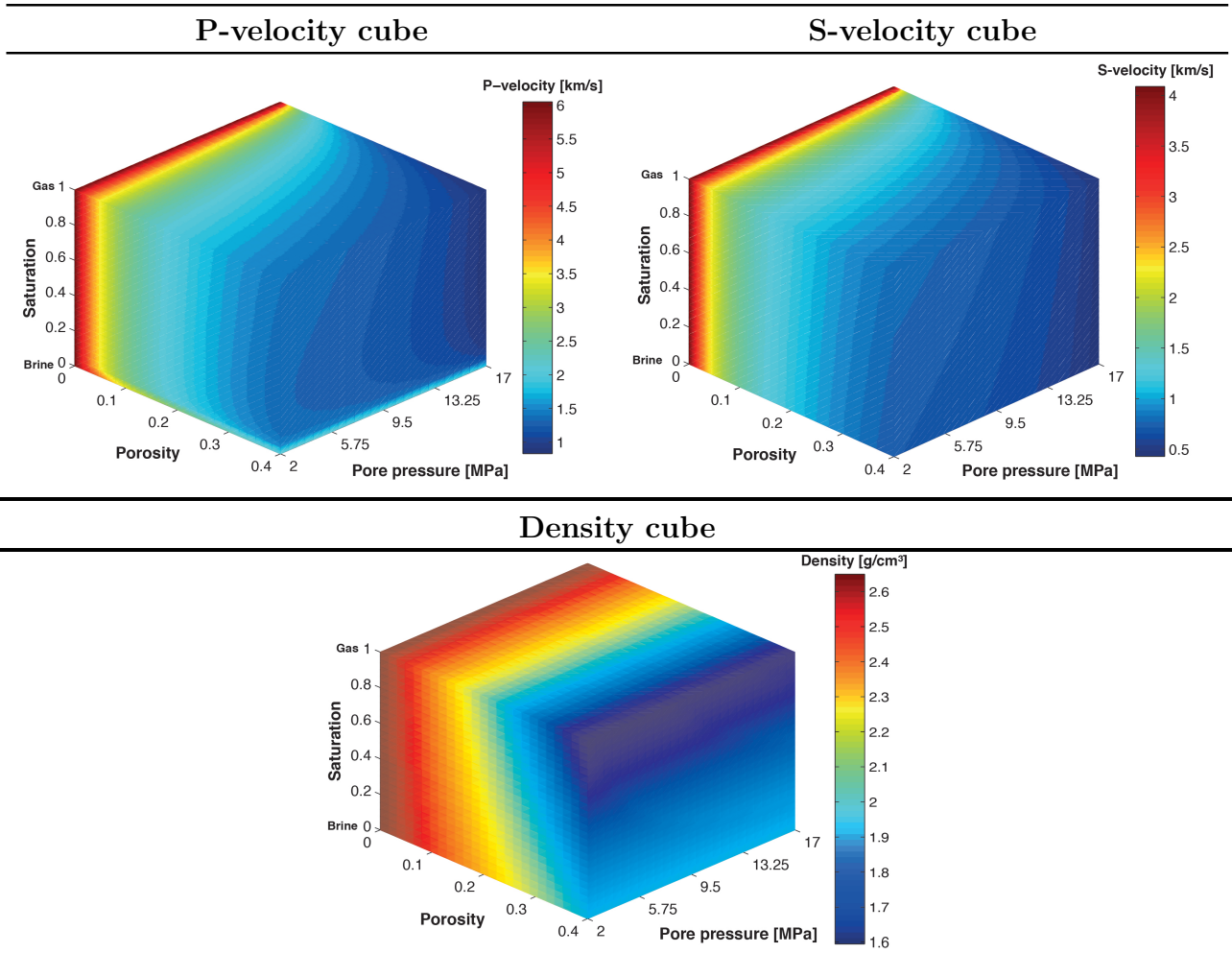

Figure 5.4: The constraint cubes of P and S-velocity and density for reservoir A suited for reservoir monitoring. The previously lithology axis is replaced by pore pressure.

function of time, repeated input data is required. Figure 5.5 shows solutions obtained from applying synthetic input data and the constraint cubes in figure 5.4, where a Newton-Raphson based solver (see appendix B.1) is used. The correct solutions is represented by black squares superimposing the colorized inverse solutions with respect to saturation. The pre defined porosity and saturation samples are shown in figure 4.1, while the pore pressure combinations are defined at 10.1 MPa (corresponds the pore pressure found from equation (3.3) and can be thought of as the equilibrium pore pressure), and a corresponding 5 MPa pore pressure decrease and increase. The solutions are similar to those previously seen in figure 4.6 by that both consistent and incosistent solutions are identified, even when applying three input data.

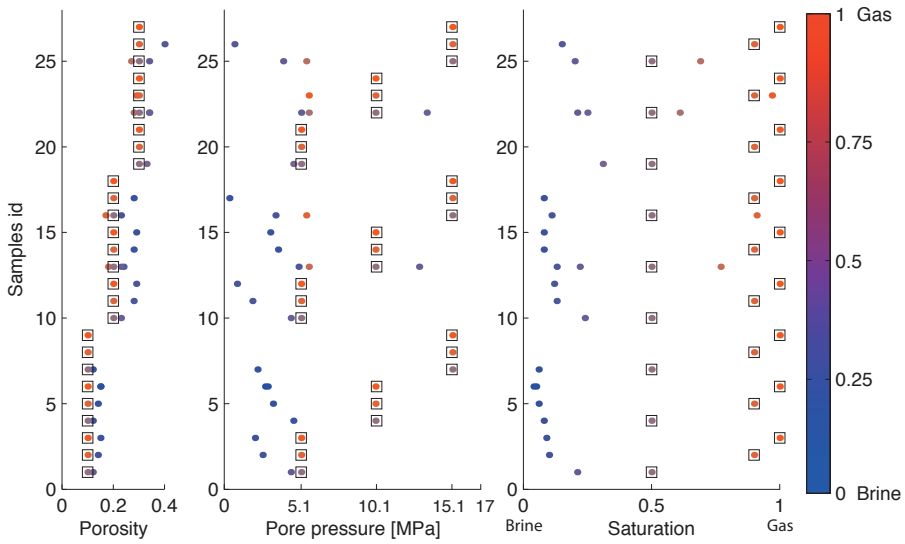

Figure 5.5: The inverse solutions obtained from applying synthetic input data from the modified constraint cubes of reservoir A in figure 5.4.

5.3 A 4D hybrid synthetic approach performed on real data

In this section a 4D study is introduced on synthetic modified well log data from the Glitne field, Norh Sea, by applying the IRPM approach. Glitne is an oil field that was discovered in 1995 with subsequent start of production in 2001, and are developed with six production wells and one water injection well (Norwegian Petroleum Directorate, 2012). The log data shown in figures 5.6 and 5.7, covers a section that comprise two facies referred to as IIb (2155-2165 meters) and IIc (2166-2183 meters) (Avseth et al., 2005). Facies IIb is clean, massive sandstone with clay coatings, but with some presence of clay occupying the pore space. Facies IIc is plane-laminated sandstone with a grain size generally smaller than in IIb and with a higher content of pore-filling clay.

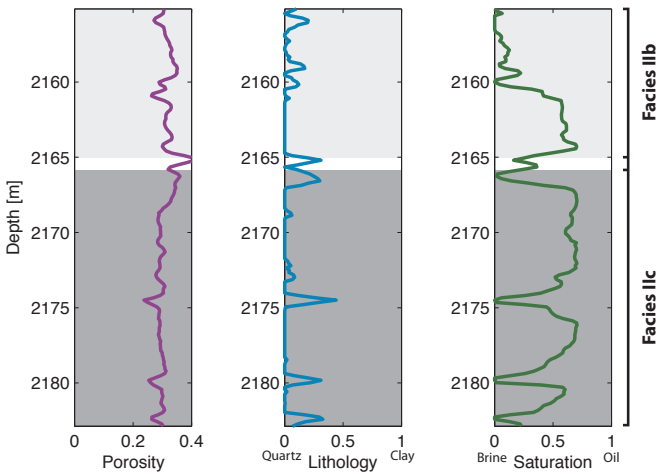

Figure 5.6: Observed model parameters in Glitne.

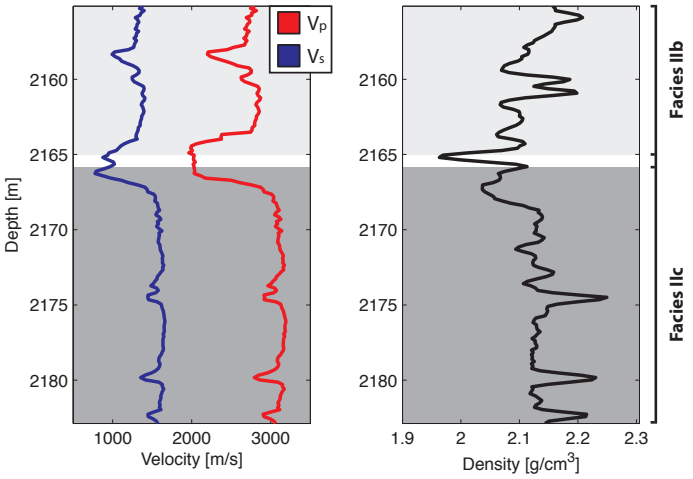

Figure 5.7: Observed data parameters in Glitne.

Previous rock physics modeling on Glitne data by Avseth et al. (2005) and Johansen et al. (2011) focused on finding a representative rock physics model by calibrating the observed model parameters in

aid of reservoir characterization. Avseth et al. (2005) superimposed constraints of various rock physics models onto well log velocity-porosity data from the reservoir zones of Glitne. As such, the well log data tend to cluster around the so called friable sand model, i.e. a lower Hashin-Shtrikman-Walpole bound between zero porosity and high porosity end members, where Hertz-Mindlin theory (Mindlin, 1949) is used for the high porosity point (see figure 2.6).

Johansen et al. (2011) continued by applying the IRPM approach to calibrate the inverse solutions with the model parameter well logs, and used the results obtained by Avseth et al. (2005) in creating rock physics constraint cubes. However, several other rock physics models were additionally tested to check wether an improved calibration was reachable. The result was different from the friable sand model proposed by Avseth et al. (2005), and the modeling suggestions of both Avseth et al. (2005) and Johansen et al. (2011) are summarized in table 5.1 for more details. Also, the constituent properties defined for the most consistent results were unequal in the two studies. In table 5.2 the constituent properties used by Johansen et al. (2011) are shown.

Rock physics modeling suggestions	
Avseth et al. (2005)	Johansen et al. (2011)
Dry rock: Hashin-Shtrikman lower bound interpolates between zero porosity (i.e. the effective mineral properties) and the high porosity end member which were modeled using Hertz-Mindlin theory (Mindlin, 1949). The Hertz-Mindlin model used a critical porosity $\phi_0 = 0.4$, coordination number $C_0 = 8.3$ and effective pressure $P_e = 20$ MPa. The effective mineral properties were modeled using a Hashin-Shtrikman lower bound. **Fluid substitution:** The fluid properties were modeled by Wood's equation 2.39 and fluid substitution introduced applying Gassmann (1951) model.	**Dry rock:** A DEM model interpolates between the porosity end members with a pore model as defined below. The inclusions has the elastic properties of the high-porous end member, which is predicted using a Walton model (Walton, 1987) with a mixed slip factor model (Duffaut et al., 2010; Bachrach and Avseth, 2008). The Walton model used the same ϕ_0, C_0 and P_e values as Avseth et al. (2005) used in the Hertz-Mindlin model, and, the effective mineral properties were also modeled equally. **Fluid substitution:** The fluid substitution is modeled equally as in Avseth et al. (2005). **Pore model:** Aspect ratio spectrum: $[1, 0.5, 0.1, 0.01, 0.001, 0.0001]$; Concentration: $[0.6419, 0.3205, 0.0321, 0.0050, 0.0005, 0.0001]$. **Slip factor model:** 0.4 for facies IIb and 0.6 for facies IIc.

Table 5.1: The results of Avseth et al. (2005) and Johansen et al. (2011) rock physics modeling studies for Glitne.

In this study, constraint cubes with accordance to Johansen et al. (2011) is created so that the the rock physics modeling is calibrated to the Glitne well log data. As mentioned, the geological scenario is slightly different in facies IIb and IIc, and Johansen et al. (2011) proposed using different slip-factors

Constituent	Bulk moduli [GPa]	Shear moduli [GPa]	Density [g/cm^3]
Quartz	36.8	44	2.65
Clay	13	4	2.56
Brine	2.8	–	1.0
Oil	1.005	–	0.78

Table 5.2: Constituent properties that gives the most consistent result during modeling Glitne data according Johansen et al. (2011).

in the Walton (1987) model for this issue (specified in table 5.1). Various slip-factor models means a volume weighted averaging of the elastic moduli predicted at rough and zero grain friction. After generating the constraint cubes and applying input data from the Glitne well log data, the results shown in figure 5.8 for the two facies are obtained. The inverse modeling use P-velocity V_p, S-velocity V_s and density ρ in the IRPM algorithm. The reason for the large number of identified solutions, even when applying three data parameters, is because a proximity detection solver is applied. This solver detects solutions in parts of the isosurfaces that lies within a certain spatial proximity of each other and therefore identifies more solutions than the Newton-Raphson solver (see appendix B for more details about the two different solvers). The solutions are similar to the solutions obtained from synthetic input data in section 4.2 by that there is little variation in the porosity estimations, some variation in lithology and a wide range of possible fluid saturations.

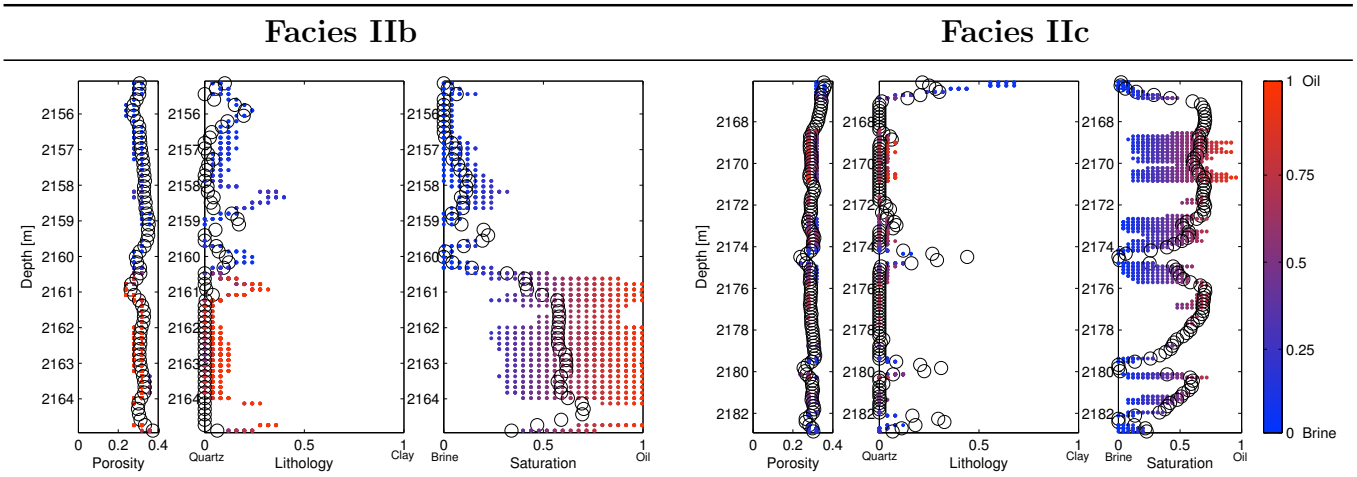

Figure 5.8: The original inverse solutions obtained by using spesifications of Johansen et al. (2011). The black circles represents the observed model parameters (corresponding model parameters in figure 5.6) and the colorized dots denotes the inverse solutions obtained by applying the IRPM approach. The color gradient of the inverse solutions denotes the fluid saturation.

To obtain a 4D reservoir characterization study on the Glitne data, repeated measurements at the same depth sequence should ideally be acquired after a period of hydrocarbon production. Consequently, saturation and pore pressure are expected to change from the initial scenario. In lack of such a data set, and because provided data from Glitne do not include any pressure measurements, a hybrid synthetic data set has been prepared. For this we are only considering data from facies IIb. The hybrid synthetic

data are generated according to the following procedure;

1. The rock physics modeling is done in accordance to Johansen et al. (2011).
2. The rock physics constraints are modified to consider varying pore pressure, as described in section 5.2.
3. Hydrocarbon production is assumed to give an oil saturation reduction and pore pressure increase due to fluid injections. The initial and hybrid synthetic model parameters are shown in figure 5.9.
4. A new set of synthetic input data is calculated in figure 5.10 that correspond to the hybrid synthetic model parameters in figure 5.9.
5. The synthetic input data is applied together with the modified constraint cubes in the IRPM algorithm. In figure 5.11 the hybrid synthetic model parameters superimpose the corresponding inverse solutions.

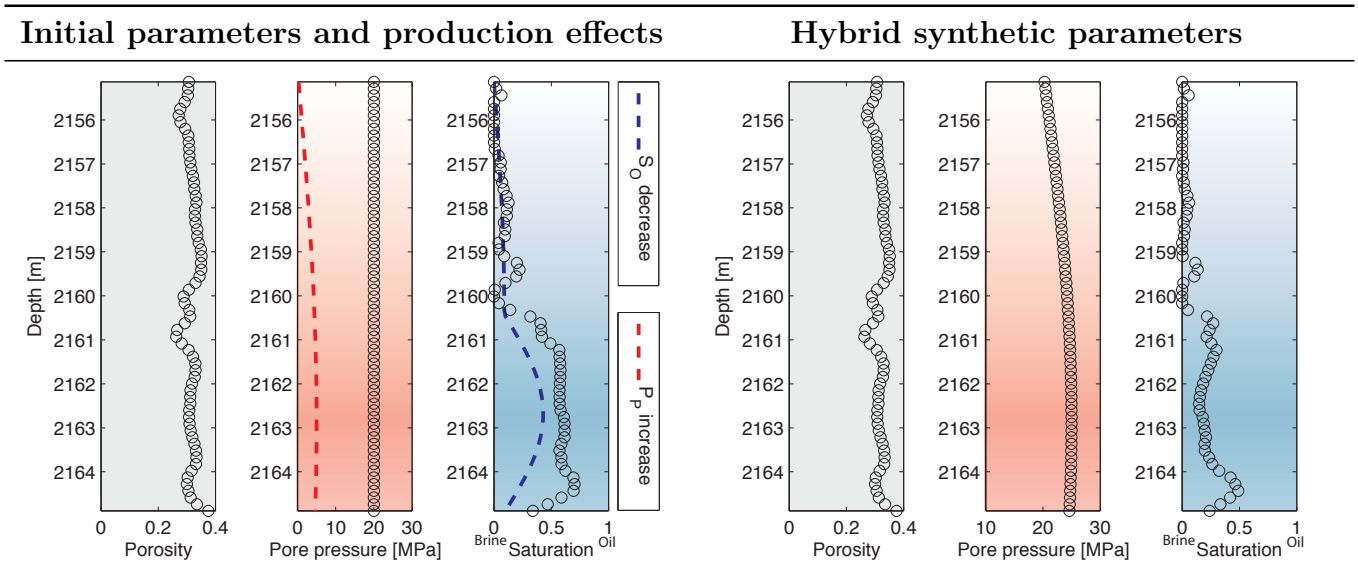

Figure 5.9: Left: the initial model parameters from Glitne (denoted by black circles) together with the considered oil decrease and pore pressure increase due to production. Right: updated model parameters after oil saturation subtraction and pore pressure addition. The porosity is considered to be unaffected by production effects. The background colors denotes the production effects.

As the initial Glitne data implies a varying clay content through facies IIb (see figure 5.8), the lithology in the rock physics constraints were perturbed as $C = [0, 0.05, 0.1]$ and revealed that the lithology have no significant influence on the solutions. Hence, the rock physics constraints used in figure 5.11 and in the following study use a pure quartz lithology.

The simulated oil decrease and pore pressure increase in figure 5.9 have been described by a one half sinus function curve (i.e. $y = sin(x), x \in [0, \pi]$) with a peak at 2162.8 meters that corresponds

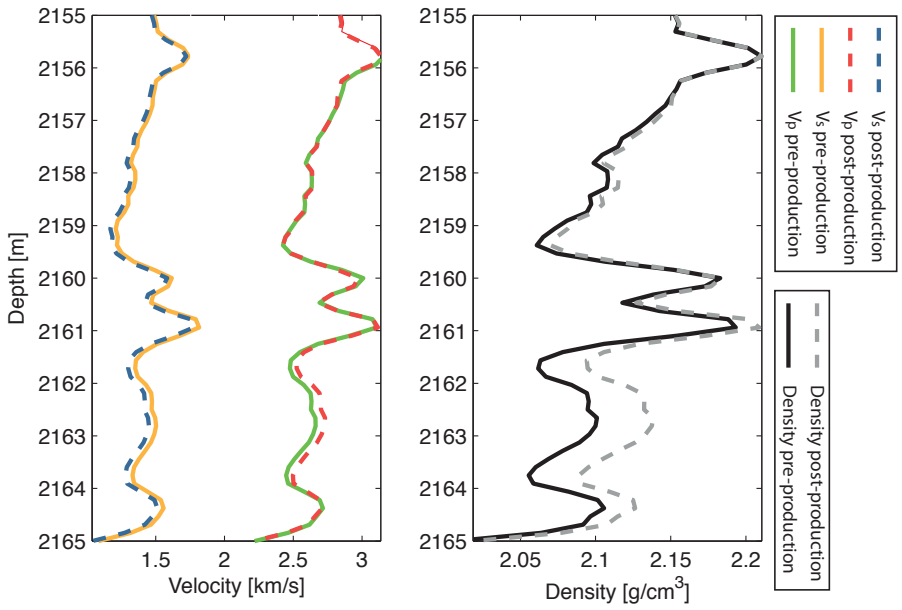

Figure 5.10: The V_P, V_S and ρ parameters before and after the change in saturation and pore pressure shown in figure 5.9.

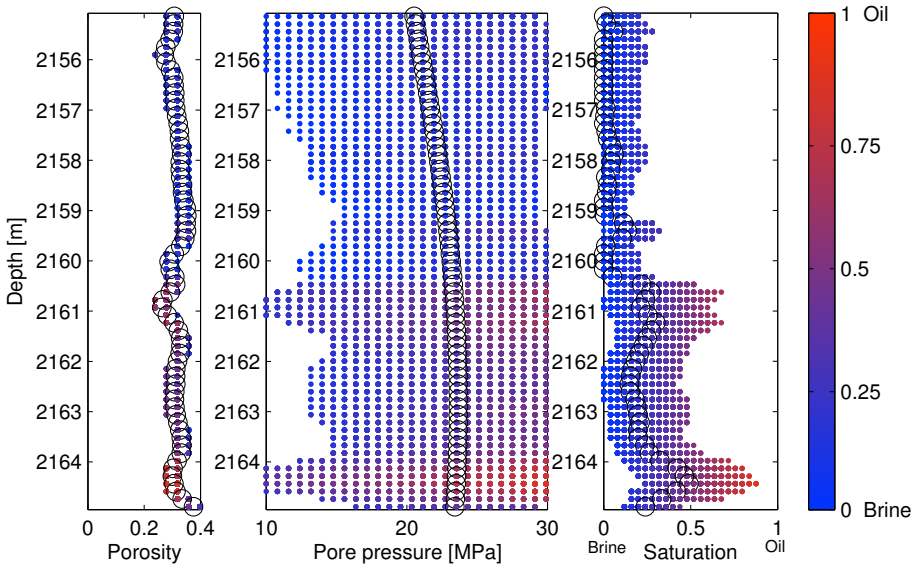

Figure 5.11: The inverse solutions obtained from applying the post-production input data in figure 5.10 and the corresponding constraint cubes (i.e. V_P, V_S and ρ). The black circles denotes the hybrid synthetic model parameters.

a maximum of 33 % oil reduction and a 5 MPa pore pressure increase. The synthetic modeling is assumed to mimic model parameters in vicinity of an injection well, where injected brine at 2162.8 meters cause a higher pore pressure so that oil is squeezed away from the injection well. Notice that the rock physics modeling by Avseth et al. (2005) and Johansen et al. (2011) used an effective pressure of 20 MPa (see table 5.1), which typically lies close to the pore pressure. Hence, the pore pressure is considered to also be 20 MPa in the initial rock physics model for Glitne. In equation (3.2) (assuming $\beta = 1$), confining pressure is set to 40 MPa, whereas the pore pressure varies between 10 MPa and 30

MPa, causing the effective pressure to vary in the rock physics constraints.

Reasonably, the input data in figure 5.10 has changed the most in vicinity of a maximum production effect described in figure 5.9. We see that the bulk density, expressed by equation (5.1), has increased significantly due to changed fluid properties, especially since the average porosity in facies IIb is quite high. Furthermore, the P and S-velocities, expressed respectively by equations (2.15a) and (2.15b), show a rather small change. The fluid independent S-velocity show a small decrease due to increased pore pressure and bulk density. P-velocity however, has slightly increased caused from a raise in the fluid incompressibility due to increasing brine saturations.

Now, an evaluation of the specific model parameter solutions in figure 5.11 follows. Firstly, considering the inverted porosity solutions, they now lies more accurate within the black circles compared to the initial solutions in figure 5.8. This is because the synthetic input data in figure 5.10 is calculated using the same rock physics model as in the rock physics constraints applied in the IRPM approach. On the other hand, the input data used in figure 5.8 are well log observations that disagrees to some extent with the rock physics modeling suggested by Johansen et al. (2011). Any convenient rock physics model must be used with caution when comparing with real data, simply because the models are not capable of incorporating all heterogeneities found in natural born rocks. Real data may also suffer from uncertainties which makes it challenging to compare real and modeled data (Walls et al., 2004).

Continuing the evaluation, the predicted saturations overlap and follows the trend of hybrid synthetic data (i.e. black circles). The saturation is now more brine dominated at all depths. The predicted saturations is still very non-unique.

Pore pressure solutions have not previously been studied by applying the IRPM approach, and is therefore an interesting part of this study. The solutions show a highly non-unique problem that spans more or less the whole perturbed pore pressure window. Reasons causing such poorly constrained solutions were discussed in section 5.2; the elastic properties and density are not very dependent on perturbations in pore pressure. Thus, the pore pressure is cumbersome to sufficiently constrain due to its insensitivity in the rock physics modeling.

At this point, it is important to consider all possible combinations of input data to check if any constraint cubes have isosurfaces that are closer to perpendicular to the pore pressure axis. A sensitivity analysis was conducted to possibly find a better combination of data parameters leading to more narrow and stable solution ranges (Jensen and Johansen, 2011). The sensitivity analysis did not yield one set of input data which one could expect to perform much better than the rest. In addition, the analysis revealed what is already implied by figure 5.11, namely that it might be impossible to constrain the pore pressure. In figure 5.12 a combination of Poisson's ratio v, S-velocity V_S and Lamé constant times density $\lambda\rho$ are used in the IRPM approach, after a manual quality control of the vari-

ous candidates. The sensitivity analysis evaluate data parameters that constrain each specific model parameter conveniently. Hence, the saturation solutions in figure 5.11 has improved significantly due to applying the Poisson's ratio, which is particularly sensitive to saturation. However, the parameter combination did not improve constraining pore pressure.

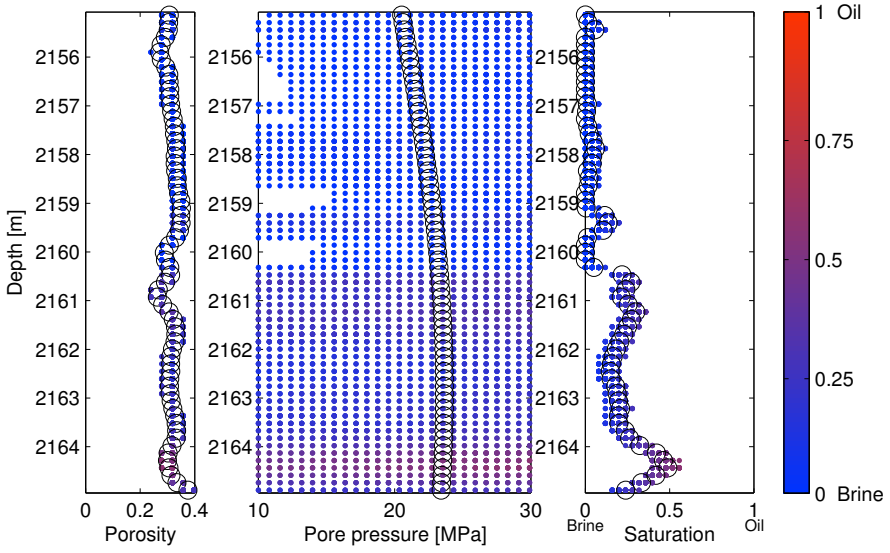

Figure 5.12: The solutions obtained from applying v, V_S and $\lambda\rho$ input data, which corresponds the same V_P, V_S and ρ values shown in figure 5.10.

5.4 Summary

In this chapter we have seen that rock physics constraints can be modified to incorporate model parameters of interest in reservoir monitoring. A calibrated rock physics model for Glitne (Johansen et al., 2011) were following modified to include varying pore pressure. Real input data from Glitne were synthetically modified and applied together with the modified Glitne rock physics constraints to study porosity, pore pressure and saturation solutions. The results obtained showed little variation in porosity solutions, a wide range of possible saturation solutions and pore pressure solutions that were cumbersome to constrain due to its insensitivity in the Glitne rock physics model.

Chapter 6

Discussion and conclusions

6.1 Discussion

This study has mainly contributed to focus on two areas: (1) impact of static model parameter uncertainties on IRPM solutions and (2) customization of the IRPM approach for reservoir monitoring applications. Along this research, pitfalls and limitations attached to the usage of IRPM in reservoir characterization were encountered and are in the following discussed.

The model dependency of the IRPM approach is illustrated by comparing the elasticity constraint cubes of reservoir A and B (see figures 3.4, 3.5 and 3.6). The contact theory and contact cement theory, used respectively for reservoir A and B, deviates significantly. Reservoir A exhibits relative monotonous low elastic values throughout the whole PLF domain, except for low porosities and quartz dominated solid phase (see also figure 2.6). This emphasizes the importance of deposited cement at the grain surface with respect to elastic properties in the high porosity regime. Also, for reservoir A and B we use lower and upper Hashin-Shtrikman-Walpole bounds, respectively, to interpolate between zero and high porosity end members. The lower and upper bounds simulate various sorting and cementation trends, respectively, two very different physical processes.

Figure 4.7 shows density and shear moduli constraints by their respective isosurfaces representing sample #5 of the porosity, lithology and saturation solutions in figure 4.5. The angle formed between the normal vectors at every point on a specific isosurface and a particular model parameter axis implies how well the data parameter constrains the considered model parameter. As the average normal vector of an isosurface approaches parallel with a model parameter axis, the solution range narrows for that particular model parameter. The average normal vectors of the individual isosurfaces in figure 4.7 creates an angle with the porosity axis that is significantly closer to zero than the equivalent angle at the lithology axis. This is why the solution range (marked as orange intervals on each model parameter axis) of porosity is narrower than for lithology in figure 4.5. The orientation of isosurfaces is consistent in terms of physical property reasoning; the porosity reflects the contrast in stiffness and density between the solid and fluid components which is certainly much larger than the contrast between various solid or various fluid components, respectively represented by lithology and saturation.

Figure 3.7 and 3.9 show considered bulk moduli isosurfaces for reservoir A and B, respectively. These have in common a quite flat topology except when approaching fully brine saturations. This is due to the fluid substitution from applying the Gassmann model (see figure 5.1). The bulk moduli is monotonically strongly decreasing within approximately 0-10 % gas increase, whereas the remaining gas substitution has a small effect. When applying several additional data parameters with a different saturation sensitivity, it is a high probability for isosurfaces to intercept in the regions of a fully brine saturated rock. Examples are found in figures 4.6 and 5.5; the majority of samples where three input data have been applied has a second solution denoted by a high brine content. Thus, applying bulk moduli, or other related parameters, in the IRPM approach, may imply non-unique solutions.

This issue is however most relevant considering mixed fluids with a significant contrast in physical properties. Figure 6.1 shows interceptions between the isosurfaces in figure 3.11. Notice how the red and green interception line (both including bulk moduli constraints) tend to bow when approaching low gas content and subsequently intercepts one another. Hence, conditioning and limitations of solution constraints depends on the orientation and flatness of isosurfaces, which can be conducted by a sensitivity analysis that yields an optimal combination of input data (Jensen and Johansen, 2011).

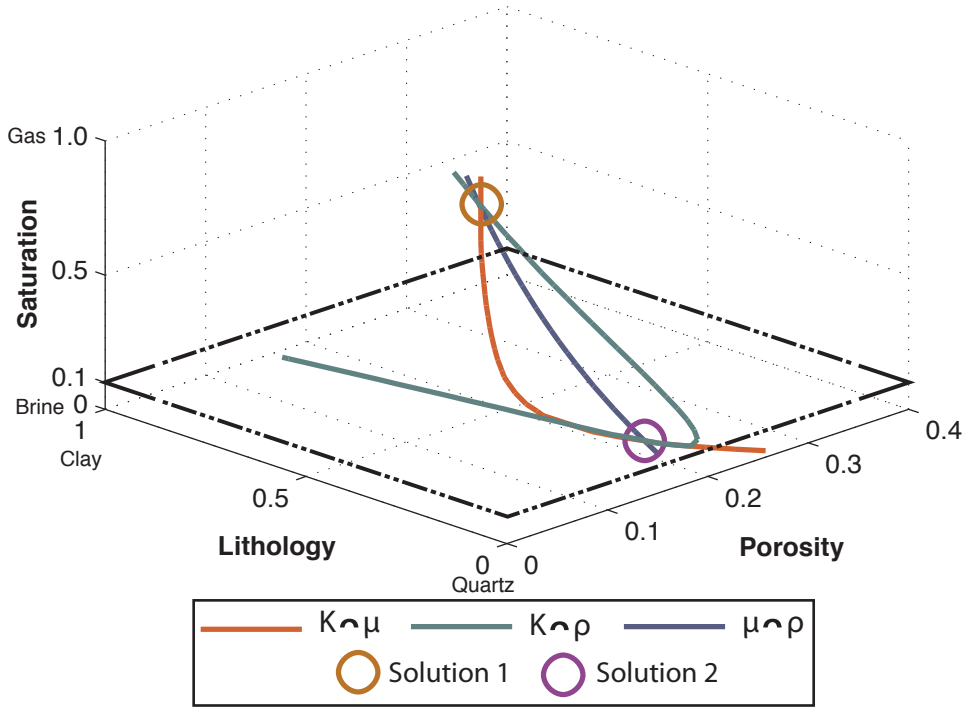

Figure 6.1: Interception lines and points corresponding the isosurfaces in figure 3.11. The bold black frame denotes a 10 % gas saturation, where the bulk moduli changes significantly when approaching brine.

The pore pressure in figure 5.11 and 5.12 show poorly constrained solutions, whereas figure 5.5 shows consistent pore pressure solutions when considering synthetic input data from the 4D suited rock physics constraints of reservoir A (see section 5.2). However, the hybrid synthetic modeling of Glitne also considered consistent input data, so why are the pore pressure solutions in figure 5.11 and 5.12 so weakly constrained? The answer lies within the differently used rock physics models; reservoir A use a lower Hashin-Shtrikman-Walpole (HSW) bound to interpolate the zero and high porosity end members, while for Glitne, we use a differential effective medium (DEM) model that predicts a far stiffer rock (see figure 6.2). The DEM model considers the mineral point as host material and the high porosity framework as inclusions by cracks, ellipsoids and spheres. The HSW lower bound represents the rock as infinite many two-phase spheres composed of an inner core of the mineral point and an outer core of the grain package end member. Hence, the two models reacts very differently to pore pressure perturbation. The stiffness predicted by DEM is hardly affected by common pore pressure changes so that isosurfaces align parallel with pore pressure axis (see figure 6.3). Hence, the low pore pressure sensitivity in the hybrid synthetic modeling for Glitne yields topological features of isosurfaces that constrains pore pressure insufficiently and implies fragile pore pressure solution stability.

If a rock physics model imposing a stronger pore pressure dependency is applied, the pore pressure constraints would be stronger. However, contact theory implies that elastic properties change so tiny due to common pore pressure variations, that isosurfaces most likely are close to parallel with the pore pressure axis also if a more proper model is used. Also, geochemical processes that initiates due to pore pressure changes and may potentially affect the rock physics, have not been considered in this study. Furthermore, if cementation initiates in an unconsolidated sandstone reservoir so that it becomes partly cemented, a patchy cementation model (see section 2.4.8) designates as a reasonable candidate. This model indicates declining pore pressure sensitivity for increasing cementation. This is one reason for why the 4D seismic technique has been more successful for unconsolidated reservoirs than carbonates and cemented sandstones (Lumley, 2001).

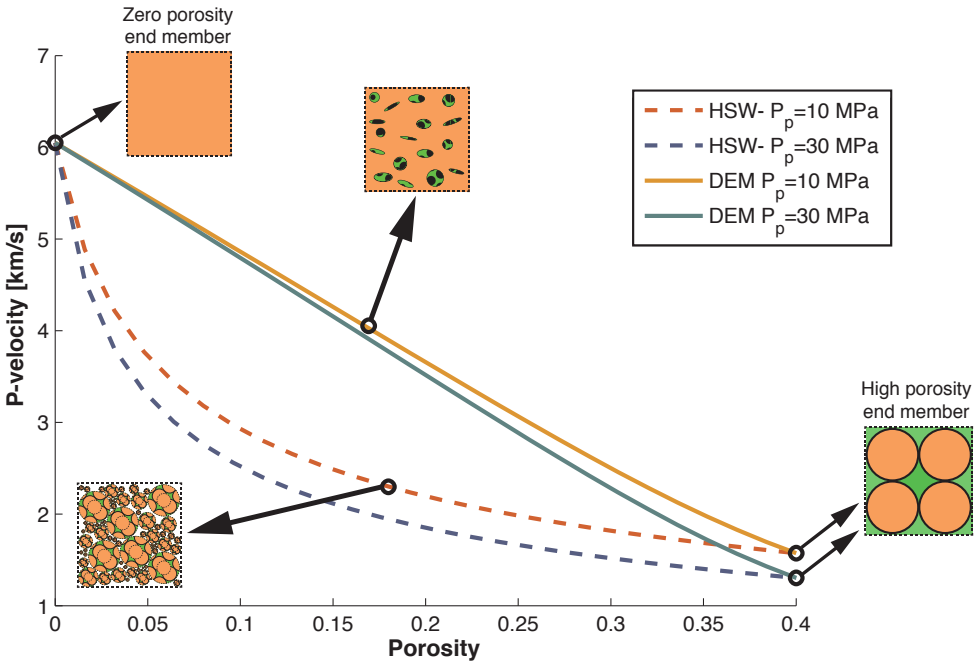

Figure 6.2: A DEM and lower HSW model that interpolates between zero and high porosity end members at two different pore pressure P_p states. The pore fluid is gas.

The saturation solutions in figure 5.12, applying a input data combination of Poisson's ratio, S-velocity and Lamé constant times density, provide better saturation constraints than those seen in figure 5.11, where P-velocity, S-velocity and density were applied. Poisson's ratio v is directly related to the V_P/V_S ratio by

$$v = \frac{0.5\left(V_P/V_S\right)^2 - 1}{\left(V_P/V_S\right)^2 - 1}, \tag{6.1}$$

which is very sensitive to saturation changes and often interpreted as a direct hydrocarbon indicator by AVO (Amplitude Versus Offset) analysis (Gelius and Johansen, 2010). Hence, both Poisson's ratio and the V_P/V_S ratio are convenient input data to achieve narrow saturation solutions.

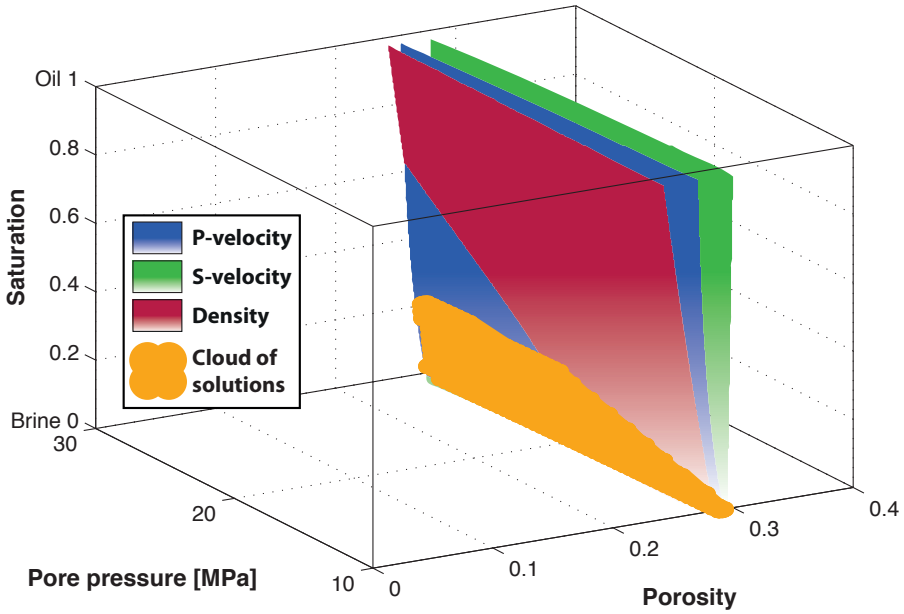

Figure 6.3: An arbitrary sample of intersecting isosurfaces in the hybrid synthetic modeling of Glitne. Notice how the cloud of solutions obtained by the proximity solver (see appendix B.2) are aligned parallel with the whole pore pressure axis. In contrast, the solutions constrains the porosity to a narrow range.

In the reservoir A and B models described in chapter 3, a brine-gas fluid mixture was assumed. In the hybrid synthetic modeling of Glitne in chapter 5 however, a brine-oil fluid mixture was assumed. The elastic behavior of oil and gas are significantly different (Batzle and Wang, 1992) as demonstrated in figures 6.4 and 6.5. The property contrast between oil and brine are significantly smaller than for gas and brine. Hence, discrimination of brine and oil can be challenging due to their relative similar elastic properties (Lumley, 2001; Avseth et al., 2005). Therefore, it can be more difficult to obtain sufficient constrained solutions when oil substitution is considered.

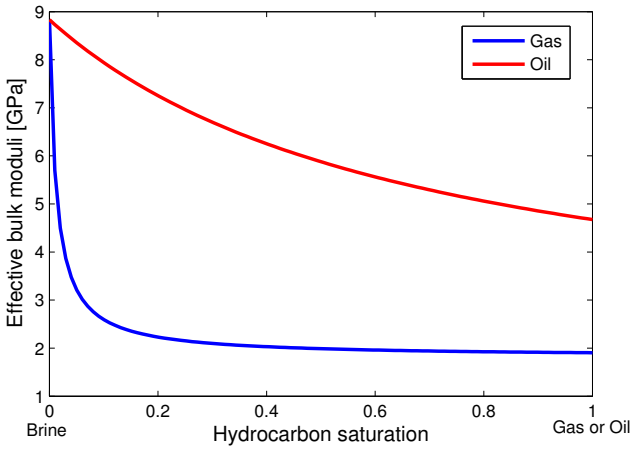

Figure 6.4: The difference in effective bulk moduli between a gas and oil substitution modeled by the Gassmann model. The fluid bulk moduli of gas and oil used here is 0.03 GPa and 1 GPa, respectively.

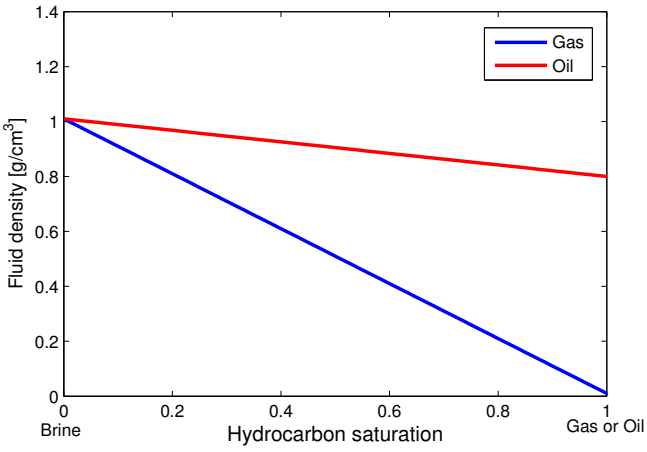

Figure 6.5: The difference in fluid density between gas and oil substitution. The density of brine, gas and oil used here is 1.01 g/cm^3, 0.01 g/cm^3 and 0.8 g/cm^3, respectively.

For some rock physics models, certain data parameters are represented as non-monotonous functions of model parameters, such as the V_P/V_S ratio (see figure 6.6). This makes it more cumbersome to achieve well constrained inverse solutions as the topology has a bigger surface area receivable for several interception points. A solution to this issue is to consider appropriate bulk and shear moduli values with a simpler topology that corresponds a specific V_P/V_S ratio. The points of intersection between the respective bulk and shear moduli isosurface may subsequently represent the specific V_P/V_S ratio constraint (Johansen et al., 2011).

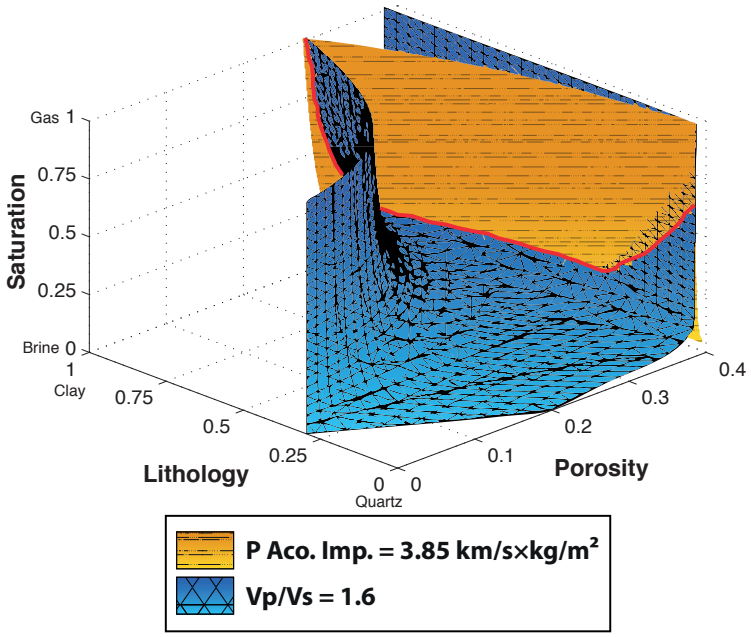

Figure 6.6: The acoustic impedance and V_p/V_s ratio isosurfaces, that are typical data parameters obtained from seismic inversion. Contour lines are attached to the isosurfaces to reveal their topology. The red line denotes the interception between the two isosurfaces.

During modeling, it is important to address simplifications made that may lead to uncertain reservoir parameters. E.g. lithological assumptions considered in this research a binary mixture of quartz and clay is used. Real geology is characterized by heterogeneity due to e.g. salt intrusions, volcanic tuff, silica ooze, etc. (Avseth et al., 2005). In general, if information about a specific reservoir property is unavailable, a set of rock physics constraints should be constructed where each reservoir property is altered to capture possible heterogeneity models, as described in section 4.3.

In an early stage of seismic exploration, restricted geophysical observables due to absence of well information can limit applications of IRPM. P-wave interval velocities is usually the first available information acquired, whereas seismic inversion contributes acoustic impedance and V_P/V_S ratios (Avseth et al., 2005). However, the P-wave interval velocities are an average over a continuous rock volume, whereas velocities obtained from acoustic impedance estimations describes the physical properties at a point of discontinuity, which its location is unspecified due to lack of well information. Averaging velocities over a bigger volume introduce uncertainties due to internal heterogeneities. Hence, cau-

tion must be aimed at combining velocities retrieved from acoustic impedance of unknown origin with a P-wave interval velocity that may in fact vary significantly within the rock volume. A proximity detection solver (see appendix B.2) may be appropriate when combining such uncertain input data.

6.2 Conclusions

In this study we have seen that applications of inverse rock physics modeling (IRPM) in reservoir characterization reveal this as an undetermined problem with non-unique solutions. However, IRPM emphasizes the non-uniqueness of the problem. Also, this study has highlighted interpretation pitfalls due to uncertainties in reservoir parameters.

The IRPM approach is flexible in the way it predicts any of the reservoir parameters that the applied rock physics model holds. Hence, IRPM can be applied in reservoir monitoring to interpret temporal variations in fluid saturation and pressure. A reservoir monitoring study on real data from Glitne, North Sea, has been considered to predict porosity, saturation and pore pressure solutions. The results obtained showed little variation in the porosity solutions, a wide range of possible saturation solutions and pore pressure solutions that were cumbersome to constrain.

The main findings are:

- The IRPM approach may serve a tool for predicting reservoir properties (e.g. porosity, lithology, saturation) when elastic properties (e.g. elastic moduli, seismic velocities, density) are known. IRPM makes it practical to emphasize the non-uniqueness of the problem.
- As to the simplifications made in modeling inherent complex rocks, a set of perturbed rock physics constraints can be made in order to study the influence of uncertainties in reservoir parameters by analyzing the corresponding solutions obtained by IRPM.
- IRPM is flexible as varies rock physics constraints that can be considered as basis for reservoir monitoring, i.e. if the rock physics model includes the relevant reservoir parameters that alters during production.
- A reservoir monitoring study approach was performed on hybrid synthetic data from Glitne, in lack of real repeated observations. It was found that pore pressure solutions were cumbersome to constrain due to its insensitivity in the rock physics model relevant for Glitne. As such, well constrained solutions are limited to reservoir properties that are sufficiently sensitive for specific rock physics models.

References

Agersborg, R., T. A. Johansen, M. Jakobsen, J. Sothcott, and A. Best (2008). Effects of fluids and dual-pore systems on pressure-dependent velocities and attenuations in carbonates. *Geophysics 73*, N35–N47.

Auld, B. A. (1990). *Acoustic fields and waves in solids* (Second ed.), Volume 1. Krieger Publishing Company.

Avseth, P., N. Skjei, and G. Mavko (2012). Rock Physics Modelling of Stress Sensitivity in Patchy Cemented Sandstones. *74th EAGE Conference and Exhibition, 4-7 June, 2012, Copenhagen, Denmark.* Expanded Abstracts, I009.

Avseth, P., T. Mukerji, and G. Mavko (2005). *Quantitative Seismic Interpretation. Applying Rock Physics Tools to Reduce Interpretation Risk*. Cambridge University Press.

Avseth, P. and N. Skjei (2011). Rock physics modeling of static and dynamic reservoir properties - A heuristic approach for cemented sandstone reservoirs. *The Leading Edge 30*, 90–96.

Bachrach, R. and P. Avseth (2008). Rock physics modeling of unconsolidated sands: Accouting for nonuniform contacts and heterogenous stress fields in the effective media approximation with applications to hydrocarbon exploration. *Geophysics 73*, E197–209.

Barclay, F., A. Bruun, K. B. Rasmussen, J. C. Alfaro, A. Cooke, D. Cooke, D. Salter, R. Godfrey, D. Lowden, S. McHugo, H. Özdemir, S. Pickering, F. G. Pineda, J. Herwanger, S. Volterrani, A. Murineddu, A. Rasmussen, and R. Roberts (2008). Seismic inversion: Readying between the lines. *Schlumberger oilfield review*, 42–63.

Batzle, M. and Z. Wang (1992). Seismic properties of pore fluids. *Geophysics 57*, 1396–1408.

Berryman, J. (1992). Single-scattering approximations for coefficients in Biot's equations of poroelasticity. *The Journal of the Acoustical Society of America 91*, 551–571.

Bjørlykke, K. (2010). *Petroleum Geoscience: From Sedimentary Environments to Rock Physics*. Springer-Verlag Berlin Heidelberg, ISBN 9783642023323.

Boggs, S. (2006). *Principles of Sedimentology and Stratigraphy* (Fourth ed.). Pearson Prentice Hall.

Bruggemann, D. A. G. (1935). Berechnung verschiedener physikalischer Konstanten von heterogenen Substanzen. I. Dielektrizitätskonstanten und Leitfähigkeiten der Mischkörper aus isotropen Substanzen. *Annalen der Physik 416*, 636–664.

Cole, S., D. Lumley, M. Meadows, and A. Tura (2002). Pressure and saturation inversion of 4D seismic data by rock physics forward modeling. *SEG Int'l Exposition and 72nd Annual Meeting, 6-11 October, 2002, Salt Lake City, Utah.* Expanded Abstracts, 2475–2478.

Compagnie Generale de Geophysique (2006). *1931-2006: 75 Years of Passion.* Chene.

Digby, P. J. (1981). The Effective Elastic Moduli of Porous Granular Rocks. *Journal of Applied Mechanics 48*, 803–808.

Dræge, A., T. A. Johansen, I. Brevik, and C. Dræge (2006). A strategy for modelling the diagenetic evolution of seismic properties in sandstones. *Petroleum Geoscience 12*, 309–323.

Duffaut, K., M. Landro, and R. Sollie (2010). Using Mindlin theory to model friction-dependent shear modulus in granular media. *Geophysics 75*, E143–152.

Dvorkin, J., H. Mavko, and A. Nur (1991). The effect of cementation on the elastic properties of granular material. *Mechanics of Materials 12*, 207–217.

Eiken, O. and R. Tøndel (2005). Sensitivity to time-lapse seismic data to pore pressure changes: Is quantification possible? *The Leading Edge 24*, 1250–1254.

Gassmann, F. (1951). Über die elastizität poröser medien. *Vierteljahrsschrift der Naturforschenden Gesellschaft in Zürich 96*, 1–23.

Gelius, L. J. and T. A. Johansen (2010). *Petroleum Geophysics.* UniGEO as. *Accessible from* ***http://www.unigeo.no***.

Guéguen, Y. and V. Palciauskas (1994). *Introduction to the Physics of Rocks.* Princeton University Press.

Han, D. H., A. Nur, and D. Morgan (1986). Effects of porosity and clay content on wave velocities in sandstones. *Geophysics 51*, 2093–2107.

Hashin, Z. and S. Shtrikman (1963). A variational approach to the theory of the elastic behaviour of multiphase materials. *Journal of the Mechanics and Physics of Solids 11*, 127–140.

Hill, R. (1963). Elastic properties of reinforced solids: Some theoretical principles. *Journal of the Mechanics and Physics of Solids 11*, 357–372.

Hornby, B. E., L. M. Schwartz, and J. A. Hudson (1994). Anisotropic effective-medium modeling of the elastic properties of shales. *Geophysics 59*, 1570–1582.

Jakobsen, M., J. A. Hudson, T. A. Minshull, and S. C. Singh (2000). Elastic properties of hydrate-bearing sediments using effective medium theory. *Journal of Geophysics Research 105*, 561–577.

Jensen, E. H. (2011). *Methods for improved prediction of elastic, eletrical and reservoir properties.* Ph. D. thesis, Univeristy of Bergen.

Jensen, E. H. and T. A. Johansen (2011). Conditioning of elastic and electrical parameters for use in reservoir characterization. *In preparation to be submitted to Geophysical Prospecting*.

Johansen, T. A., E. H. Jensen, G. Mavko, and J. Dvorkin (2011). Inverse rock physics modeling. *In preparation to be submitted to Geophysics*.

Johansen, T. A., K. Spikes, and J. Dvorkin (2004). Strategy for estimation of lithology and reservoir properties from seismic velocities and density. *SEG Int'l Exposition and 74th Annual Meeting, 10-15 October, 2004, Denver, Colorado*.

Kelley, C. (2003). *Solving nonlinear equations with Newton's method.* Society for Industrial and Applied Mathematics, ISBN 9780898715460.

Kullerud, K. (2010). E-module: Clastic sedimentary rocks. *Retrieved 14.09.2011 from* ***http://ansatte.uit.no/kku000/webgeology/***.

Landau, L. D. and E. M. Lifshitz (1967). *Theory of Elasticity.* Moscow: Editions Mir.

Landrø, M. (2001). Discrimation between pressure and fluid saturation changes from time-lapse seismic data. *Geophysics 66*, 836 –844.

Landrø, M., P. Digranes, and L. K. Strønen (2001). Mapping reservoir pressure and saturation changes using seismic methods - possibilities and limitations. *First Break 19*, 671-677.

Lumley, D. E. (2001). Time-lapse seismic reservoir monitoring. *Geophysics 66*, 50–53.

Mavko, G., T. Mukerji, and J. Dvorkin (2009). *The Rock Physics Handbook: Tools for Seismic Analysis of Porous Media* (Second ed.). Cambridge University Press.

Mindlin, G. W. (1949). Compliance of elastic bodies in contact. *Journal of Applied Mechanics 16*, 259–268.

Norwegian Petroleum Directorate. General information about Glitne, North Sea. *Retrieved 16.04.2012 from* ***http://www.npd.no/Templates/OD/Article.aspx?id=4197***.

Nur, A., G. Mavko, J. Dvorkin, and D. Galmudi (1995). Critical porosity: The Key to Relating Physical Properties to Porosity In Rocks. *SEG Annual Meeting, 8-13 October, 1995, Houston, Texas.* Expanded Abstracts, 878.

Ødegaard, E. and P. Avseth (2003). Interpretation of Elastic Inversion Results of Using Rock Physics Templates. *Extended Abstract E-17, 65th EAGE Conference and Exhibition, 2-5 June, 2003, Stavanger*.

Pluijm, A. V. D. B. and S. Marshak (2004). *Earth Structure* (Second ed.). W. W. Norton & Company, ISBN 0-393-92467-X.

Pujol, J. (2003). *Elastic Wave Propagation and Generation in Seismology*. Cambridge University Press, ISBN 0521520460.

Reuss, A. (1929). Berechnung der Fließgrenzen von Mischkristallen auf Grund der Plastizitätsbedingung für Einkristalle. *ZAMM - Journal of Applied Mathematics and Mechanics / Zeitschrift für Angewandte Mathematik und Mechanik 9*, 49–58.

Semprich, J., N. S. C. Simon, and Y. Y. Podladchikov (2010). Density variations in the thickened crust as a function of pressure, temperature, and composition. *International Journal of Earth Sciences 99*, 1487–1510.

Tarantola, A. (2005). *Inverse problem theory and methods for model parameters estimation*. Society for Industrial and Applied Mathematics, Philadelphia, ISBN 0-89871-572-5.

Walls, J., J. Dvorkin, and M. R. Carr (2004). Rock Solid Images: Well Logs and Rock Physics in Seismic Reservoir Characterization. *Offshore technology conference, 3-6 May, 2004, Houston, Texas. Retrieved 03.04.2012 from* `http://www.rocksolidimages.com/pdf/Walls-Dvorkin-Carr_04.pdf`.

Walpole, L. J. (1966a). On bounds for the overall elastic moduli of inhomogenous systems–I. *Journal of the Mechanics and Physics of Solids 14*, 151–162.

Walpole, L. J. (1966b). On bounds for the overall elastic moduli of inhomogenous systems–II. *Journal of the Mechanics and Physics of Solids 14*, 289–301.

Walton, K. (1987). The effective elastic moduli of a random packing of spheres. *Journal of the Mechanics and Physics of Solids 35*, 213–226.

Wood, A. W. (1955). *A textbook of sound: being an account of the physics of vibrations with special reference to recent theoretical and technical developments*. G. Bell.

Appendix A

Contact cement theory (CCT) coefficients

The parameters $\hat{S}_n$ and $\hat{S}_\tau$ in the CCT model (Dvorkin et al., 1991) are proportional to the normal and shear stiffnesses, respectively, of a cemented two-grain combination. They depend on the contact cement amount, the physical properties of the cement and grains as defined in the following relations:

$$
\begin{aligned}
&\hat{S}_n = A_n b^2 + B_n b + C_n,\\
&A_n = -0.024153\Lambda_n^{-1.3646},\\
&B_n = 0.20405\Lambda_n^{-0.89008},\\
&C_n = 0.00024649\Lambda_n^{-1.9864},\\
&\hat{S}_\tau = A_\tau b^2 + B_\tau b + C_\tau,\\
&A_\tau = -10^{-2}\left(2.26v^2 + 2.07v + 2.3\right)\Lambda_\tau^{0.079v^2+0.1754v-1.342},\\
&B_\tau = \left(0.0573v^2 + 0.0937v + 0.202\right)\Lambda_\tau^{0.0274v^2+0.0529v-0.8765},\\
&C_\tau = 10^{-4}\left(9.654v^2 + 4.945v + 3.1\right)\Lambda_\tau^{0.01867v^2+0.4011v-1.8186},\\
&\Lambda_n = \frac{2\mu_c}{\pi\mu}\frac{(1-v)(1-v_c)}{(1-2v_c)},\\
&\Lambda_\tau = \frac{\mu_c}{\pi\mu},\\
&b = \frac{a}{R},
\end{aligned}
$$

where μ and v are the shear modulus and the Poisson's ratio of the grains, respectively; μ_c and v_c are the shear modulus and the Poisson's ratio of the cement, respectively; a is the radius of the contact cement layer and R is the grain radius (Mavko et al., 2009). However, b has been explicitly expressed in equations (3.5) and (4.1) for various contact cementation models.

Appendix B

Solvers applied in the inverse rock physics modeling (IRPM)

In essence, the IRPM can be reduced to a geometrical problem of identifying intersections of isosurfaces. In this work, two solvers have been utilized for this purpose, namely a Newton-Raphson based method and a proximity based method (Jensen, 2011). Whereas the Newton-Raphson solver identifies exact points of intersecting isosurfaces, the proximity detection solver incorporate a small uncertainty. Hence, the proximity detection solver is favorable when considering real input data. Figure B.1 shows examples of the two different solvers in action, considering two and three input data.

B.1 Newton-Raphson's method

This solver is based on Newton-Raphosn's method (Kelley, 2003), and it identifies the intersections of the isosurfaces to within a special level of precession. The solvers starts by subdividing the constraint cubes into $25 \times 25 \times 25$ smaller cubes, where those subcubes not constraining all isosurfaces of interest are discarded. For the remaining subcubes, x, y and z coordinates (i.e. model parameter values) of the isosurface intersections are calculated according to Newton-Raphson's method in three dimensions (Kelley, 2003).

B.2 Proximity detection method

This solver does not only identify intersections of isosurfaces as solutions, but also points on the isosurfaces which are within a maximum distance of each other. Hence, a tolerance parameter can be adjusted to handle various levels of uncertainty. The solver refines the constraint cubes of $26 \times 26 \times 26$ points to $50 \times 50 \times 50$ points to gain high resolution so that the non-linear topology is captured. Furthermore, points on isosurfaces that lies within a maximum tolerated distance from each other are identified as possible solutions. At each solution, a sphere with a pre-defined radius comprehends points on isosurfaces that are identified as solutions as well. If the refined constraint cubes has a

sufficiently high resolution, the span of solutions obtained is continuous and the actual solutions can be interpreted to be within the respective solution range.

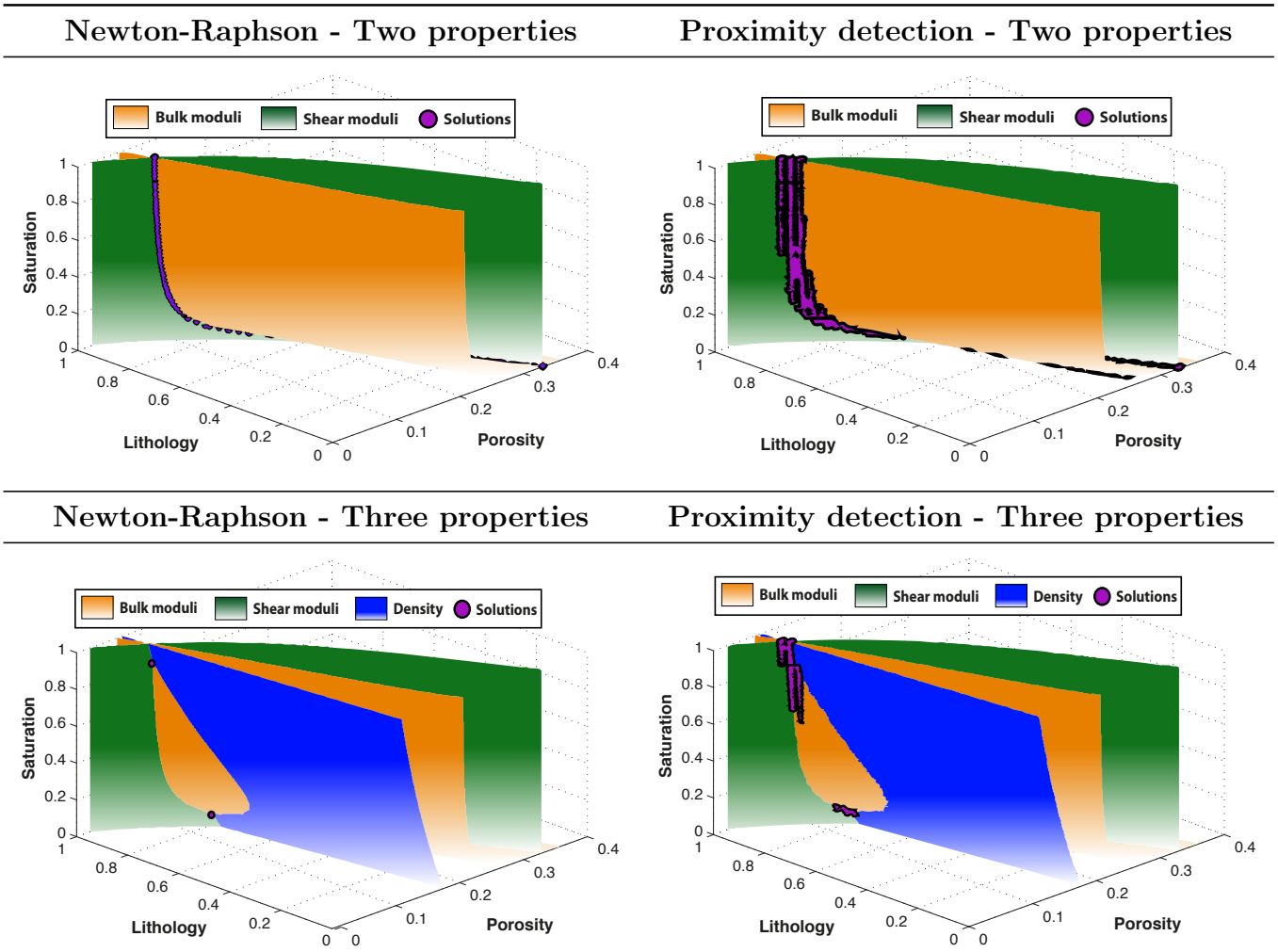

Figure B.1: The Newton-Raphson's and proximity detection solvers in action, for two and three input data. Notice how the proximity based method identifies a cloud of solutions around the points where the Newton-Raphson's based method identifies exact solutions.